Microstructural degradation of bearing steels

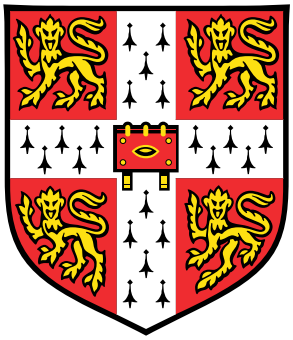

Wilberth Solano Alvarez

Department of Materials Science and Metallurgy

University of Cambridge

This dissertation is submitted for the degree of

Doctor of Philosophy

Downing College

December 2014

To my family, friends, heavy deadlifts, and tea.

Declaration

I hereby declare that except where specific reference is made to the work of others, the contents of this dissertation are original to the best of my knowledge and have not been submitted in whole or in part for consideration for any other degree or qualification in this, or any other university. This dissertation is my own work and contains nothing which is the outcome of work done by others unless referenced or specified in the text or acknowledgements. This dissertation contains no more than 60,000 words.

Parts of the work presented in this thesis have been published in the following articles:

1. W. Solano-Alvarez and H. K. D. H. Bhadeshia. White-Etching Matter in Bearing Steel. Part I: Controlled Cracking of 52100 Steel. *Metallurgical and Materials Transactions A*, 45:11 (2014), 4907-4915. (Chapter 3)

2. W. Solano-Alvarez and H. K. D. H. Bhadeshia. White-Etching Matter in Bearing Steel. Part II: Distinguishing Cause and Effect in Bearing Steel Failure. *Metallurgical and Materials Transactions A*, 45:11 (2014), 4916-4931. (Chapter 4)

3. W. Solano-Alvarez, EJ Song, D-K Han, D-W Suh and H. K. D. H. Bhadeshia. Cracks in martensite plates as hydrogen traps in a bearing steel. *Metallurgical and Materials Transactions A*, 46:2 (2015), 665-673. (Chapter 5)

4. W. Solano-Alvarez, E. J. Pickering and H. K. D. H. Bhadeshia. Degradation of nanostructured bainitic steel under rolling contact fatigue. *Materials Science & Engineering A*, 617 (2014), 156-164. (Chapter 6)

5. H. K. D. H. Bhadeshia and W. Solano-Alvarez. Critical assessment 13: Elimination of white etching matter in bearing steels. *Materials Science and Technology*, 31:9 (2015), 1-6. (Conclusions)

6. W. Solano-Alvarez, H. F. G. Abreu, M. R. da Silva and M. J. Peet. Phase quantification in nanobainite via magnetic measurements and X-ray diffraction. *Journal of Magnetism and Magnetic Materials*, 378 (2015), 200-205. (Appendix B)

Wilberth Solano Alvarez
December 2014

Acknowledgements

I would like to extend my most sincere gratitude to my supervisor, Prof. Harry Bhadeshia for guiding this project so enthusiastically, for his vast knowledge and humbleness, for always providing constructive feedback and innovative ideas, and giving me the opportunity to enrich my doctoral education through conferences, local and foreign research collaborations, and freedom in pursuing interesting or alternative research topics. Working hand in hand with one of the persons I most admire was a truly unforgettable and life-changing experience.

I was very fortunate to be able to secure funding from several sources that allowed me to offset all fees, research expenses, and maintenance costs, while still being able to conduct research freely. This allowed me to pursue not only fundamental or simply interesting research, but also address controversies outlined in recent reviews. For this, I am very grateful to the National Council of Science and Technology (CONACyT for its abbreviation in Spanish) for awarding me the Bicentennial Fellowship for master's studies and the CONACyT-Cambridge Scholarship for PhD studies, co-funded by the Cambridge Overseas Trust. I am also very thankful to the Technit group integrated by Ternium and Tenaris who supported most of my studies through the Roberto Rocca Undergraduate Scholarship and later on with the Roberto Rocca Postgraduate Fellowship, which was renewed for an extra year. I am very grateful to The Ironmongers' Company for their kind support to fund additional activities such as conferences abroad and a research exchange in the Republic of Korea. I am also very grateful to Downing College for their economic support through the Buchanan Fund for difficult times, the Downing Student Support Endowment for conference expenses, and the Alumni Sports Fund. Finally, I would like to thank the Eric Evans Fund and the Hawks' Charitable Trust for their support towards my sporting activities.

Most of the work presented in this document would not have been possible without the help, suggestions or advice from other members of the Phase Transformations and Complex Properties group, such as Dr. Steve Ooi, Dr. Ed Pickering, Chris Hulme-Smith, Dr. Mathew Peet, Dr. Yan Pei, James Nygaard, Dr. Lin Sun, Dr. Lucy Fielding, Dr. Hector Pous,

and visiting scientist Dr. Ting Ping Hou. I am especially grateful to my coauthors, Ed, for his help in using the TEM and for answering my many questions about supervisions, and Mathew for his analytical insight and computational savvy. I am also thankful to members of the SKF University Technology Centre, most notably Dr. JeeHyun Kang, Peter Walker, Chris Amey, Dr. Pedro Rivera, and other students of his such as Dr. Bij-Na Kim and Dr. Enrique Galindo. I am very grateful to all members of the Computational Metallurgy Laboratory of the Graduate Institute of Ferrous Technology (GIFT) of the Pohang University of Science and Technology (POSTECH), specially Dr. Eunju Song, Dr. Seung-Woo Seo, Dr. You Young Song, Do-Kyeong Han, Geunsu Jung, Jeong In Kim, Soon-Young Jun, and Prof. Dong Woo Suh for their hospitality, friendliness, and help in and out of the lab; they made my time in Korea truly enjoyable.

I would like to extend my most sincere appreciation to all the staff of the Department of Materials Science and Metallurgy, including Andrew Rayment at the mechanical testing lab, David Saul, Terry Mosdall, and Frank Clarke of the undergraduate teaching lab for specimen preparation advice and for letting me use their great microscopes, Andrew Moss and Mary Vickers of the X-Ray diffraction lab for their help with running scans and interpreting data, David Nicol for his help with microscopy, Paul Stokes and other members of the workshop, Dr. Rosie Ward of the admissions office, and Dr. Carsten Schwandt for lending the vacuum oven and isostatic press. I would also like to thank SKF, especially Steve Lane, for allowing usage of the rolling contact fatigue testing machine and helping with final sample preparation. I would like to show my gratitude to Jonathan Duff and Prof. Mike Smith at the University of Manchester for the high strain rate tensile testing performed at their laboratory. I am very grateful to Hamilton Ferreira Gomes de Abreu from UFC and Manoel Ribeiro da Silva from UNIFEI Itajubá for their help in performing the magnetic measurements of nanobainite. Finally, I would like to thank Beverley Calvey and Tina D'Angelico of the accommodation office at Downing College for the excellent college accommodation provided during the past three years and all the staff at the catering department for fuelling me with the best food in Cambridge.

Just as important as academic supervision, funds, and technical help, the moral support given by my family and friends and the healthy distraction that sport brings have allowed me stay motivated, enjoy my studies, have fun, and keep my sanity through the difficult times. My uttermost appreciation goes to my mother, father, and sister for their endless support and love, to Lara Graham for her sweetness and thoughtfulness, and to all my friends who are my family away from home: Jorge Quintana, Varun Choda, Rob Liu, Andrew Hodgson,

Erick Hernandez, Yunuen Montelongo, Calvin Wakeford, Alp Notghi, Louis Cox-Brusseau, Claire Armstrong, Georgina Hutton, Damien Bruneau, amongst many others. I extend special thanks to Paulina Montoya for her patience, motivation, and for being one of the few non-Phase Transformations group person to truly understand my project. Last but not least, I want to thank all other members of the powerlifting club and powerlifting in general for being the perfect way to 'unload' from a stressful day at work.

Abstract

The aim of the work presented in this thesis is to clarify one of the most fundamental aspects of fatigue damage in bearings steels through critical experiments, in particular whether damage in the form of cracks precedes hard “white-etching matter" formation, which is carbon supersaturated nanoscaled ferrite. Heat treatments have been designed to create four different crack types and distributions: scarce martensite plate cracks, fine grain boundary cracks, abundant martensite plate cracks, and surface cracks. Subsequent rolling contact fatigue experiments showed that the amount of hard white-etching matter is higher in pre-cracked samples compared to those without prior damage and that its formation mechanism is the frictional contact of disconnected surfaces within the bulk that elevate the temperature and localise deformation. These key experiments indicate that hard white-etching matter is the consequence, *not* the cause, of damage. Therefore, one way to avoid white-etching matter is by increasing the toughness of the material. The macroscopically homogenous distribution of microcracks proved also to be a useful rolling contact fatigue life enhancer due to damage deflection via crack branching and a powerful trap for diffusible hydrogen. Successful trapping was corroborated by the inability of hydrogen to cause crack propagation via embrittlement or accelerate white-etching matter generation during rolling contact fatigue. By also studying the behaviour of a nanostructured bainitic steel under rolling contact fatigue, it was found that its degradation mechanism is ductile void formation at bainitic ferrite/stress-induced martensite interfaces, followed by growth and coalescence into larger voids that lead to fracture along the direction of the softer phase as opposed to the conventional damage mechanism in 52100 steel of crack initiation at inclusions and propagation. Given the relevance of phase quantification in nanobainite and the possible surface artefacts introduced by preparation, alternative methods to X-ray diffraction such as magnetic measurements were also investigated. The lack of hard white-etching matter obtained in the carbide-free nanostructured bainite led to conclude that an alternative route to mitigate hard white-etching matter could be by eliminating pre-eutectoid carbides from the microstructure, therefore restricting their dissolution and ultimate carbon supersaturation of the mechanically deformed and homogenised nanoferrite.

Table of contents

Nomenclature

α	Ferrite
α_b	Bainite
α'	Martensite
γ	Austenite
ε	Strain - subscript 't' for observed total strain. Epsilon carbide
η	Fe_2C carbide
θ	Cementite. Bragg angle
ν	Poisson's ratio - subscript '1' for ball, '2' for cylinder or rod
ρ	Dislocation density
σ	Applied stress - subscript 'r' for residual compressive stress
τ	Shear stress - subscript 'max' for maximum and 'xz,max' for orthogonal
Φ	Diameter - subscript '1' for ball, '2' for cylinder or rod, 'a' for ball contact diameter with balls, 'b' for pitch diameter of balls and retainer, and 'c' for cup contact diameter with balls
χ	Fe_5C_2 carbide
Ω	Atomic volume of iron
a	Lattice parameter - subscript 'γ' for austenite, 'α'' for martensite. Width of contact area in the tangential direction
A	Cup angle

b	Semi-minor axis of projected elliptical area of contact. Magnitude of Burgers vector. Length of contact area in the axial direction
c	Concentration - subscript 'γ' in austenite or 'α' in ferrite, superscript '0' for lower limit of concentration. Lattice parameter - subscript 'α'' for martensite
C	Theoretical load carrying capability for 1 million inner race revolutions with a 10% probability of failure
C_{app}	Apparent hydrogen solubility
D_{eff}	Effective hydrogen diffusivity
E	Young's modulus - subscript '0' for initial value, '1' for ball, '2' for cylinder or rod, superscript '$*$' for effective value. Ball revolutions for one revolution of retainer
F	Shaft revolutions for one revolution of retainer
H	Hardness - subscript 'RT' for room temperature. Number of stress cycles between ball and specimen for one revolution of retainer
H_{eff}	Effective field
I_{ss}	Steady state current
k	Correlation factor for the calculation of the intrinsic saturation magnetisation of ferrite based on chemical composition
K	Number of stress cycles between balls and specimen for one revolution of specimen
K_α	X-ray spectral line
L	Length
$\overline{L}$	Mean linear intercept size - subscript 'γ' for prior austenite grain size
L_{10}	Basic rating life
LF	Life factor - subscript 'a', for processing, 'b' for type of steel, 'c' for compressive residual stress, and 'd' for hardness

M_s	Martensite start temperature. Intrinsic saturation magnetisation of ferrite - superscript 'calc' for calculated and 'exp' for experimental
m_s	Specific saturation magnetisation - superscript 'Fe' for iron, 'Co' for cobalt, and 'Ni' for nickel
M_f	Martensite finish temperature
n	Load life exponent depending on the type of bearing
N_{Fe}^c	Number of iron atoms at the surface of cracks present in unit volume of steel
N_t^c	Density of hydrogen trapping sites due to cracks
N_t^{gb}	Density of hydrogen trapping sites due to grain boundaries
N_t^{ρ}	Density of hydrogen trapping sites due to dislocations
N_V^c	Crack number-density
p	Pressure - subscript '0' for contact pressure at centre of contact area
P	Permeation. Operating load. Pearlite
Q	Quenched. Initial point of contact between uppermost ball and rings, subscript 'max' for highest loaded position
$Q-T$	Quenched and tempered
$Q-T-RCF$	Quenched, tempered and rolling contact fatigue tested
r_0	Radius of contact area
R	Radius - subscript '1' for ball, '2' for cylinder or rod, 'eq' for equivalent, superscript '$*$' for effective value. Surface roughness - subscript 'a' for average or 'q' for root mean squared
t	Time - subscript 'γ' for austenitisation, 'b' for breakthrough time, superscript 'isotrans' for isothermal transformation and 'temper' for tempering

T	Temperature - subscript 'T' for operating temperature, 'RT' for room temp, 'γ' for austenitisation, '0' for temperature at which austenite and ferrite of same the composition have the same Gibbs free energy, superscript 'isotrans' for isothermal transformation and 'temper' for tempering
V	Volume fraction, subscript 'γ' for austenite, 'θ' for cementite, 'α' for ferrite, 'α'' for martensite, or 'α_b' for bainite
x	Amount of hydrogen evolved - subscript 'γ' from austenite or 'α' from ferrite. Weight percent

AM	Air melting
BCC	Body-centred cubic
BCT	Body-centred tetragonal
CCT	Continuous cooling transformation
CVD	Carbon vacuum degassing
DER	Dark-etching region
EBSD	Electron backscattered diffraction
EDS	Energy-dispersive X-ray spectroscopy
EFR	Electroflux remelting
ESR	Electroslag remelting
FEG	Field emission gun
FIB	Focused ion beam
GB	Grain boundary
MP	Martensite plate
MPC	Martensite plate cracks
OM	Optical microscopy
RCF	Rolling contact fatigue
SC	Surface cracks
SEM	Scanning electron microscope (microscopy)

SS	Stainless steel
STEM	Scanning transmission electron microscope (microscopy)
TDS	Thermal desorption spectroscopy
TEM	Transmission electron microscope (microscopy)
TRIP	Transformation-induced plasticity
UTW	Ultra-thin window
VAR	Vacuum arc remelting
VIM	Vacuum induction melting
VP	Vacuum processing
VSM	Vibrating sample magnetometer
WEC	White-etching crack
WEM	White-etching matter
WSF	White structure flaking
XRD	X-ray diffraction

Chapter 1

Introduction

Both from the engineering and metallurgical point of view, the rolling bearing represents the most essential of machine elements and the true workhorse of industry. Such bearings are subjected to complex and repeated contact loads which induce damage that accumulates and ultimately leads to failure or removal from service when monitoring systems identify precursors to failure. However, it is not clear whether some of the damage that is detected in post-service examinations is the cause or consequence of failure. In order to gain confidence in the mechanisms of failure, it is necessary to be able to reproduce damage phenomena in controlled experiments, where the ambiguity of interpretation is reduced. There is a particular kind of microstructural damage in the form of regions of the structure which appear white in etched metallographic samples, that is a cause of controversy in the context of failure mechanisms in large bearings used in wind turbines [1]. The hard regions of white-etching matter are sometimes identified as the cause of failure, and the mechanism by which this structure forms has been associated with diverse phenomena such as severe localised deformation, adiabatic shear, carbide dissolution, and low-temperature recrystallisation [1–4].

An alternative interpretation is that the process begins with the initiation of a micro-crack [5], which then develops the white-etching matter by the rubbing together of the crack surfaces, causing intense localised mechanical deformation [4]. The design of better bearing steels depends on the clarification of these issues. For example, the idea that white-etching matter formation is the cause of failure would require different issues to be addressed, whereas if cracking precedes white-etching matter formation, then the problem can be mitigated by enhancing the resistance to cracking [5].

One way of establishing the mechanism is to subject samples, in which microscopic

cracks are introduced deliberately, to rolling contact loading. Such experiments would reveal whether white-etching matter development in the pre-cracked samples occurs at the internal crack faces with greater vigour, than in specimens that do not contain cracks. They could also help establish whether damage development is a function of the orientation of the crack faces relative to the principal stresses during rolling contact loading. However, to conduct such experiments it is necessary to create populations of cracks which permit the steel to survive rolling contact loads for a significant number of cycles, sufficient to stimulate white-etching matter, but less than that required to cause gross fracture over the period of the test. The cracks that are relevant are classified as 'very short', typically 1-10 μm in length [6]. In chapter 3, the methods designed for creating such cracks are presented as a prelude to the critical experiments presented in chapter 4, which investigate white-etching matter generation when the cracked samples are subjected to rolling contact stresses.

The vast majority of bearing steels are manufactured to be extremely hard in order to resist rolling-contact stresses of the order of 2 GPa. The steels typically contain 1 wt% of carbon and 1.5 wt% Cr so that they can be processed into a martensitic microstructure, which is then subjected to a low-temperature tempering heat-treatment that has the dual purpose of reducing the retained austenite content to a level consistent with dimensional stability requirements, and to improve the properties of the martensite [4]. Like most strong steels, bearing steels can be victims of hydrogen, which severely degrades the mechanical properties at concentrations as small as 1 part per million [7, 8]. In chapter 5, it was felt that it would be interesting to examine the role of the microscopic cracks as traps for hydrogen. This work might be applicable to inclusions that have weak interfaces with the steel matrix, that should act in a manner similar to the cracks in accumulating hydrogen and keeping it there in a molecular and innocuous form.

It is possible that nanostructured bainite, which consists of an extremely fine mixture of ferrite and austenite [9, 10], may prove suitable for the manufacture of bearings. Despite its exceptional abrasive, wear, and fatigue resistant properties, the stresses involved in rolling contact fatigue are quite different from uniaxial loading, a close approximation being a combination of mean, uniaxial compressive-stress and torsion that are in phase with respect to their maximum values [11, 12]. The purpose of the work presented in chapter 6 was to investigate the rolling contact fatigue phenomena associated with nanostructured bainite. The damage mechanisms have never before been reported and are unlikely to be identical to common bearing steels mentioned in chapter 4 due to the complete absence of carbides and the work hardening mechanism associated with the retained austenite.

Given that there are now several commercial applications and numerous research programmes associated with nanostructured bainite, it was thought useful to develop an easy method to characterise the retained austenite content with confidence. At present, there are many methods to determine the retained austenite content [13–17], each of which has limitations that have been discussed extensively [18, 19]. Diffraction using X-rays or neutrons has the advantage of rigour in the analysis of data and remains the method of choice for phase fraction analysis. However, magnetic methods to determine volume fractions can be rapid to implement even though they may require calibration. One difficulty is that the calibration constants seem to vary widely as a function of the alloy composition and microstructure [20–25]. In appendix B, X-ray diffraction and magnetic detection of retained austenite in nanostructured bainitic steel is investigated in an attempt to clarify the nature of the calibration function required for the magnetic technique and consolidate it as an alternative to X-ray diffraction.

In conclusion, this project is centred around the idea of conducting critical experiments, which will unveil the sequences, mechanisms, and properties of an extensively debated, but still enigmatic phenomenon. By possessing a clearer perspective of the microstructural degradation of bearing steels during rolling contact fatigue, it should be possible to alter their chemical composition and heat treatment to produce tougher, hard white-etching matter proof alloys. In turn, bearings could have a longer life, a wider range of operating temperatures, and a higher resistance to hostile environments. This longer life is particularly useful for the large bearings used in offshore wind turbines as it would decrease costs due to maintenance or early failure. By reducing the kilowatt-hour cost of wind energy, this renewable energy source could gain ground on polluting energy sources such as coal plants. In the long term, this research project strives for society's energy sustainability through the cost efficiency of one of the most widely used machine elements: bearings.

Chapter 2

Background

2.1 Bearings

Bearings are machine elements that enable the low-friction relative motion of a rotative component around a line or a plane. They are also able to accurately position moving parts relative to fixed ones and transmit load [26]. In order to support continuous, oscillatory, or static operation and radial, axial, or combined loads, rolling bearings incorporate a series of lubricated rolling elements fixed in a cage that is contained between two concentric rings. Since rolling bearings are ubiquitous, not only in everyday objects such as blenders or bicycles, but also in highly complex machines such as jet engines or generators, there is a myriad of different types of bearings depending on their functions and capabilities. A description of the main components and the basic rolling bearings types will be presented from the manufacturing and engineering perspective. Although there exist alternative bearing mechanisms that do not use rolling elements such as plain bearings or even superconducting bearings [27], this document will deal only with the former.

As mentioned before, the main components in a bearing are: cages, rolling elements, and rings. Bearing cages have the objective of avoiding frictional contact between the opposite moving surfaces of two consecutive rolling elements and providing them with guidance through the raceways. By introducing a cage with pockets for the rolling elements, the risk of frictional damage is reduced and the speed of the bearing is increased [26]. Cages are normally made of pressed mild steel sheet for high-speed capabilities or machined from solid brass, bronze, or steel, which can be plated for corrosion resistance. For precision machine-tool bearings, the cages are machined from phenolic resin, which can operate at higher speeds under limited lubrication or moulded in nylon, which can accommodate high degrees of misalignment.

Bearing rolling elements, instead, have the function of transmitting the load from the outer to the inner ring. The maximum load carrying capacity is determined by the sum of contact points between the rolling elements and the rings, and the maximum contact stress at each of these points [28]. Hence, the load capacity of the bearing depends on the number and shape of these rolling elements, which can be spheres, cylinders, truncated cones, or barrels. These elements are manufactured via several stages of high reduction-rate plastic deformation such as hot rolling or drawing. Once the raw cast material is in the form of square sectioned billets, it is heat treated and cut into the right lengths so rolling elements can be cold-forged, machined, and heat-treated again to the right hardness [4].

Finally, bearing rings have the function of supporting or locating rotative or fixed components, whilst their inner faces have raceway grooves that constrain the passage of rolling elements. In the case of radial ball bearing, the grooves are slightly larger than the ball radius in order to provide greater load support and lower friction, or can have internal radial clearance to avoid end movement and restrict angular contact, as is the case of angular contact bearings [26]. Regardless of such groove design, rings are manufactured from seamless tube by hot-rolling, heat treating, machining, and grinding to the hardness and surface roughness requirements [4]. The material used for the rolling elements and the rings will be covered in detail in the next section.

Many different types of bearings exist depending on the load, speed, dimensions, lubrication, and temperature requirements. Deep groove ball bearings (fig. 2.1a) are versatile, robust, and widely used bearings that can operate at high speeds and accommodate axial loads due to the deep fitting of balls inside raceway grooves [29]. Angular contact ball bearings (fig. 2.1b) are designed to support combined axial and radial loads thanks to the shoulders on opposite sides at the inner and outer raceways [26]. Self-aligning ball bearings (fig. 2.1c) have a common concave outer raceway, two inner raceways and two rows of balls to allow for shaft misalignment, whilst maintaining low friction [29]. In contrast, cylindrical ball bearings (fig. 2.1d) offer a higher radial load capacity at moderate speeds and misalignment resistance due to the greater contact between rolling elements and rings and the slightly cambered profile across raceways, which eliminates stress concentrations. Tapered roller bearings (fig. 2.1e) are similar to the cylindrical ones but have both tapered raceways and rolling elements, which accommodate better heavy combined loads [30]. Spherical roller bearings (fig. 2.1f) are based on the same principle as self-aligning ball bearings but use barrel shaped elements, which allows a higher radial load capacity

whilst still being self-aligning. Needle bearings (fig. 2.1g) are essentially cylindrical roller bearings that incorporate thin and long rollers, which offer a lower load capacity but higher speed capabilities, oscillatory motion, and smaller radial dimensions [31]. Finally, thrust bearings (fig. 2.1h) have a contact angle of 90 °, operate at high speeds, and support axial loads [31].

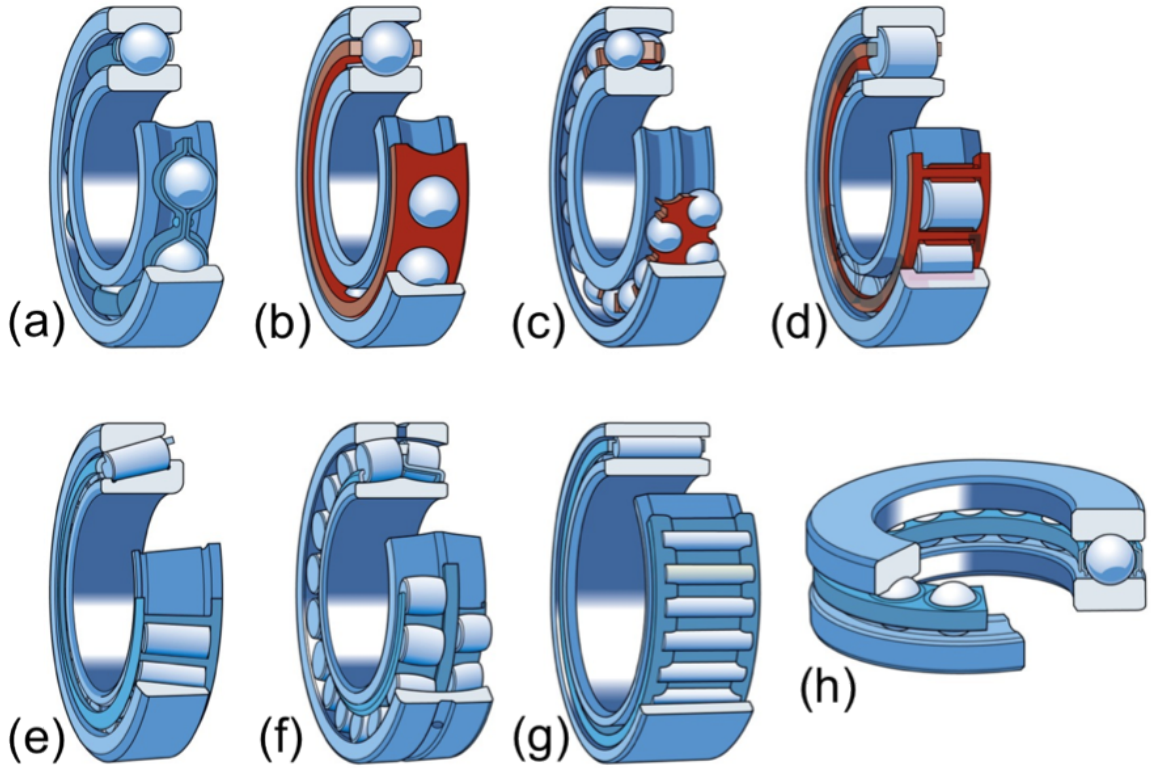

Fig. 2.1 Bearing configurations [30]: a) deep groove ball bearing, b) angular contact ball bearing, c) self-aligning ball bearing, d) cylindrical roller bearing, e) tapered roller bearing, f) spherical roller bearing, g) needle roller bearing, h) thrust ball bearing.

There are a number of handbooks [32] or manufacturers catalogues [29, 33] that assist in the selection of the appropriate bearing, beginning with the calculation of the normal and maximum loads, bearing speed at maximum load, housing misalignment, and shaft deflection. These data are then used to select a bearing type and size after which life is calculated and the selection process optimised to the smallest size that meets the requirements. Mounting, lubrication, and sealing arrangements also need to be established.

2.2 Bearing steel

The material used in bearing construction has to comply with a long list of requirements that includes aspects such as hardness, toughness, dimensional stability, microstructural homogeneity and cleanliness, corrosion and hydrogen resistance, fatigue and rolling contact fatigue properties, wear resistance, reliability, cost, and manufacturing considerations [3, 34]. Given the availability, low cost, hardenability, and tailorable mechanical properties of steel, it has long been considered as the material of choice for rolling bearing elements and rings [35].

As Zaretsky mentions, work by Stribeck and Hess on tool steels in the early 1900's indicated the suitability of high carbon and high chromium steels (1C-1.5Cr) for rolling bearing applications [35]. Since the initial manufacture in 1905 by Fichtel and Sachs, variations of 1C-1.5Cr steel, nowadays referred to as 52100 type steel, is the most widely applied bearing steel [4, 36]. The numerous alloy variations have been listed by Bhadeshia [4]. Nonetheless, most applications still rely on a handful of alloys chosen on the basis of operating temperature, corrosion resistance, and toughness (table 2.1). If the operating temperature is below 422 K (149 °C), the alloys of choice are through-hardened AISI 52100, case-carburised AISI 8620 or AISI 9310, and corrosion-resistant AISI 440C. For temperatures above 422 K (149 °C), the choices are through-hardened M50, case-carbonitrided M50NiL, and corrosion-resistant AMS 5749 [35].

Table 2.1 Composition (wt%) of several common bearing steels [4, 35].

Alloy	C	Mn	Si	Cr	Ni	Mo	V	S	P
AISI 52100	1.00	0.35	0.39	1.45	-	-	-	<0.025	<0.025
AISI 8620	0.21	0.80	0.25	0.50	0.55	0.20	-	<0.040	<0.035
AISI 9310	0.10	0.54	0.28	1.18	3.15	0.11	-	<0.025	<0.025
AISI 440C	1.03	<1.0	0.41	17.30	-	0.75	0.14	<0.014	<0.018
M50	0.80	0.30	0.25	4.00	-	4.25	1.00	<0.030	<0.030
M50 NiL	0.13	0.30	0.25	4.00	3.50	4.25	1.20	<0.030	<0.030
AMS 5749	1.15	0.50	0.30	14.50	-	4.00	1.20	<0.010	<0.015

Multiple studies on the significant impact of inclusions on bearing life, triggered a race to produce cleaner steels that would satisfy their ever increasing engineering requirements [36, 37]. Examples include the use of basic refractories in air-melting, careful selection of scrap metal for the electric-arc furnace, vacuum degassing, ladle metallurgy, stirring, usage of high-alumina ladle lining, shrouding (to isolate liquid steel from the oxygenated environment), and bottom filling of ingots [4, 38].

The steels can be manufactured through continuous or ingot casting. In the latter case, steel obtained by melting scrap metal in the electric arc-furnace is alloyed, ladle degassed, and refined. In continuous casting, steel from scrap melting or from the blast furnace, is blown with oxygen to remove phosphorus, transferred to the basic oxygen furnace to adjust carbon, degassed and refined, and fed to the continuous caster [4]. After these processes, the main impurities found in bearing steel are oxygen, titanium oxides and carbides, hydrogen, interstitial nitrogen and nitrides, and sulphur (in the form of manganese sulphides) [39–41]. Oxygen and nitrogen are limited to 10 ppm, whilst hydrogen is limited to only 1 ppmw [4, 42, 43].

Modern vacuum processing can be applied to reduce further the mount of non-metallic inclusions, entrapped gas, and trace elements [35]. Vacuum induction melting consists of remelting the steel under vacuum and high-purity refractories to remove impurities. In vacuum arc remelting, the ingot is used as an electrode, which melts under direct current discharge in vacuum. Electroslag refining can be used to limit the size of inclusions and the total concentration of phosphorus, which embrittles the austenite grain boundaries, by applying a high current through the ingot electrode which is dipped in a pool of superheated slag. As the molten ingot droplets move through the slag into the bottom of a water-cooled mould, the non-metallic inclusions of the ingot can be separated chemically by reaction with the slag or physically by flotation allowing the formation a new, homogenous, directionally solidified, and high-purity ingot [44–46].

After manufacture and hot rolling, 52100 steel is supplied in the spheroidised (fig. 2.2a) or divorced-pearlite condition to facilitate machining or forming. This initial microstructure will influence the kinetics of subsequent heat treatments, e.g. a fine dispersion of globular cementite creates a homogenous carbon distribution within the austenitised matrix [47].

Once the parts have been formed or machined, they are partly austenitised usually at 1113 K (840 °C) for 20 min, which leaves undissolved 3-4 wt% of the cementite leading to austenite with a carbon content of 0.7-0.8 wt%. Although austenite first appears at 993 K (720 °C) using low heating rates, only at temperatures of about 1313 K (1040 °C) for 20 min will the steel become fully austenitic [48, 49]. The complete dissolution of cementite is not necessary to enhance fatigue life, in fact, cementite improves the resistance to wear due to the "stand-out" effect where periodic lamellae act as barriers hindering the cutting or ploughing action of hard abrasive grit in ferrite [50–52]. The austenitisation temperature and time will influence the austenite grain size, which in turn determines the size of marten-

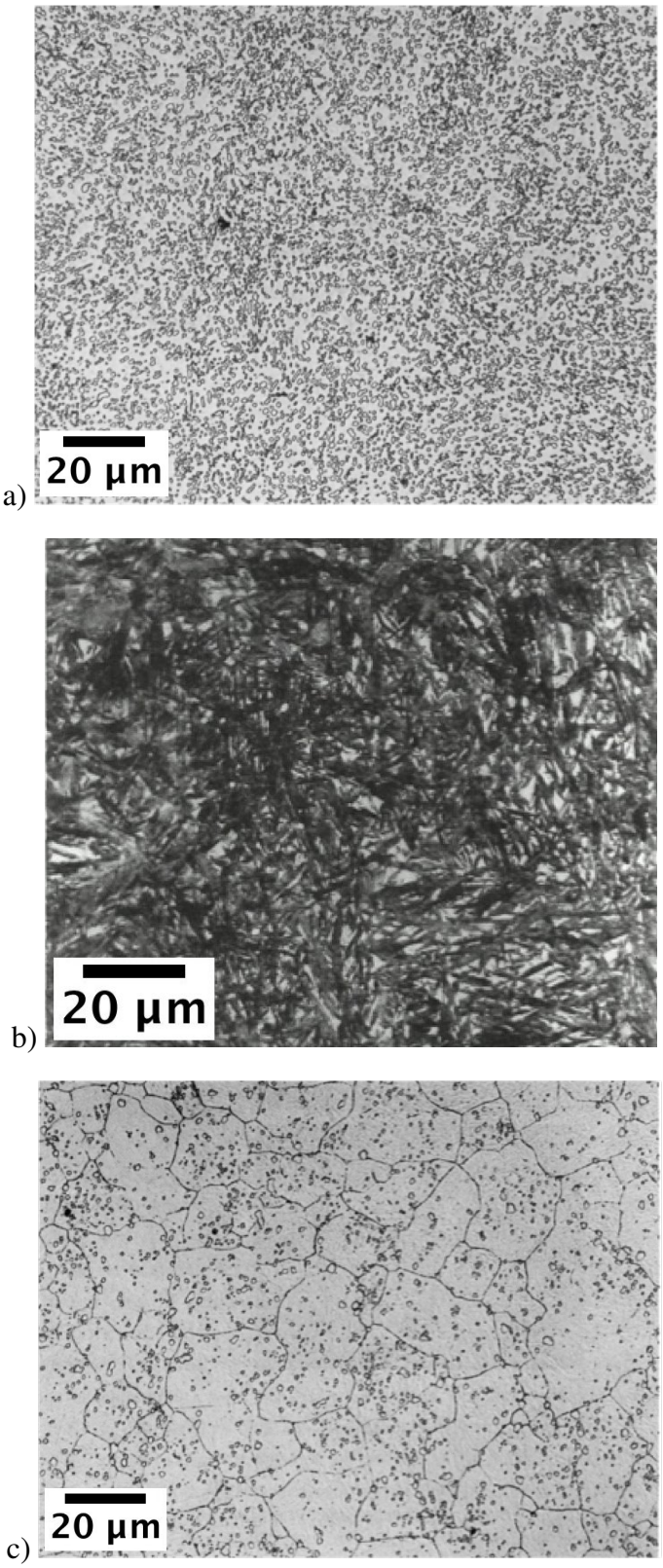

Fig. 2.2 52100 steel in the: a) as-received spheroidised condition, b) quenched condition containing untempered martensite, retained austenite, and residual carbides, and c) quenched and tempered condition etched with picric acid to reveal the prior austenite grain boundaries as well as residual and hardening carbides [28].

site plates upon quenching. The standard austenitisation treatment creates austenite grains of 40 to 60 μm [48], but can lead to coarser grains in the case of vacuum induction melted or vacuum arc remelted steels because of a reduction in the number density of inclusions [53]. Nevertheless, it is established that fine grains increase rolling contact fatigue life [54] and decrease the probability of microcracking, which will be discussed in the following subsection [55].

After austenitisation, bearing steel is normally quenched in oil at 333 K (60 °C) to form martensite (fig. 2.2b) [28] after which it will have a hardness of 59-66 HRC, a 0.2% proof strength of 1400-2200 MPa, and an ultimate tensile strength of 2150-2450 MPa [4, 56]. The mean hardness can be estimated by accounting for any other phases such as bainite, pearlite, and austenite, which have individual an hardness of 35, 29, and 17 HRC respectively [57]. Since the hardness is directly proportional to the life of the bearing, a fully martensitic microstructure with a minimum hardness of 58 HRC at the operating temperature is desired. In fact, a 3 HRC increase can result in a 35% life enhancement [35]. Life can be improved if the rolling elements are 2 HRC points harder than the raceways [32]. The substitutional solutes in 52100 steel give it sufficient hardenability with a depth of at least 5 mm becoming martensite on quenching into oil at 333 K (60 °C) [4].

Since the martensite-start temperature M_s depends on the amount of carbon dissolved during austenitisation, it can vary from 523 K (250 °C) in the case of the standard austenitisation at 1113 K (840 °C) down to 421 K (148 °C) when the fully austenitic state is quenched [28, 58]. Instead, the martensite finish temperature M_f is around 223 K (-50 °C)[1], where M_s is 523 K (250 °C), leading to 16 vol% of retained austenite [28]. A lower quantity of retained austenite, i.e. 2-5 vol% is preferable from the point of view of dimensional stability during service [35]. Compressive residual stress, which can be introduced by phase transformations or manufacturing processes like rolling, burnishing, and grinding, will increase the fatigue life [35].

In order to reach a balance of properties after quenching, 52100 steel is tempered at 433 K (160 °C) for 1 to 2 h (fig. 2.2c). This process improves toughness and precipitates a variety of transitional hardening carbides like η-Fe_2C, χ-Fe_5C_2, and ε-$Fe_{2-3}C$ depending on tempering time, whilst decomposing some of the retained austenite [4, 28, 59]. The fact that this steel can be tempered at such low temperatures limits the service temperature.

[1] This would require a cryogenic treatment in liquid nitrogen in order to diminish the amount of retained austenite, but such practice is not the standard for 52100 steel since it could lead to distortion or cracking [4].

Steels that retard tempering through the addition of silicon and molybdenum display increased rolling contact resistance, but have not been fully commercialised [60, 61]. Molybdenum counteracts the lack of toughness at the grain boundaries caused by phosphorus [4, 62].

2.2.1 Microcracks

The study of microscopic cracking in strong steels, including those used in the manufacture of bearings, has a significant history in the published literature. In high-carbon steels the martensite can crack when plates growing on different habit planes within the same austenite grain impinge (fig. 2.3) [55, 63–66]. The general consensus is that the austenite grain size (mean lineal intercept $\overline{L}_\gamma$), the amount of carbon in the martensite, and the transfer of stress between the martensite and austenite are important parameters in controlling crack formation [55, 62, 66, 67]. A large austenite grain size promotes martensite cracking, although it is reported that the quantity of cracking does not change much once $\overline{L}_\gamma \gtrsim 100\,\mu\text{m}$ [55]. This is consistent with the fact that the size of martensite plates scales with $\overline{L}_\gamma$, and once the austenite grain size becomes smaller than the stress transfer length of composite theory, it becomes difficult to transfer load onto the plates, thus reducing their tendency for cracking [66].

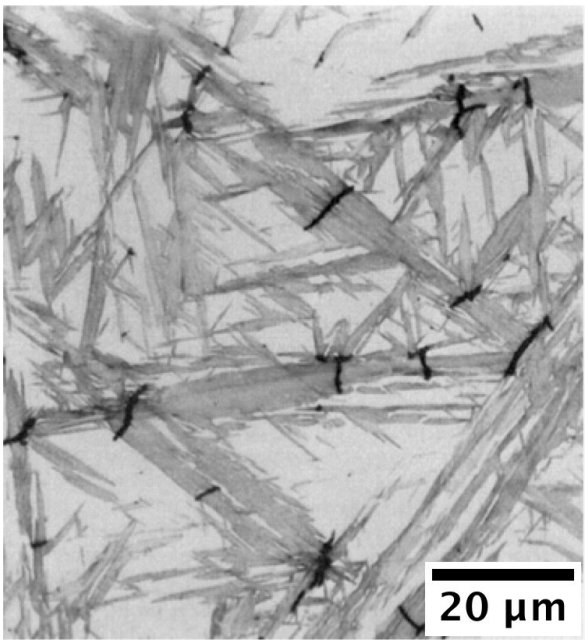

Fig. 2.3 Microcracks or martensite plate cracks in an Fe-1.39 wt% C steel etched with nital [64].

The susceptibility of martensite to brittle fracture naturally increases with its carbon concentration [62, 67] due to the well-known intense strengthening caused by the presence of carbon in interstitial solution in the otherwise body-centred cubic lattice of ferrite. There are secondary effects due to changes in martensite crystallography, which can alter the impingement angles between different variants [63]. Other forms of cracking that could be introduced deliberately include fracture at the γ-grain boundaries [68], often exacerbated by quenching stresses or impurity embrittlement.

2.2.2 Nanostructured bainite

Bainite is a microstructure in steels that forms by the displace transformation of austenite at temperatures above M_s, but below T_0. Such transformation is accompanied by a shape deformation, which is an invariant-plane strain with a large shear component. Three types of bainite can form: upper bainite (high temperatures), which is a non-lamellar aggregate of plate-shaped ferrite whose boundaries are decorated by elongated cementite, lower bainite (low temperatures) which has thinner interplatelet cementite but also fine carbide precipitates inside the ferrite, and carbide-free bainite where an addition of at least 1.5 wt% of silicon restricts the precipitation of cementite due to the low solubility of this element in cementite [69]. In both cases, bainite plates nucleate at the austenite grain boundaries and grow without diffusion creating plastic deformation of the austenite, which is thought to limit the length of the plates. Excess carbon is then partitioned into the residual austenite making the next ferrite plate grow from carbon-enriched austenite. The process will stop at the T_0 curve boundary[2] when diffusionless transformation becomes impossible even if the austenite has not reached it equilibrium composition. Therefore, this is described as an incomplete reaction [70].

Carbide-free nanostructured bainite consists of incredibly fine platelets of bainitic ferrite dispersed in matrix of carbon-enriched retained austenite (fig. 2.4) [9, 10]. The steel in its transformed condition can have a hardness in the range 600-670 HV, strength exceeding 2 GPa, and toughness levels of around 30-40 MPa $m^{1/2}$ [71–73]. This steel also exhibits high abrasive and rolling-sliding wear resistance [52, 74–81], optimal fatigue resistance in a variety of uniaxial tests [79, 81, 82], as well as hydrogen penetration resistance when the austenite content exceeds the percolation threshold [83]. In fact, the ability of the austenite to percolate the steel dictates also other factors such as the ductility [84] since there is a critical threshold of austenite fraction below which the material fractures during tensile

[2] Obtained by plotting the locus of the T_0 temperature against carbon concentration.

loading [85]. This material is currently used as armour but projects exist to expand its use to other critical applications such as jet turbine shafts and roller bearings.

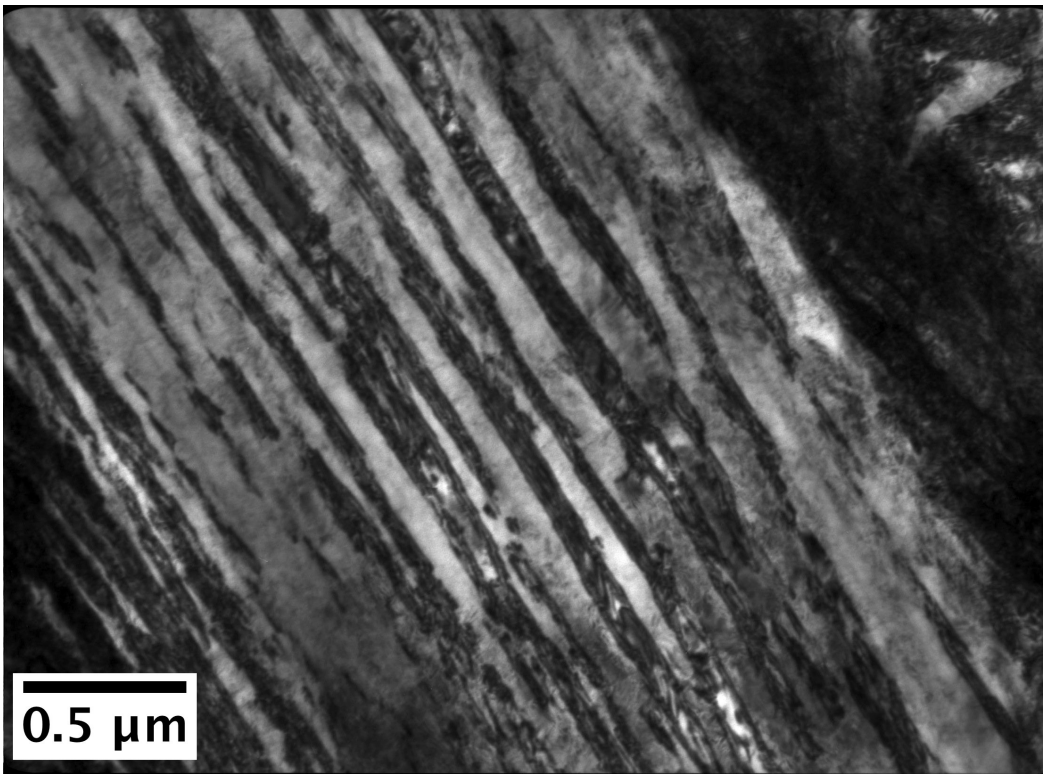

Fig. 2.4 Typical nanostructure of carbide-free bainite after transformation at 473 K (200 °C) for 10 days [86].

The typical heat treatment of superbainitic grades consists of homogenisation at 1473 K (1200 °C) for 2 days and slow cooling through the 973-823 K (700-550 °C) range to ensure pearlite formation and avoid martensite, which would induce quench cracks [87]. Austenitisation then takes place in the γ region 1173-1273 K (900-1000 °C) for $\sim$15 min before being cooled in air to the bainitic transformation temperature. The transformation time depends on the chemical composition and austempering temperature but the typical heat treatment is performed at 473 K (200 °C) for 10 days before being quenched in water at room temperature, and in some cases tempering also for different times and temperatures to study the kinetics of austenite decomposition [86, 88–91].

2.3 Bearing operation

The ability of a bearing to transmit load from the outer to the inner ring depends on the number of contact points between the rings and the rolling elements [28]. The position of the balls relative to the loading direction, will in turn determine the loading cycles perceived by each element. The load elastically deforms the surfaces of the rolling elements creating a contact area and thus, a stress distribution at the surface and subsurface. The loads experienced by the inner and outer rings depend on the position of the rolling elements relative to the loading direction. As explained by Voskamp, if there is a pure radial load applied to a rigid housing with no internal clearance, the load will be distributed over the balls of the upper semicircle of the bearing, which are four in the case of a single-row eight ball deep groove bearing [28]. Only in the case of maximum load induced stress amplitude, i.e. when a ball is located at the uppermost part of the raceway, the load will be distributed over one ball less and that uppermost ball, A, will be carrying the maximum load (fig. 2.5). Such a scenario does not apply if the elastic response of the shaft causes a bending moment or if the tight interference fit of the bearing to the shaft causes expansion of the inner ring.

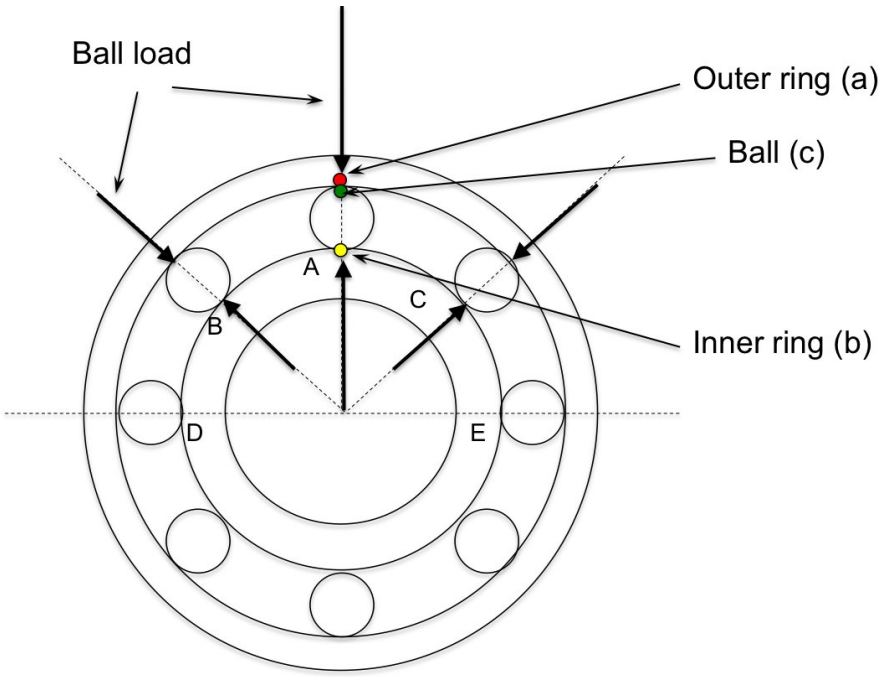

Fig. 2.5 Schematic representation of a radially loaded SKF 6309 deep groove ball bearing at the maximum loading condition depicting the load's magnitude distribution through the length of the load arrows and three stressed volume elements. It is assumed that the balls spin with an axis parallel to the bearing's axial direction. The outer ring is fixed and rotation is clockwise. Redrawn based on [28].

As the balls start to move, different loading cycles and contact amplitudes occur at the three volume elements represented by red, green and yellow dots in fig. 2.5. In the case of the outer ring, the red element will be loaded again by ball B at a full amplitude as shown in fig. 2.6. Instead, the green volume on the uppermost ball will experience its next contact with the inner ring at a lower amplitude followed by a contact with the outer ring at an even smaller load. Finally, the volume element at the inner ring represented by the yellow dot will experience its next contact with ball C at a lower amplitude, as both the ring and the ball are moving away from the highest loaded position. From this analysis, it is clear that every volume element in the outer ring experiences maximum stress during each cycle, so if the stress amplitude would be a determining factor in rolling contact fatigue life, failure would be expected predominantly in this component. However, bearing life is mostly limited by the damage initiated at inclusions located in the regions of maximum subsurface stress. Therefore, the smaller volume of material exposed to cyclic loading of the inner ring leads to an increased probability of finding a crack initiating inclusion of critical size in its stressed volume and thus, a higher risk of fatigue failure compared to the outer ring, despite the higher stress frequency and amplitude felt in the later (fig. 2.6) [28].

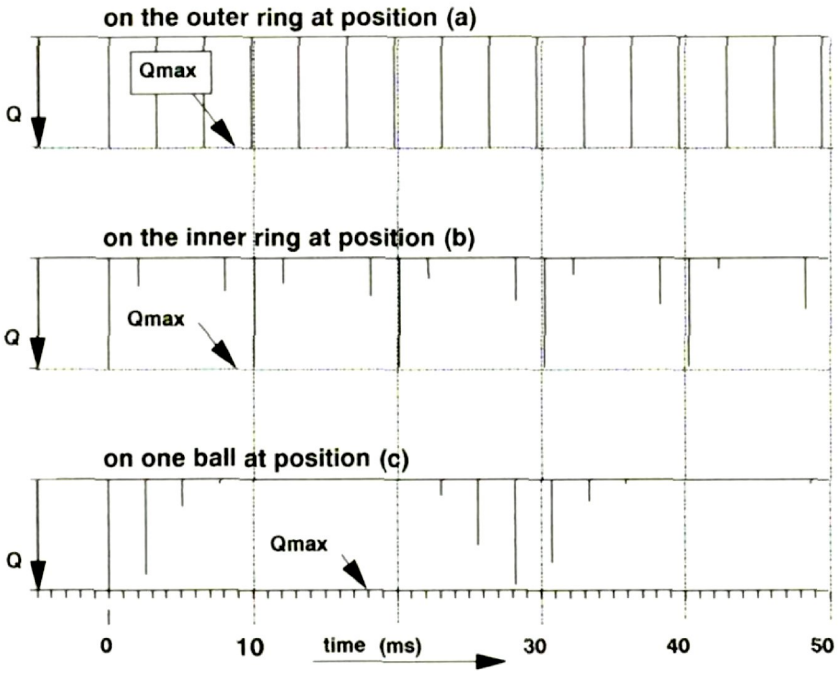

Fig. 2.6 Loading cycles of the three volume elements marked in fig. 2.5 where Q is the initial point of contact between the uppermost ball and the rings and Q_{max} represent the highest loaded positions. The rotation speed is 6000 rpm [28].

The load applied to bearings translates into stress through the contact area on the rolling elements and rings created by the elastic deformation of the material at the engineering scale (fig. 2.7). The dimensions of such elliptical area depend on the magnitude of the load, the number of balls in the bearing, the rigidity of the housing, the diameter of the balls, the radius of the raceway groove, the diameter of the ring, and the Young's modulus and Poisson ratio of the material [28]. In contrast to line contact models, Hertz contact pressure model describes the stress field at the surface of an elliptical contact area under a perpendicular force assuming frictionless bodies and elastic deformation, in the absence of surface shear stresses. Although operation does lead to smoothing down of surfaces, referred to as running in, and plastic strain reaches a steady state, referred to as shakedown, the differences in velocity experienced by the different points within the contact area give raise to shear stresses. However, experimental evidence suggests that subsurface stresses statistically determine fatigue failure [4, 31, 92, 93]. Jones incorporated these aspects into a triaxial subsurface stress model based on the Thomas and Hoersch method that determines the orthogonal shearing stress, the octahedral shearing stress, and the maximum shearing stress as a function of the maximum Hertz stress [35, 94, 95]. The von Mises-Hencky model determines, instead, the equivalent shear stress assuming a distortion energy criterion [96]. Since these shear stresses occur at different depths below the surface[3], the regions of most significant material alterations have tried to be linked to a particular stress. Whilst Lundberg and Palmgren attributed the orthogonal shear stress to be the cause of fatigue cracking, Voskamp concluded that it was the responsible for areas of intense phase transformations despite the fact that residual stress peak values occur closer to the maximum unidirectional shear stress [28, 97]. Given the disparities, the subsurface volume of interest (fig. 2.8) should be taken as the one contained between the depth range of the mentioned shear stresses, i.e. $0.5b$-$0.79b$ [35]. Detailed mathematical formulations of rolling motion and rolling contact can be found in [98].

The previously mentioned mechanisms of cyclic stressing will cause in the stressed volume, even during the first loading cycle, decomposition of the retained austenite into martensite and material flow parallel to the surface creating, in return, residual compressive stress in the axial direction [28]. Consequently, a normal stress develops perpendicular to the surface, which acts as a crack opening force, as a response to a thickness decrease of the

[3] If b is the semi-minor axis of the projected elliptical area of contact, the depth of the shear stresses in point (ball) contact are: $0.50b$ for the orthogonal shear stress, and $0.76b$ for the octahedral shearing stress and the maximum shearing stress. Instead, for line (roller) contact the depths are: $0.50b$ for the orthogonal shear stress, and $0.79b$ for the octahedral shearing stress and the maximum shearing stress [35].

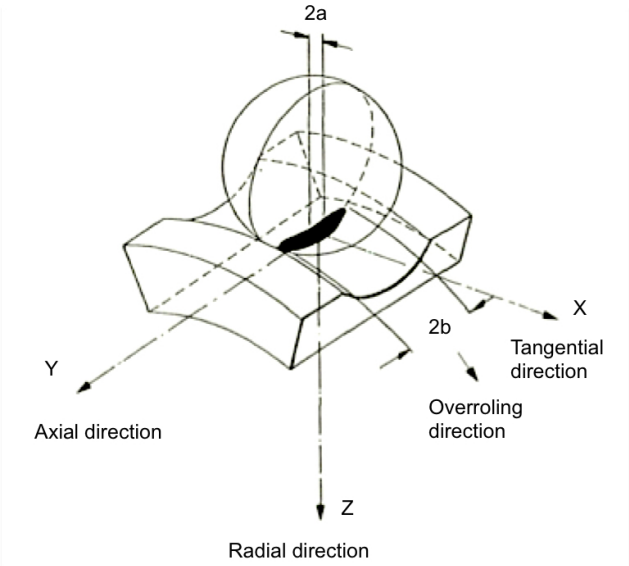

Fig. 2.7 Elliptical contact area formed by the radial load of the ball on the inner raceway groove due to elastic deformation. The contact area has a width of 2*a* in the tangential direction and a length of 2*b* in the axial direction [28].

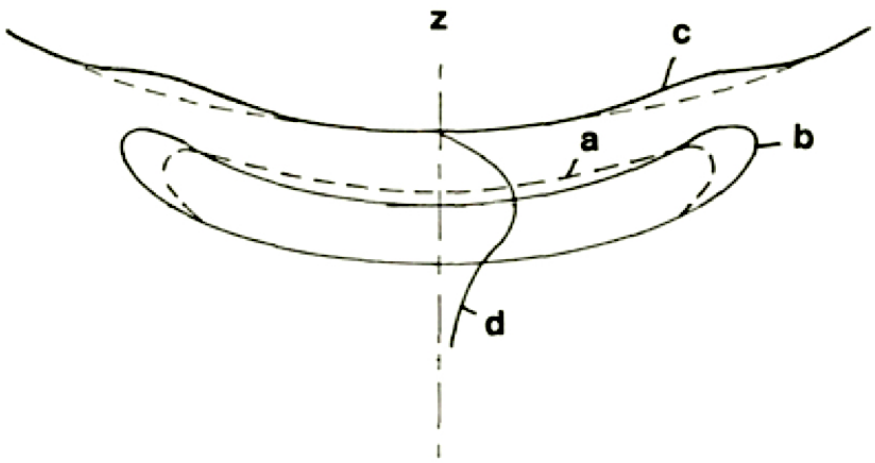

Fig. 2.8 Schematic of the stressed subsurface volume beneath the inner raceway surface depicting: a) the initial dimensions of the volume, b) the flattened and lengthened volume after material flow, c) upheavals in the surface created by the lengthening of the stressed volume, and d) the depth profile of a tensile radial component of residual stress perpendicular to the raceway surface [28].

deformed subsurface region (fig. 2.8). Despite the fact that contact stresses do not exceed the yield stress on the macro scale, accommodation of shape change in a small subsurface volume by local plastic deformation creates micro yielding and work hardening [99]. The hysteresis obtained in stress-strain cycles during push-pull tests corroborate this behaviour (fig. 2.9) where 99% of the energy is thermally dissipated and 1% is absorbed by strain causing microstructural alterations that will be described in the next section [100, 101]. Just like the results of fatigue tests such as rotating beam and push-pull cannot be used to asses rolling contact fatigue mechanisms [4], the magnitude of such temperature raise is only of a couple of degrees Celsius and should not be confused with the temperature increase due to sliding contact, crack rubbing, or deformation localisation.

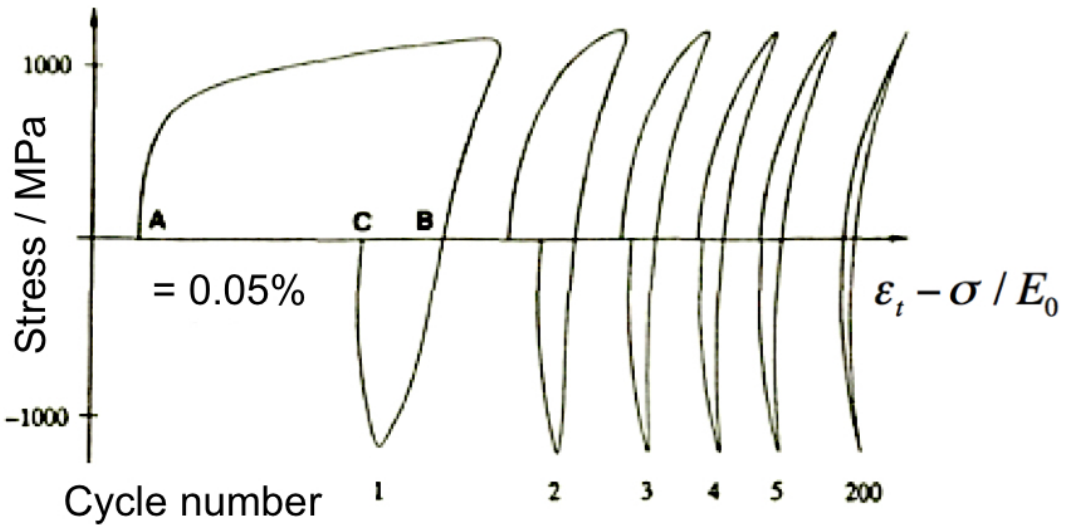

Fig. 2.9 Stress-strain cycles from push-pull test where the distance AC represents retained austenite (diminished after first cycle) and distance CB, which by contracting, illustrates progressive work hardening. The area inside the hysteresis loops corresponds to the energy dissipated. ε_t is the observed total strain, σ is the applied stress, and E_0 is the Young's modulus. Adapted from [28, 101].

The effect of cyclic plastic stressing of the bearing elements creates a scenario of metal fatigue, which is responsible for initiation and growth of cracks that can eventually cause failure [102]. In the case of bearings steels, their brittle nature implies a fatigue life dominated by the crack initiation stage and a lack of a fatigue limit based on the Palmgren-Miner rule, meaning that failure can occur at low stress levels if the cycles are large enough [28, 103, 104]. This occurs due to the inability of these steels to strain-age when stress

concentrators allow dislocations to remain mobile despite interstitials [4]. Bearing steels, instead, exhibit an endurance limit and large compressive stresses at their surfaces caused by machining or grinding that transfer the fatigue initiation sites to the subsurface [105].

Based on the previous descriptions, rolling contact fatigue (RCF), in the case of bearings, can be summarised as the cyclic loading of the raceways by the repeated passage of rolling elements that induce Hertzian contact stresses responsible for phenomena such as the decomposition of retained austenite, smoothing of surfaces, steady-state plastic strain, texture development, residual stress development, work hardening, and surface or subsurface crack initiation and propagation. Rolling contact fatigue models are based on failure via detachment of material (spalling) due to surface or sub-surface cracks and surface roughness (distress). Lundberg and Palmgren determined the life of a bearing through a formula based on Weibull statistics, which expresses as a probability, the life in millions of inner race revolutions that 90% of bearings in a population should equal or exceed before the first sign of rolling contact fatigue damage (spalling) occurs [97]. This basic rating life, which has probabilistic and not a physical basis, is expressed as:

$$L_{10} = LF\left(\frac{C}{P}\right)^{n} \tag{2.1}$$

where C is the theoretical load a bearing can carry for 1 million inner race revolutions with a 10% probability of failure, P is the actual operating load, n is a load life exponent depending on the type of bearing, and LF is the total life factor, phenomenologically introduced by Ioannides and Harris, that takes into account the effect of material parameters on reliability. The total life factor is the multiplication of individual factors, shown in tables 2.2, that consider rolling contact fatigue life limiting aspects such as processing routes (table 2.2a), steel used (table 2.2b), residual stresses (equation 2.2), and hardness at operating temperature (equation 2.3 and table 2.2d) [35, 97, 106]. More detailed information on life factors can be found in [107].

a)

Processing	Life factor, LF_a
Air melting (AM)	1
Vacuum processing (VP) or carbon vacuum degassing (CVD)	1.5
Vacuum arc remelting (VAR)	3
Electroflux remelting (EFR) or electroslag remelting (ESR)	3
Vacuum arc remelting-vacuum arc remelting (VAR-VAR)	4.5
Vacuum induction melting-vacuum arc remelting (VIM-VAR)	6

b)

Material	Life factor, LF_b
Through-hardened steels	
AISI 52100	3
AISI M10	2
AISI M50	2
AISI T1(18-4-1)	2
Halmo	2
AISI M1	0.6
AISI M2	0.6
Corrosion resistant steels	
AMS 5749 (BG-42)	2
AMS 5900 (CRB7)	2
AISI 440C	0.6
Case-carburised steels	
AMS 6278 (VIM-VAR M50 NiL)	4
AISI 4620	3
AISI 8620	2
AISI 9310	2
CBS 600	2
Vasco X-2	2
CBS 1000	2
AISI 8720	1.5

c)
$$LF_c = \left[\frac{\tau_{max}}{\tau_{max} - \frac{\sigma_r}{2}}\right]^c \tag{2.2}$$

d)
$$LF_d = e^{0.1\left[(H_{RT}-60)-C_1(T_T-T_{RT})^{C_2}\right]} \tag{2.3}$$

	Material	Temperature range / K (°C)	C_1	C_2
	AISI 8620	294-589 (21-316)	73×10^{-5}	1.7
	CBS 600	294-589 (21-316)	0.75×10^{-5}	2.4
	Vasco X2	294-811 (21-538)	1.4×10^{-5}	2.2
	CBS 1000	294-811 (21-538)	93×10^{-5}	1.5
	CBS 1000M	294-811 (21-538)	340×10^{-5}	1.3
	Super Nitralloy	294-600 (21-327)	1.3×10^{-5}	2.3
	AISI 52100	294-533 (21-260)	92×10^{-5}	1.6
	AISI M50	294-811 (21-538)	133×10^{-5}	1.4
	AISI M1	"	"	"
d)	AISI M2	"	"	"
	AISI M10	"	"	"
	AISI M42	"	"	"
	AISI T1(18-4-1)	"	"	"
	Halmo	"	"	"
	WB-49	"	"	"
	WD-65	"	"	"
	Matrix II	"	"	"
	AISI 440C	"	"	"
	AMS 5749 (BG42)	"	"	"
	AMS 6278(M50 NiL)	"	"	"

Table 2.2 Life factors depending on the: a) processing routes, b) type of steel used, c) compressive residual stress (the c exponent is typically 9), and d) hardness at operating temperature where H is the Rockwell C hardness and the subscript T stands for the operating temperature and RT for room temperature both in °C. C_1 is a material constant and C_2 a material exponent. These values are normalised for air melt AISI 52100 steel tested at a contact stress of 1.7 GPa [35, 36].

2.4 Consequences of bearing operation

As briefly mentioned in the previous section, cyclic stressing of bearing steel can cause microstructural changes, which then have damaging macroscopic consequences on the life of bearings. Whilst 36% of all premature failures can be blamed on inadequate lubrication, most subsurface degradations can occur under correct operating conditions, but threaten the predicted life of the components [33]. Evidence of this has been presented in the case of large bearings in gearboxes of wind turbines [3]. In this section, the geometrical and microstructural degradations of bearing steels will be discussed in an effort to elucidate their underlying principles.

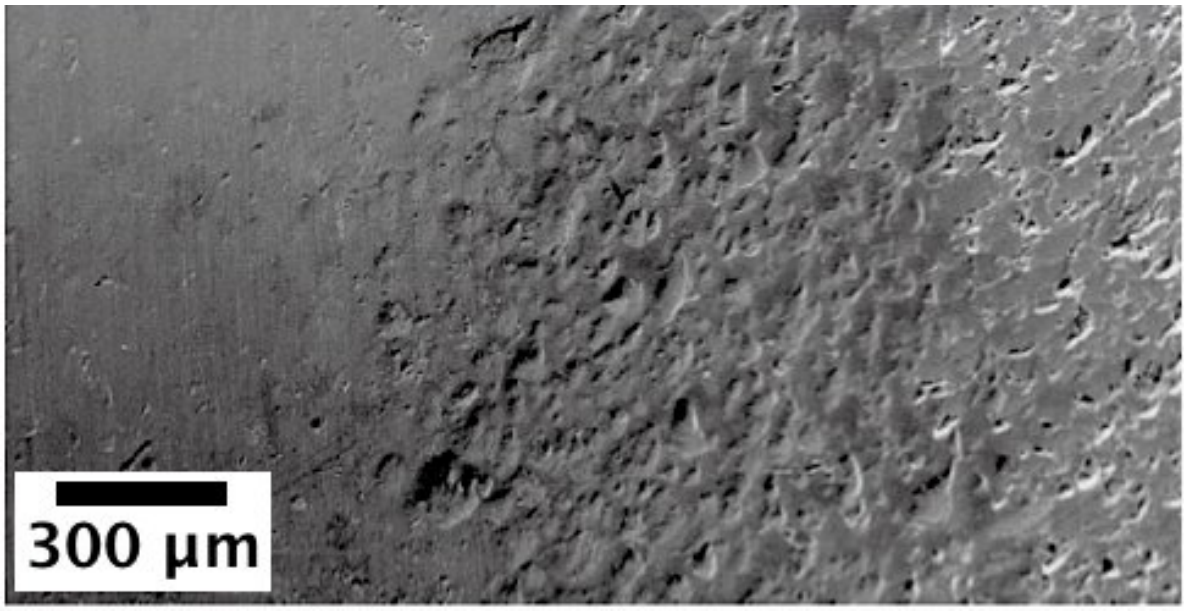

Fig. 2.10 Surface distress created by particle-contaminated lubricant [108].

Rolling contact fatigue is manifested mainly through two types of geometrical damage: surface distress and spalling. Particle-contaminated lubricants or a breakdown of the lubricant film will cause surface distress when small particles indent the surface in an inhomogeneous micro-plastic deformation manner [28]. These pits will lead to small surface cracks, which develop into shallow craters or cause bits of surface material to flake off (fig. 2.10) [4, 108]. Instead, spalling can be caused by surface or subsurface cracks, which cause chips of material, orders of magnitude larger than the surface distress flakes, to be removed from the surface. Normally initiated at the interfaces of non-metallic inclusions, voids, or carbide stringers, subsurface microcracks can branch off towards the surface by coalescing with other microcracks until they form an oval shaped spall [4, 93, 109]. On the contrary, surface spalls, which have more of a fan shape, can appear despite the compressive surface stresses of bearing elements, due to the influence of stress concentrators, thermal damage, large indented particles, and the combination of rolling contact and bending or sliding [93, 110]. Such surface cracks can propagate by action of the lubricant that penetrates the crack and transmits the contact load to its tip in a tensile manner [28]. This action can increase the dimensions of the spall and thus, create debris that can get entrained in the raceways and exacerbate damage. Although retained austenite has been shown to improve rolling contact fatigue life [51] and fatigue crack propagation [111], large quantities of it can cause “capping” when balls lose a portion of the case material [35].

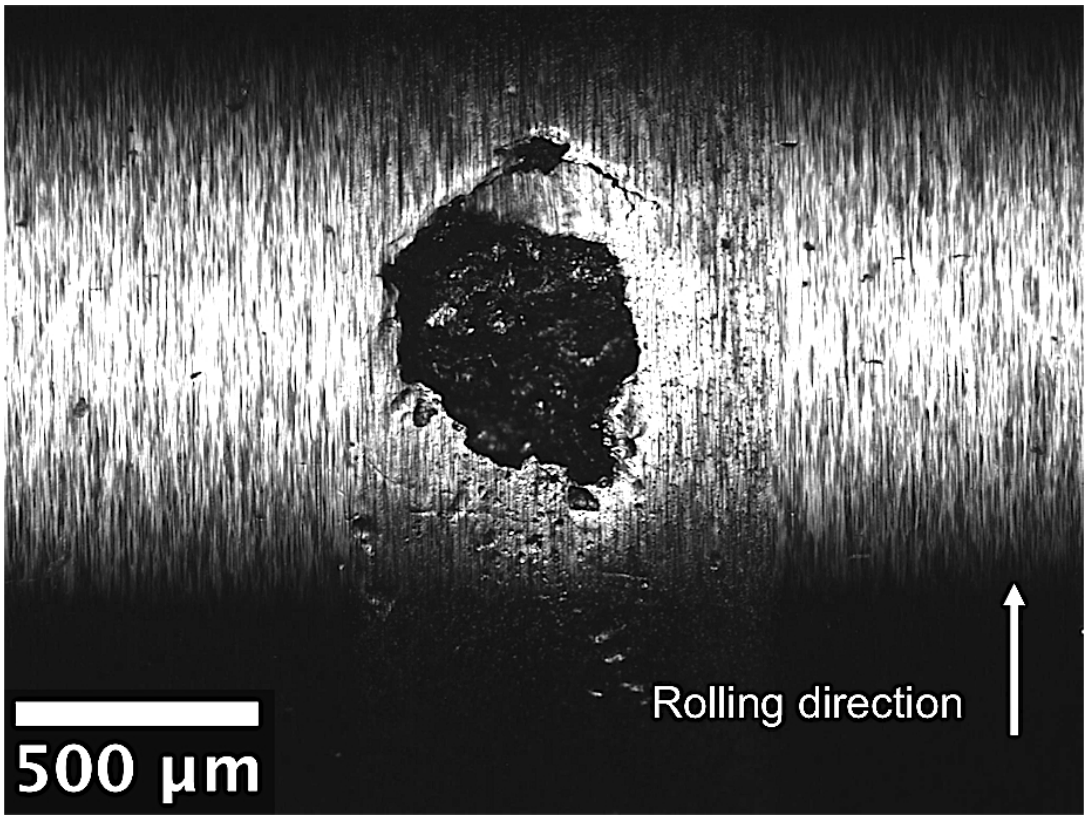

Fig. 2.11 Spall damage on the surface of a rod tested at 5.7 GPa for 7×10^7 cycles. The rolling direction is from bottom to top as depicted by the sharper leading edge. The upheaves created by the indent and the successive impact of the ball against the depressed area of the spall create the surface cracks behind the leading edge, which might help to propagate the spall by breaking off along the direction of motion.

2.4.1 Dark-etching regions

Despite the fact that geometrical damage leads, unequivocally, to failure, it is the microstructural damage, which is more intriguing as it is commonly attributed to be the cause of failure and an early symptom of damage. The sequence of microstructural alterations in bearings is revealed through changes in the etching response and generally starts with the appearance of a dark etching region (DER) in the subsurface range of maximum orthogonal shear stress (fig. 2.12a). This region appears dark under the optical microscope due to its structure of long disc-like cementite particles embedded in a cell structure of deformed and misoriented martensite plates where fine hardening carbides have dissolved during cyclic deformation and reprecipitated as ε-carbide, effectively over-tempering the material (fig. 2.12b) [112, 113]. In fact, DER are not observed if the steel is initially fully tempered to 57 HRC [4].

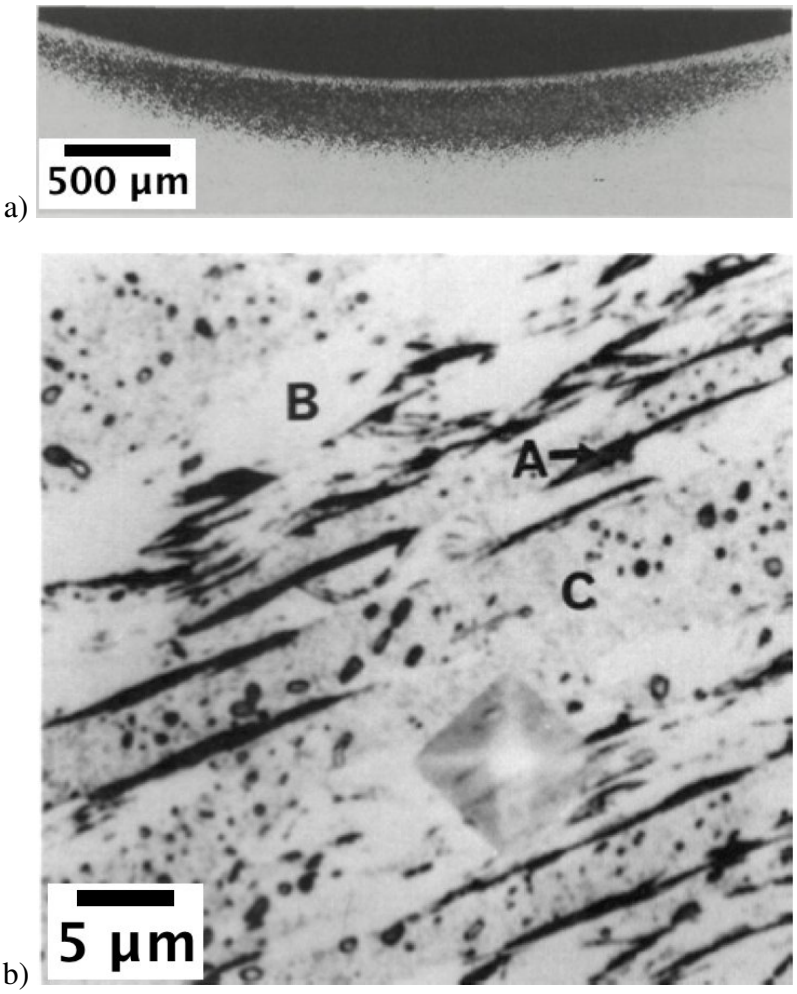

Fig. 2.12 Dark etching matter seen a) macroscopically at the subsurface of a bearing's inner ring [28], and b) etched with carbide etchant showing carbide discs (A), cell ferrite (B), and DER phase (C) [114]

Given the lower hardness of the dark etching region[4], this structure is said to be the result of cyclic softening, which is the process of mechanical removal of excess dislocations [113, 115]. The prolonged rolling contact softening caused by the decay of martensite to cell structured ferrite and the extensive carbon redistribution counteracts initial hardening caused by cyclic stressing and retained austenite decomposition upon loading [4]. This loss of hardness decreases the yield stress of the material by increasing the volume fraction of deformable material [28]. Furthermore, this decay is accompanied by a slight decrease in specific volume, which generates internal tensile stresses that oppose the compressive

[4] 53 HRC compared to the original value of 64 HRC [113].

stresses induced by the volume expansion of austenite decomposition. The occurrence of residual stress at such highly localised plastically-deformed subsurface regions creates three different deformation textures in the dark etching region [28]. Room temperature rolling contact related to a high deformation mode with no recovery, causing material displacement of less than 5 µm, creates a $\{100\}< 011 >$ texture. Instead, rolling contact above 318 K (45 °C) gives rise to a $\{111\}< \bar{2}11 >$ texture that may be due to bursts of dissipated energy and localised temperature peaks that trigger recrystallization. This texture comes in hand with a reduction of residual globular cementite. Finally, a weak $\{221\}< 11\bar{4} >$ texture can develop only in conjunction with $\{100\}< 011 >$ as the result of twinning. In other words, the appearance of dark etching regions is influenced by the stress level, the operating temperature, and the initial heat treatment [28, 116]. For example, lengthy tempering treatments lead to a loss of coherency of epsilon carbides in the matrix and reduction of microstrain, which diminish the dark etching response [28].

2.4.2 White-etching matter

Further rolling contact operation gives rise to regions inside the dark etching matter that reveal no internal contrast when etched in nital known as white-etching matter (WEM). This microstructural degradation can lead to the premature failure of bearings through a mechanism called “white-structure flaking" (WSF). White-structure flaking is a bearing failure mechanism associated with white-etching matter, that leads eventually to flakes of material detaching from the raceway surface. Such damage has been identified as one of the possible causes of the premature failure of large bearings, such as those in wind-turbine gearboxes [3]. White-etching matter is a generic term describing microstructural damage that exhibits lighter contrast relative to the surrounding material, when an etched sample is observed using optical microscopy. White-etching matter encompasses the so-called butterfly wings, some cracks, white-etching spheres, bands, all caused by rolling contact fatigue in the subsurface of bearing raceways or white-etching layers caused again by rolling contact fatigue of railway tracks or by hard turning (fig. 2.13), as reviewed in [4].

White-etching matter not only occurs in through-hardened martensitic 52100 steel, but also in bainitic 52100, case-hardened 52100, pearlitic steel, and high speed tool steel, amongst others [3]. This matter has several manifestations, but two main types have been identified: soft and hard [4]. Soft white-etching matter such as the one in low and high angle bands exhibits lower hardness than the matrix [119], can be transgranular [28], is composed by fine equiaxed grains ($\sim$ 20 nm) [120], has non-crystallographic or amorphous regions and microvoids, whilst the material adjacent to the band has a high dislocation

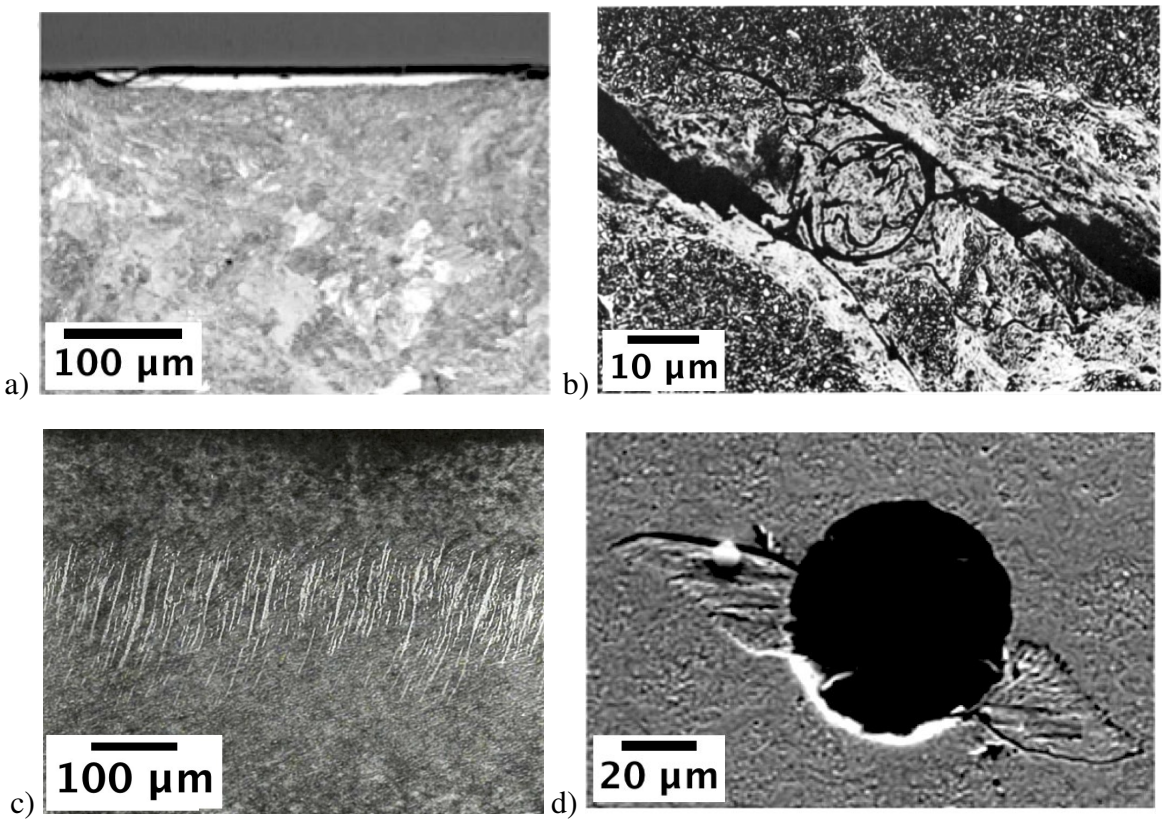

Fig. 2.13 Different representations of white etching matter including hard manifestations such as: a) layer [117], b) sphere [118], and d) butterfly (SEM) [2] or soft ones like c) bands [28].

density [121]. White-etching bands have also been found to be depleted in carbon [119] either through the diffusion of carbon into the surrounding dark-etching regions which then gets trapped by dislocations or precipitates as cementite [122], or through the unpinning of dislocations from their carbon atmospheres that leaves a supersaturated ferrite which then promotes partitioning and precipitation as cementite outside the bands [123]. During rolling contact, low angle bands develop first at orientations of 20 to 32 ° depending on depth, have a thickness of the order of 1 µm and a length larger than the austenite grain [28]. High angle bands develop later at orientations of 75 to 85 ° depending on the rotation speed and have a thickness of up to 20 µm. These two orientations are related to the way principal axes of stress and strain rotate as the balls displace over the rings [124]. In either case, these bands are not associated with cracks or surface disconnections such as hard white-etching matter and occur only in conjunction with the dark etching region $\{111\}<\bar{2}11>$ texture [4, 28].

Instead, hard white-etching matter found in layers, butterflies, cracks, or spheres, has a higher hardness than the matrix (30-50%) [117, 125], is supersaturated in carbon as a result of carbide dissolution [118], has a structure of fine martensite [117] or equiaxed nanoferrite grains [116, 121, 126], and is free of large carbides [112, 126]. White etching layers of this kind have been found in hard-turned steel or rail steel suggesting either high frictional contact that heats up the steel[5] and creates fine austenite grains which partially transform to martensite or severely deformed ferrite in which cementite dissolves by mechanical alloying [117, 127, 129]. Although the presence of such layers increases wear resistance, they leave the surface in a state of tension, which decreases rolling contact fatigue life [130]. In the case of butterflies, hard white-etching matter wings originate at voids, non-metallic inclusions, carbides, or microcracks already at 5-10% of the L_{10} life and at 45 ° to the over-rolling direction (fig. 2.14) [3, 131]. Just as in the case of white-etching cracks and spheres [3], white-etching wings consist of minute grains as a result of recrystallisation and cementite dissolution due to the increase of its interfacial energy when it gets fractured by slip steps [4, 5, 128]. A thorough study by Marze and co-workers revealed that butterflies form on ever smaller inclusions as more cycles pass reaching the minimum apparent diameter of 3 µm after which saturation of butterflies occurs at the region of maximum shear stress (1.3 mm deep) and the position of butterfly development shifts to closer to the surface (100 µm deep). Butterflies can only be seen as such if they originate from spherical inclusions and are seen through a longitudinal cut [132]. Horizontal cuts will reveal them

[5]The magnitude of this temperature increase has been discussed extensively [117, 127, 128]. It has been theoretically predicted to be between 477-503 K (204-230 °C), although some authors have concluded it reaches 573 K (300 °C) by analogy with mechanical alloying [127, 128]. Others claim, through simulations, that it can reach 1463-1573 K (1190-1300 °C) [4, 117].

as flakey white regions surrounding an inclusion. Nonetheless, if the inclusion is not spherical but rod-shaped, white regions can develop as a helix around it (fig. 2.14b and 2.14c). The exact shape of subsurface butterfly WEM wings and cracks, was recently presented by Evans et al who performed thorough characterisation of this microstructural degradation by performing serial sectioning, tomography, and 3D reconstructions [133, 134]. They concluded that white-etching wings and cracks are formed in the subsurface by inclusions and then link into large crack networks than can reach the surface and lead to flaking.

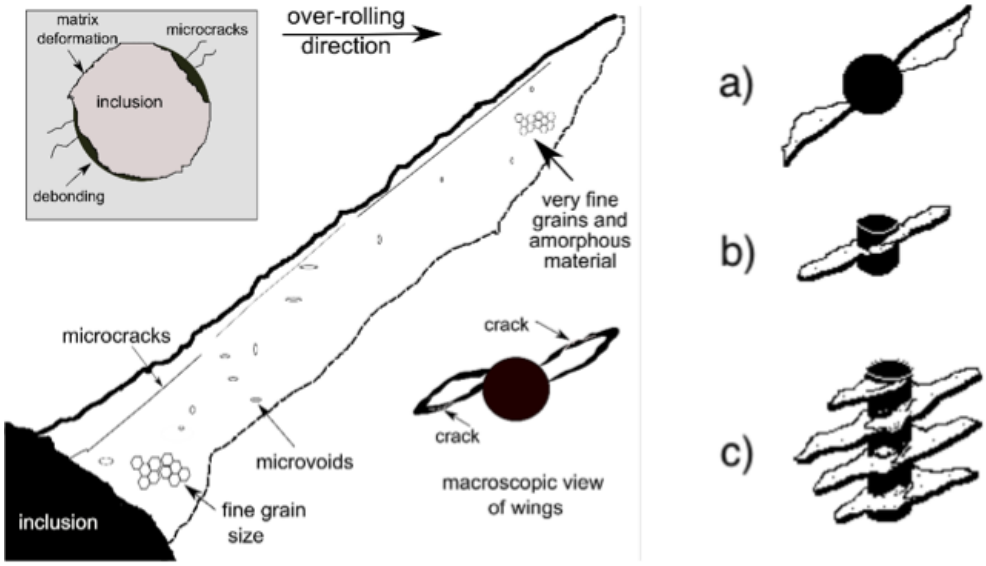

Fig. 2.14 Schematic of the structure of a butterfly wing depicting a straight interface where minute grains (10-50 nm) grow up to 100 nm close to the wavy interface [2, 4]. Within the wing, other defects like microvoids and fragmented cementite particles are present. Figure a) depicts wings developed in a spherical inclusion, b) wings in a cylindrical inclusion, and c) wings in a long cylindrical inclusion according to [132].

Several mechanisms have been proposed to explain the formation of WEM. The hard layers are associated with severe, localised plastic deformation with the possibility of some dynamic recovery [135–137]. The white-etching layers on railway tracks where rolling contact and sliding dominate the damage process, some authors consider carbide dissolution under the influence of deformation to be the primary mechanism [138] whereas others conclude that the structural change is due to rapid reaustenitisation followed by martensitic transformation [127]. An alternative interpretation relies on the formation of adiabatic shear leading to localised severe plasticity [139], although there are difficulties in reconciling the onset of adiabatic shear with the observed band dimensions and necessary strain rates [4].

There have also been reports that the process of WEM formation involves a combination of corrosion fatigue, hydrogen ingress and the tribochemical dissolution of inclusions [140]. The fundamental question that needs to be addressed is whether the white-etching regions are a cause or symptom of the onset of damage; this is the issue addressed in the following chapters of the present work.

2.5 Hydrogen embrittlement

The ingress of hydrogen leads to a severe degradation of the mechanical properties of bearing steels, even at concentrations as small as 1 ppm [7, 8]. In the case of bearings, hydrogen can cause premature failure at 1-10% of the expected life (L_{10}) through embrittlement, which exacerbates the appearance of white-etching matter [3, 7]. This white-etching matter is therefore seen as a form of damage whereby repeated deformation mechanically homogenises the structure and reduces its length scale to the nanometre range. The hydrogen that enters the steel can be generated by the decomposition of lubricants, through corrosion reactions, or exposure to hydrogen sources; this is why even 10 ppmw of water dissolved in lubricant can be harmful [141–144].

Once inside the steel, hydrogen can be mobile or not. Mobile hydrogen or diffusible monoatomic hydrogen can move freely around the lattice or get weakly trapped by reversible traps and so can escape the steel at room temperature after a few days [145]. Instead, non-mobile hydrogen is trapped at irreversible traps, which can be attractive, physical or combined [146, 147]. An attractive trap, attracts hydrogen through tensile stress fields (grain boundaries, inclusions, dislocations, crack tips, carbides), electrical fields, or temperature gradients, whereas a physical trap is one that is encountered by the random walk of hydrogen (voids, retained austenite) [148]. Given the low overall concentration of hydrogen that embrittles steel, many of the mechanisms that explain the effect require the accumulation of hydrogen by diffusion towards regions of the steel where the stress is focussed [149, 150]. The resulting increase in hydrogen concentration there leads to, for example, localised plastic instability and failure, but it is noteworthy that this also requires the diffusion of hydrogen to maintain crack propagation [149]. This is the reason why it is diffusible (monoatomic) hydrogen that causes harm. Hydrogen which is strongly trapped or present in molecular form can be considered in most cases to have been rendered harmless [146, 147].

Besides localised plastic instability, there are several other theories to explain the detrimental effects of hydrogen, for example, hydrogen embrittlement or hydrogen-enhanced

decohesion [149, 150]. Localised plasticity is argued to be caused by the stress field at the crack tip that attracts hydrogen, which softens the region by enabling slip and forming numerous ductile voids that link up to give it a macroscopic brittle fracture appearance. This mechanism conflicts with hydrogen embrittlement in which hydrogen promotes cleavage fracture by raising the brittle-ductile transition temperature or with the decohesion theory that claims that hydrogen weakens the atomic bonding of iron creating brittle failure with negligible localised deformation [151]. In any case, it is clear that hydrogen must be either not allowed to enter the steel or be irreversibly trapped if it does, in order to make it innocuous [4].

Chapter 3

Controlled cracking of 52100 steel

3.1 Introduction

Although most of the research performed in bearing steel metallurgy aims to prevent crack nucleation and propagation, some applications require the exact opposite in order to study the role that disconnected surfaces inside the bulk material play when load is applied, or when fluids entrapped in surface cracks propagate tensile stresses or exacerbate corrosion. Four heat treatments have been designed to create controlled arrays of crack types and distributions in a quenched and untempered steel normally used in the manufacture of bearings. The varieties of cracks studied include sparsely distributed martensite-plate cracks, fine grain boundary cracks, abundant martensite-plate cracks, and surface breaking cracks. The intention was to create samples which can then be subjected to appropriate mechanical testing so that phenomena such as the appearance of hard “white-etching areas" or “white-etching cracks" and hydrogen trapping can be studied further.

3.2 Experimental Methods

The material used in this study is a hot-rolled and spheroidised 52100 steel (table 3.1) manufactured by Ovako as a 60 mm diameter rod, from which cylindrical samples 120 mm long and 10 mm in diameter were machined for the purposes of heat treatment. The austenite grain size was determined using thermal etching [152] on a thermomechanical simulator Thermecmaster Z on cylindrical samples 12 mm long and 8 mm. The mean linear intercept $\overline{L}_\gamma$ was measured from optical micrographs of the thermally-etched samples, with sufficient measurements to ensure a standard error of the mean $< 1\%$. These results were corroborated using image analysis software that computes the area of enclosed regions.

The heat treatments designed to induce cracks were carried out using a standard Carbolite RWF1200 box furnace, with the temperature monitored using K-type thermocouples spot-welded to the samples. The quenchants used were air, water, and GP460 oil at different temperatures. The volume of the oil used was approximately 10 l; the oil had a density at 288 K (15 °C) of 904 kg m^{-3} and a viscosity index of 98 (ISO 2909). After oil quenching, samples were rinsed in water at ambient temperature.

Table 3.1 Chemical composition, wt%, of the 52100 steel used.

C	Cr	Mn	Mo	Si	Ni	Al	P	S	Cu	Co	Ca	Ti
0.98	1.38	0.28	0.06	0.28	0.18	0.04	0.01	0.017	0.21	0.015	0.001	<0.001

Vickers hardness tests were carried out using a Vickers Limited HTM 8373 hardness machine and a 30 kg load; the values reported correspond to the mean and standard error of the mean based on ten indentations. Surface cracks were created through Vickers indents with a 130 kg load.

Optical microscopy (OM) using a Zeiss microscope on samples prepared to a 1 μm finish was conducted in both the etched (2% nital) and unetched conditions, in the latter case to ensure clarity in the detection of cracks.

3.3 Results and discussion

The initial microstructure (fig. 3.1) has a hardness of 193±2 HV30 and consists of ferrite grains and spheroidised cementite particles, the later ranging from 0.5 to 2 μm, consistent with reported data [153]. The size of the ferrite grains and cementite particles will determine the austenite grain size, as discussed in the following section, specially if the austenitisation conditions are not sufficient to dissolve the cementite [47].

3.3.1 Prior austenite grain size determination

The austenite grain size was characterised in two ways (table 3.2): a mean lineal intercept determination is relevant because it is a fundamental measure of the surface per unit volume, and the second method involved image analysis to obtain a “grain diameter". In this second method, the software computes the area in pixels of enclosed regions and the measure is then translated into micrometres through a scale. By assuming a circular shape of grains,

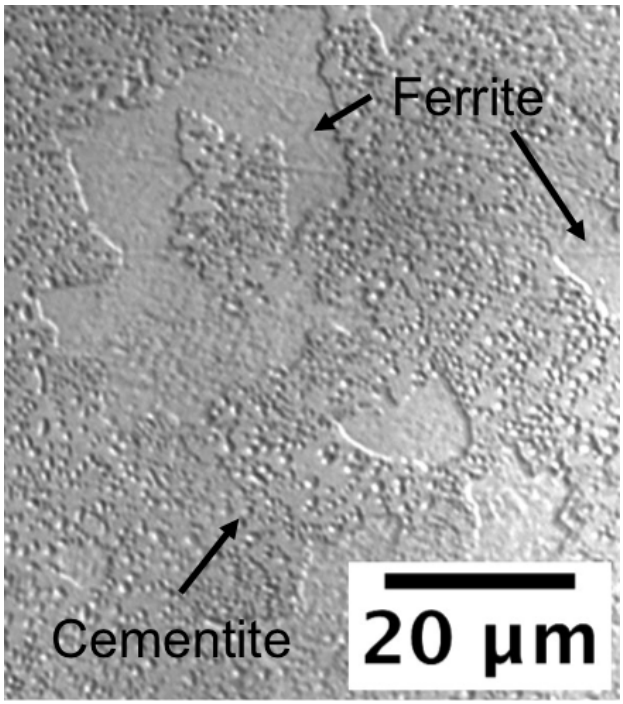

Fig. 3.1 As-received 52100 steel in its spheroidised condition, consisting of a mixture of cementite particles and ferrite.

the diameter or grain size was computed. In both cases, there is a potential uncertainty caused either by faint contrast or twins. The sizes obtained were within the ranges found in the literature of 40-60 µm after austenitisation at 1313 K (1040 °C) for 20 min [4].

Table 3.2 Average and standard deviation of prior austenite grain sizes for different analytical methods.

Method	Austenitisation treatments	
	1223 K (950 °C), 10 min	1373 K (1100 °C), 10 min
Mean linear intercept	19±5 µm	49±33 µm
Grain diameter	16±9 µm	39±27 µm

The large standard deviations for $T_\gamma = 1373\,\mathrm{K}(1100\,^\circ\mathrm{C})$ is due to uneven grain growth between the centre and the edges of the sample, presumably caused by the short austenitisation times used of 10 min (fig. 3.2). The histogram of fig. 3.3 shows that the large standard deviation does not correspond to a bimodal distribution of grains. Large austenite grains permit long martensite plates, which are more prone to cracking [63, 64, 66]. Therefore, the large scatter of coarse grains in the 1373 K (1100 °C) sample should lead to an increased

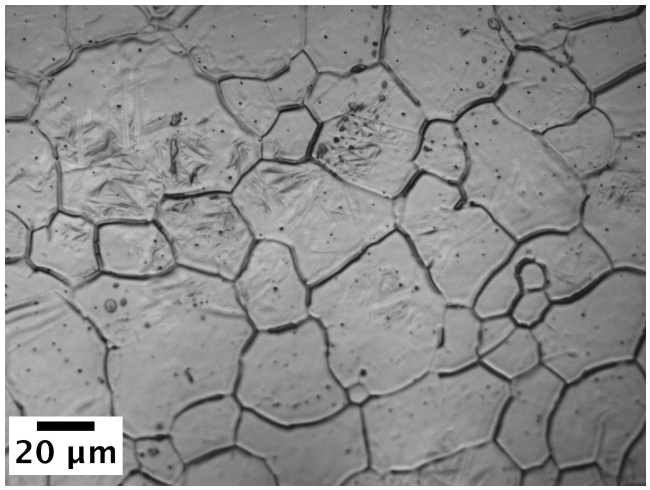

a)

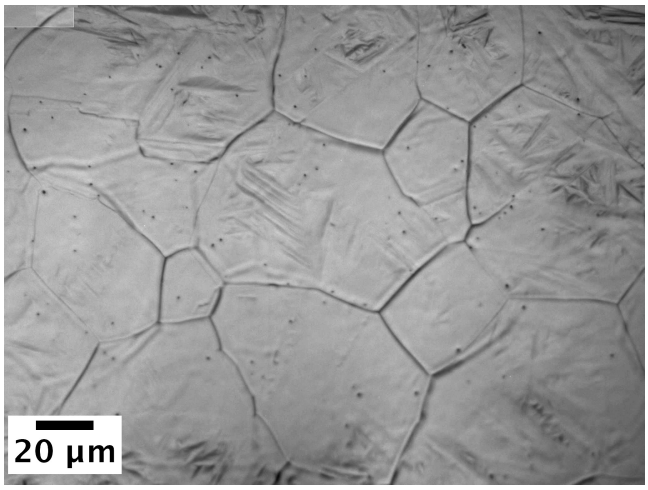

b)

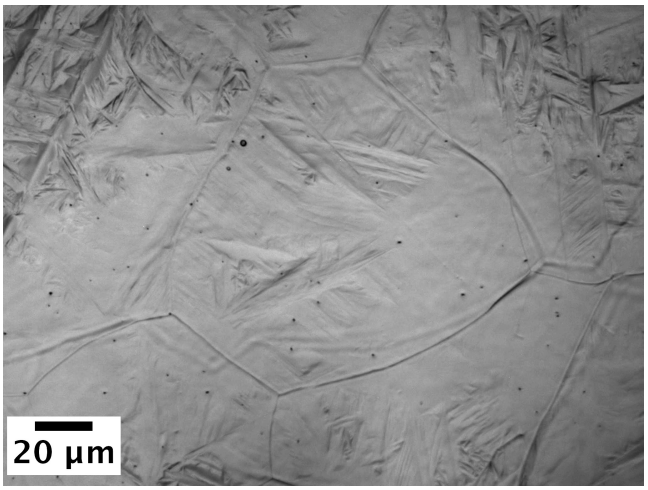

c)

Fig. 3.2 Prior austenite grain boundaries a) just below the surface of a sample austenitised at $T_\gamma = 1373\,\mathrm{K}(1100\,^\circ\mathrm{C})$ for 10 min, b) 2 mm below the surface, and c) at the centre of the sample.

probability of microcracking, a fact that was exploited to design the extensive martensite plate cracking treatment described in section 3.3.3.

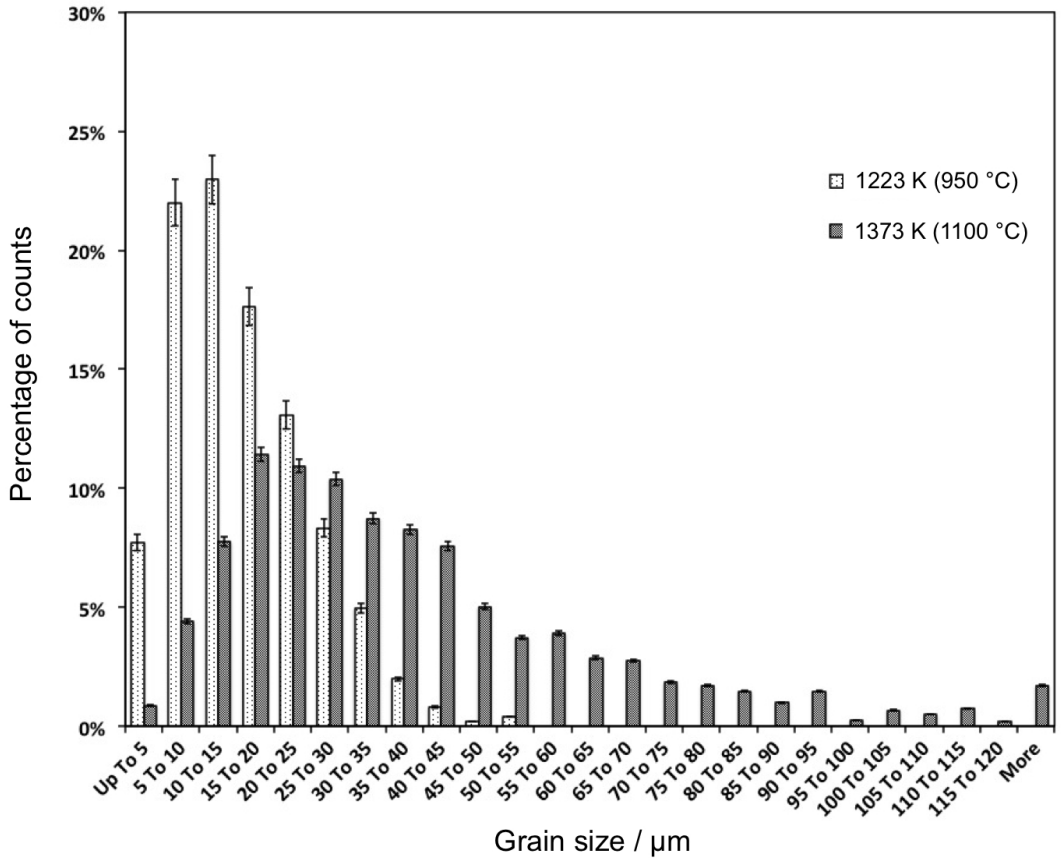

Fig. 3.3 Histogram of prior austenite grain size distribution.

3.3.2 Production of infrequent fine-cracks

The length of martensite plates can be controlled via the austenite grain size. The severity of the quench, which influences the homogeneity of thermal stresses, can in turn be adjusted by using different cooling media, their temperatures, and levels of agitation. However, the influence of different levels of agitation was not investigated in this study. The initial experiments were performed with a set austenitisation time of $t_\gamma = 10\,\text{min}$ and water as the quenchant. Since the first samples austenitised at $T_\gamma = 1373\,\text{K}(1100\,^\circ\text{C})$ displayed extensive grain boundary cracking (fig. 3.4), lower T_γ values and quenching into hotter water was pursued. The minimum T_γ used was 1113 K (840 °C), as this is the standard for 52100 steel bearings, and a treatment that leaves the most crack-free microstructure. For the sake of

brevity, in subsequent discussion we use the notation 0000-00Q where the first four digits represent T_γ in Celsius, followed by the temperature of the quenching medium, which is identified by the letters W or O to represent water and oil respectively. The austenitisation time for these infrequent fine-crack treatments was always 10 min.

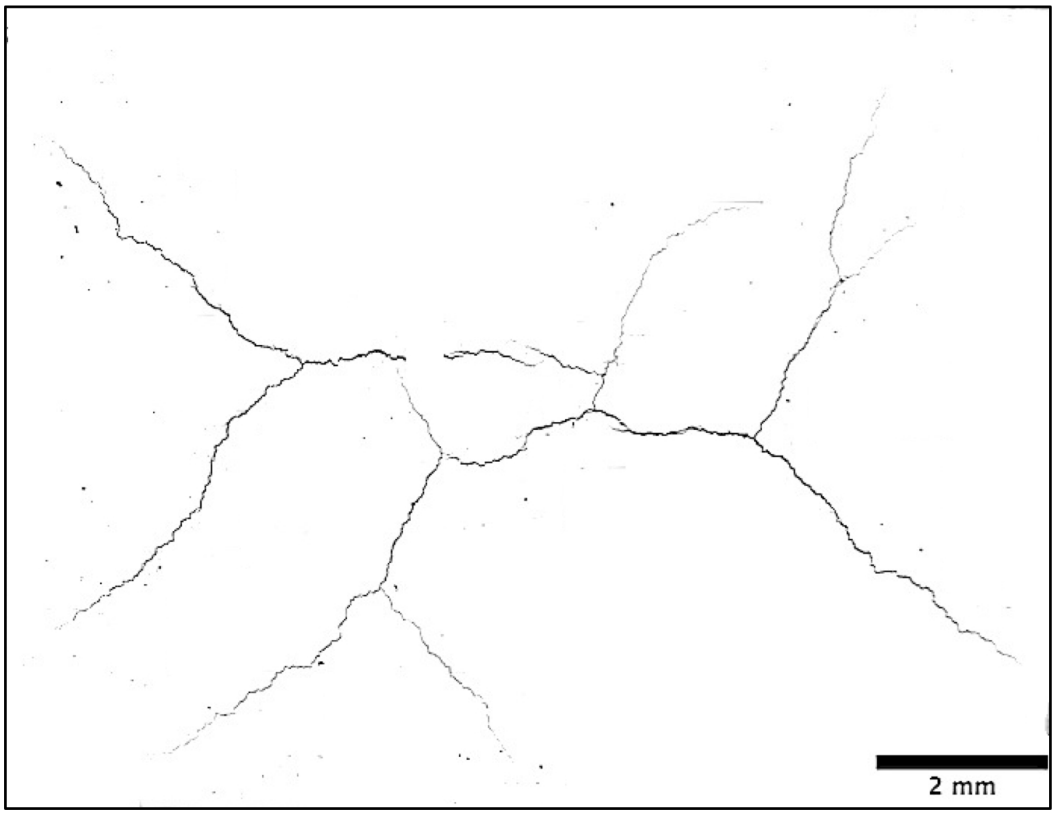

Fig. 3.4 Ensemble of optical micrographs revealing a coarse grain boundary crack. The outline of the figure corresponds to the edges of the sample.

The least severe water-based heat-treatment, 840-92W, still led to profound grain boundary cracks, so the quenchant was changed to oil, for which the same procedure was followed except that the oil was kept at room temperature for safety reasons. Only by using T_γ= 1173 K (900 °C) and quenching in oil at 295 K (22 °C) (900-22O), could the networks of coarse grain-boundary cracks be suppressed, although finer boundary cracks persisted, as illustrated in fig. 3.5a. Lower T_γ values were tested until only martensite-plate cracks were obtained for T_γ=1153 K (880 °C) (fig. 3.5b). However, cracks could not be detected once $T_\gamma < 1133$ K(860 °C). Martensite plate cracks were scarce due to the short austenitisation times used in this experiment that did not allow the austenite grains to coarsen much (see previous section). Martensite plate cracks can normally be distinguished from grain boundary fracture because they typically are only $\sim 5\,\mu$m long with serrated contours. Neverthe-

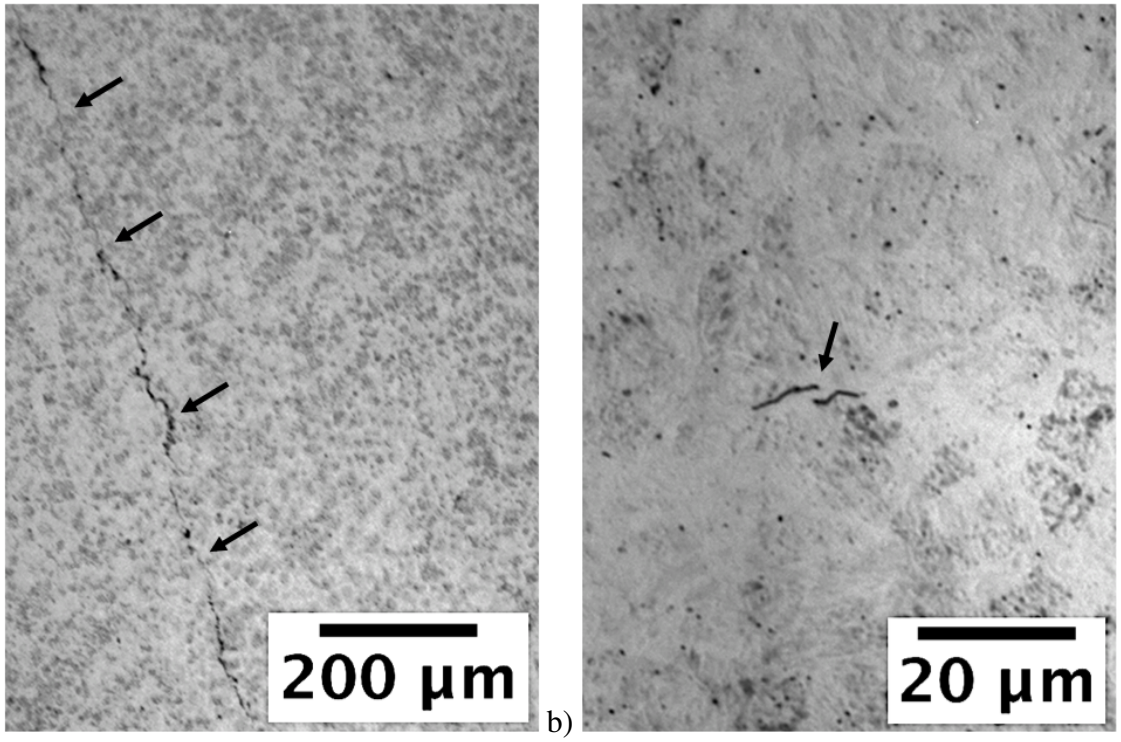

Fig. 3.5 a) A fine grain boundary crack in sample 900-22O and b) martensite plate cracks in sample 880-22O.

less, confusion can arise from crack-like features like thin manganese sulphide inclusions or unevenly etched regions, avoided by observing unetched samples.

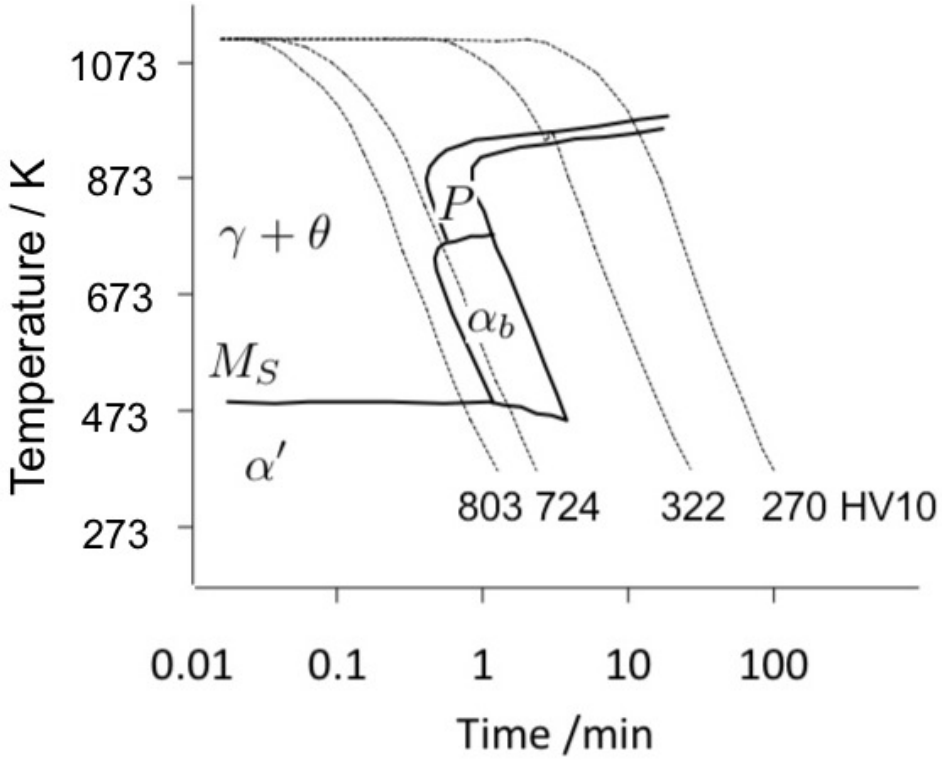

Fig. 3.6 Continuous cooling transformation (CCT) diagram for 100Cr6 alloy: Fe-0.95 C-0.36 Mn-0.28 Si-1.84 Cr wt% showing: pearlite (P), bainite (α_b), martensite (α'), the martensite start temperature (M_s), and the austenite + cementite phase field ($\gamma + \theta$). The dotted lines represent examples of cooling curves that depending on the regions intersected yield different phases or microstructures as reflected by the vickers hardnesses presented, performed with a 10 kg load when the samples reached room temperature [4] adapted from [154].

3.3.3 Extensive martensite plate cracking treatment

T_γ = 1373 K (1100 °C) creates large austenite grains and hence, long and crack-prone martensite plates. Nonetheless, the large thermal stresses associated with the quenching from such high temperatures, even in oil, induce macroscopic grain boundary cracks. According to the continuous cooling transformation diagram of an alloy similar to 52100 steel (fig. 3.6), quenching can take about 60 s over the range of 1113 K (840 °C) to 473 K (200 °C) without the risk of forming pearlite (P) or bainite (α_b). Therefore, in order to maximise martensite plate cracking whilst avoiding boundary fracture due to thermal shock, samples were

austenitised at the lowest temperature of the γ phase field for long times, but cooled in still air for close to 50 s, which reduced the temperature to around 923 K (650 °C), and finally quenched in oil at room temperature for 5 min before rinsing in water.

This treatment was first tested on a small thin sample 40 mm long, 8 mm wide, and 2 mm thick austenitised at 1313 K (1040 °C) for 30 min, cooled in air for 45 s, and quenched in oil at room temperature. The hardness achieved was 810 HV30 and many martensite plate cracks were obtained. However, to replicate this treatment for a rod sample (10 mm in diameter and 120 mm in length), the austenitisation time was tripled to 90 min followed by cooling in air for $\sim$ 55 s, and quenching in oil at room temperature, which created many martensite plate cracks in a sample with a hardness of 751 HV30 (fig. 3.7).

In order to replicate the martensite plate cracking treatment for a different alloy, the austenitisation temperature should be set so that undissolved cementite does not limit the growth of austenite grains and to dissolve sufficient carbon in the austenite to render the martensite plates brittle and prone to fracture. Based on the results obtained in this study, the austenitisation time should be adapted depending on the thickness of the sample so that the prior austenite grains are larger than $\sim 40\,\mu$m. The chemical composition of the alloy is also important in defining the maximum time available for quenching to the martensite-start temperature; the quenching medium should minimise the quench stresses to avoid large quench-cracks. As mentioned previously, factors such as the type of quenchant, its temperature, level of agitation, volume, or even multiple quenching media need to be considered.

3.3.4 Inducing surface cracks

It is sometimes necessary to introduce microscopic surface-breaking cracks, for example, to study how the transmission of contact pressure to the crack front via the pulsating lubricant influences damage evolution [155]. Such cracks have in the past been achieved by indenting the bearing raceway so that the resulting stress concentration during rolling contact initiates the crack, but local surface upheavals cause particular distributions of stress during repeated rolling contact [156]. A new method was designed that avoids the upheavals, whereby an indentation is used to immediately induce some surface-breaking cracks, followed by grinding to smooth the surface while retaining the cracks.

Initial attempts involved indentation with 90 kN silica sand with a particle size of about 300 µm and a hardness of about 900 HV30 into as-received (193 HV30) and heat-treated samples (514 HV30). The indents, illustrated in fig. 3.8a, did not induce the desired cracks,

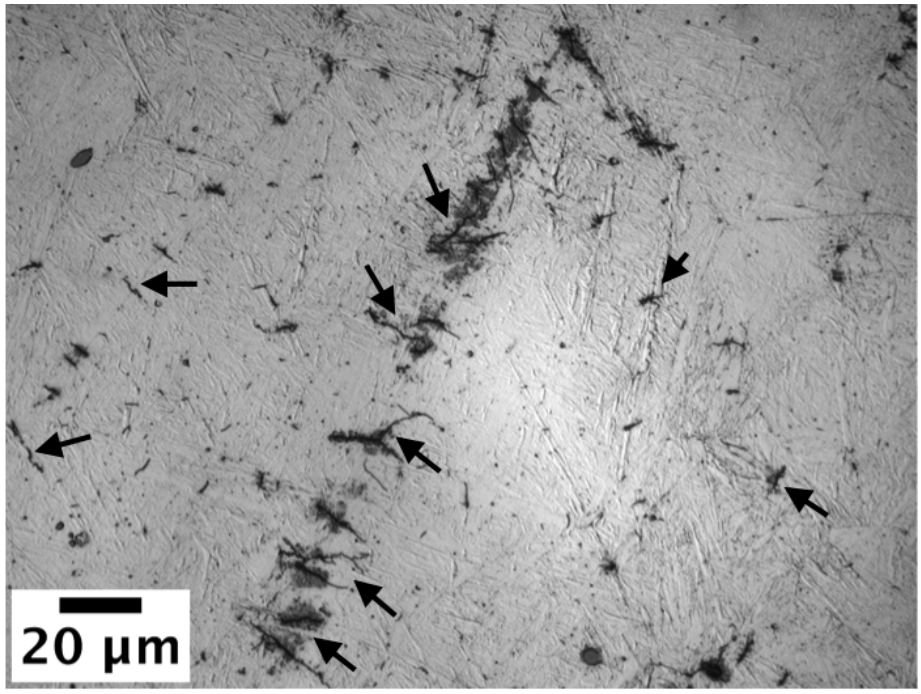

a)

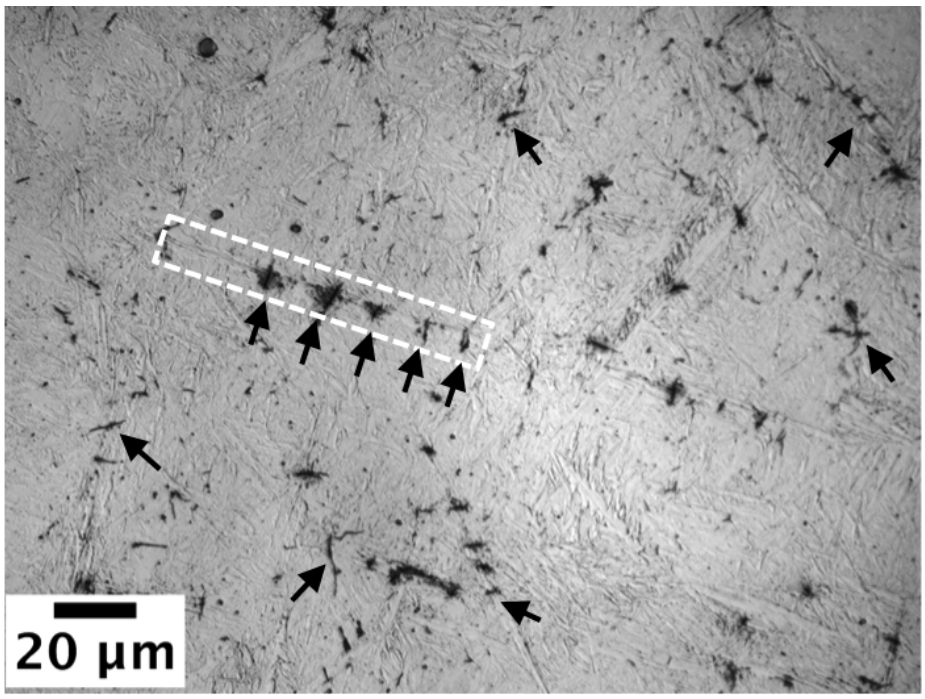

b)

Fig. 3.7 Final extensive martensite plate cracking heat-treatment depicting a) large cracks in the centre of the sample and b) smaller cracks close to the free surface. Martensite plate cracks form as families of parallel cracks that cut across the plates, as shown in b) where the black arrows indicate the cracks and the white box, a martensite plate.

presumably because of the relatively low hardness of the samples. Therefore, bending fatigue tests were carried out in an attempt to open up cracks at the indent tips on thin samples ($40 \times 8 \times 2$ mm), as illustrated in fig.3.8b, using a fixed displacement of 0.7 mm, at 5 Hz. Since these tests did not succeed in producing the desired cracks after a reasonable number of cycles (3×10^3), a different approach was adopted as described below.

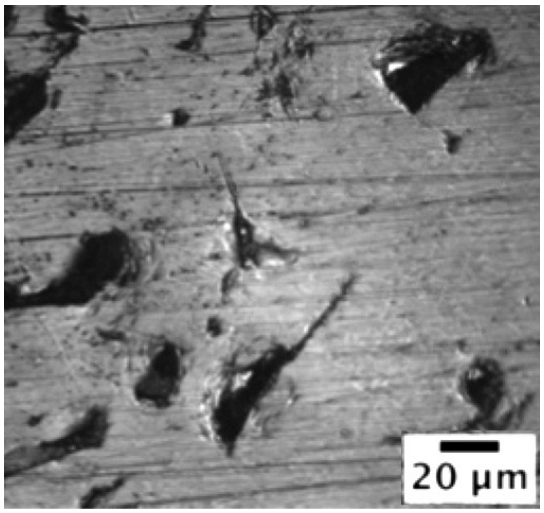

a) b)

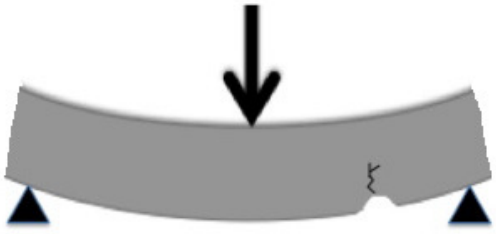

Fig. 3.8 a) Indents created upon compression of silica sand against heat treated sample and b) schematic of bending fatigue testing to generate cracks at indentations.

Based on previous indentation cracking studies of embrittled steel [157], subsequent testing was performed using harder samples and Vickers indents with a load of 130 kg. Harder, more brittle samples, were sought by applying heat treatments that would completely dissolve the cementite, form martensite, but would not form any sort of quench crack. Since austenitising at 1313 K (1040 °C) for 20 min has been reported to dissolve all the cementite [49], a rod sample was austenitised at T_γ = 1313 K (1040 °C) for 30 min, cooled in air for 50 s, and quenched in oil at room temperature, which created a martensitic grain boundary crack-free microstructure.

This treatment is similar to the one described above for extensive martensite plate cracking, but the shorter duration $t_\gamma = 30$ min using a rod sample leads to a smaller $\overline{L}_\gamma$ and hence, a reduced tendency for microcracking. With a hardness of 764 HV30, the sample cracked upon hardness indentation even with a 30 kg load. Unlike the 130 kg load cracks, these 30 kg load cracks were fine so a procedure to extend them was developed. Just as incompressible lubricants fill surface cracks in bearings and propagate them by cyclically transmitting load to their tips, samples with fine surface cracks were introduced in a Stansted fluid power FPG

2340 isostatic press, for tens of 60 s cycles at a pressure of 170 MPa whilst being submerged in a mixture of 10% Shell Dromus B oil and water. In order to ensure oil penetration into cracks prior to this cyclic pressurisation, the samples were placed in a GallenKamp 1 kPa vacuum oven for 1.5 h at 313 K (40 °C), after which they were immediately submerged in the oil. As a result of the pressure cycles, the cracks became larger: 2.5±0.2 µm wide compared to original width of 1.3±0.09 µm (fig. 3.9).

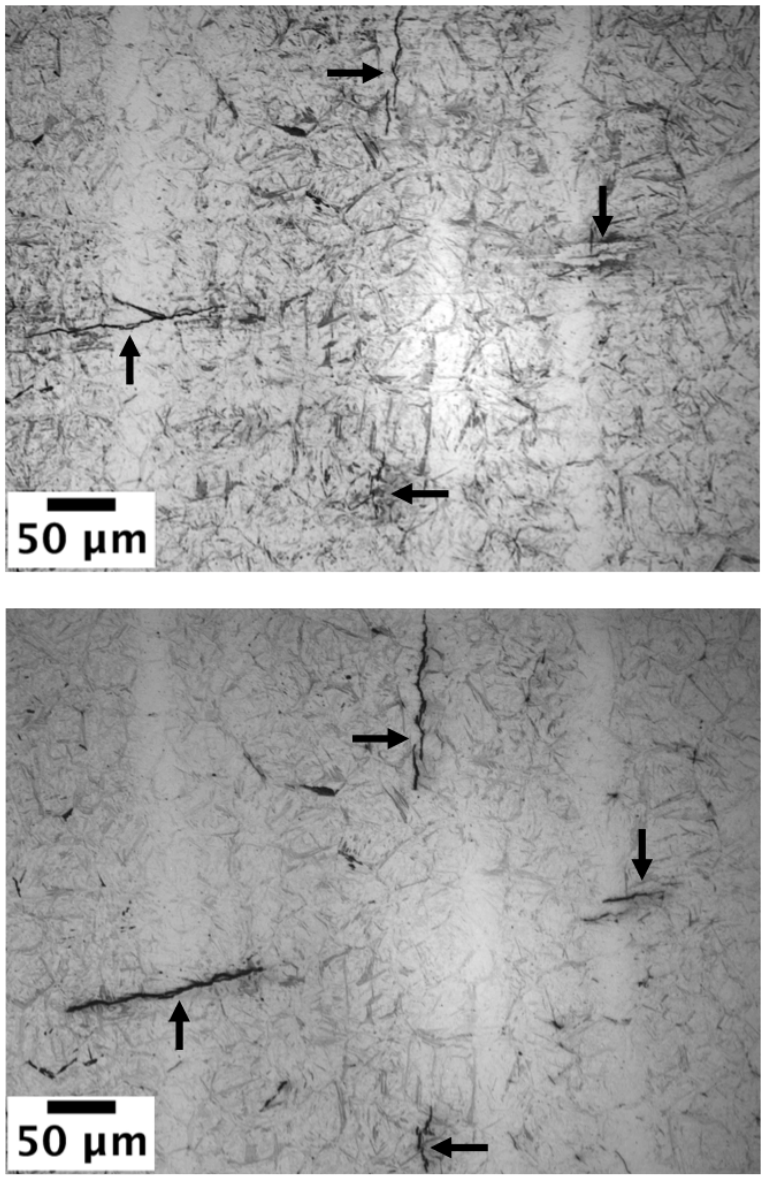

Fig. 3.9 Indentation-induced cracks using a 30 kg load a) after the indent was barely ground away, and b) after the isostatic pressure crack propagating treatment.

Another method used to amplify cracks was to submerge the previous sample in liquid nitrogen before further indentation. The cryogenic treatment stimulated the formation of additional martensite, resulting in an increase in hardness by 46 HV30 to 810 HV30. In order to study the influence of hardness on cracking, the depth of 30 and 130 kg indents with and without cryogenic treatment was calculated based on the geometry and size of the Vickers diamond indenter. The results are presented in table 3.3.

Table 3.3 Summary of indentation depths using different loads.

Vickers hardness indentation		
Load / kg	Cryogenic treatment	Calculated indent depth /μm
30	yes	51
	no	53
130	yes	107
	no	111

As expected, the increased hardness of the cryogenically treated samples gave rise to smaller, shallower indents and more extensive cracking (fig. 3.10). Although cracks created with both 30 and 130 kg loads remained after the indents were skimmed off by grinding, only the cracks created with a 130 kg load remained after the depth of grinding reached 250 μm as measured with a micrometer, irrespective of liquid-nitrogen treatment (fig. 3.10b and d). It is considered that in experiments involving real bearings, a depth of 250 μm would need to be removed from the surface after the final heat treatment in order to eliminate any decarburised layers, so surface cracks induced using the 130 kg load would be appropriate.

Once cracks were proven to remain in the sample after deep grinding, this treatment was applied to a rod sample (120 mm long and 10 mm in diameter) austenitised at 1313 K (1040 °C) for 30 min, cooled in air for approximately 55 s to 906 K (633 °C), and quenched in oil at room temperature. The dimensions of the rod are such so it can be loaded in a Delta Research Corporation rod-ball rolling contact fatigue test rig. After heat treatment, the rod was indented ten times along its circumference. Optical microscopy images of this indent ring revealed an interesting range of crack morphologies, orientations, and sizes, different to what was observed in the flat samples, fig. 3.11.

At the bottom of every indent, a grain boundary crack normal to the surface reached a depth of approximately 100 μm. Instead, at a depth of 200 to 250 μm, long grain boundary

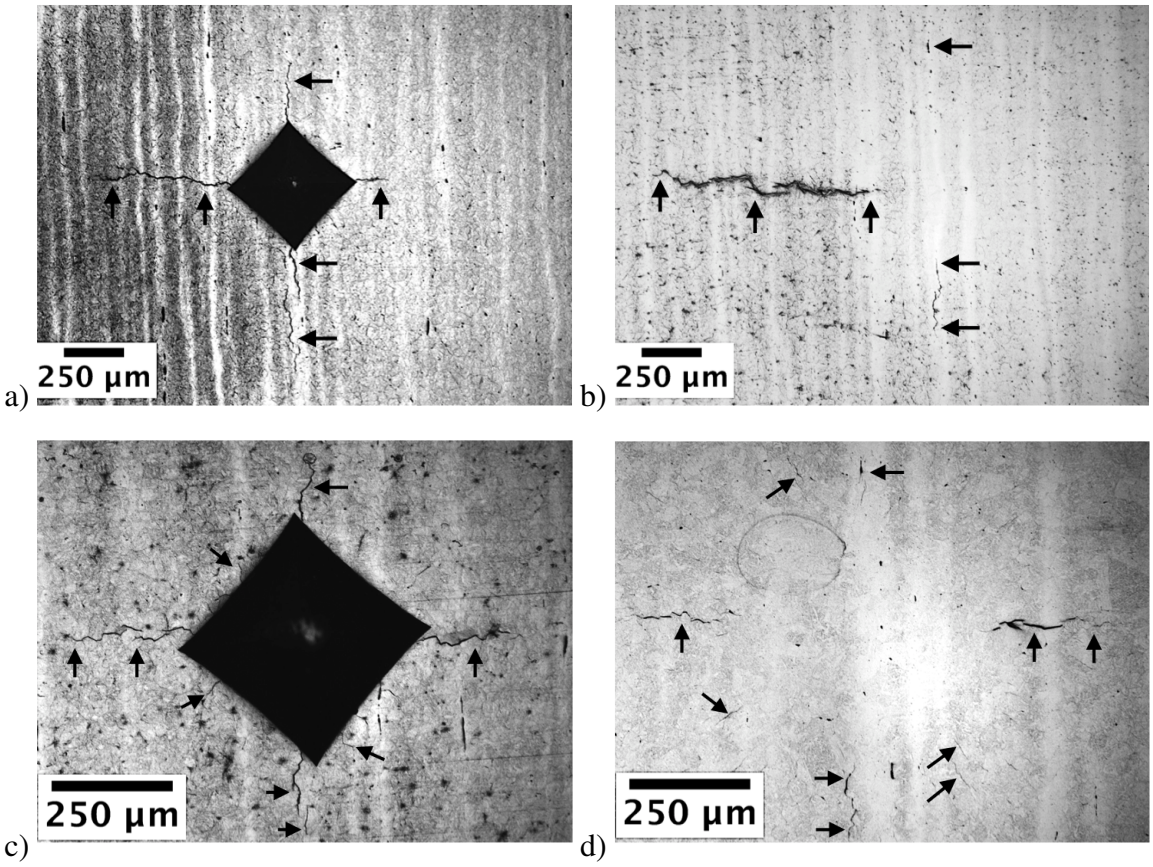

Fig. 3.10 Hardness indentation using a 130 kg load showing a) indent-induced cracks on sample without liquid-nitrogen treatment, b) cracks remaining after 250 µm grinding, c) indent cracks on sample after liquid-nitrogen submersion, d) remaining cracks after 250 µm grinding.

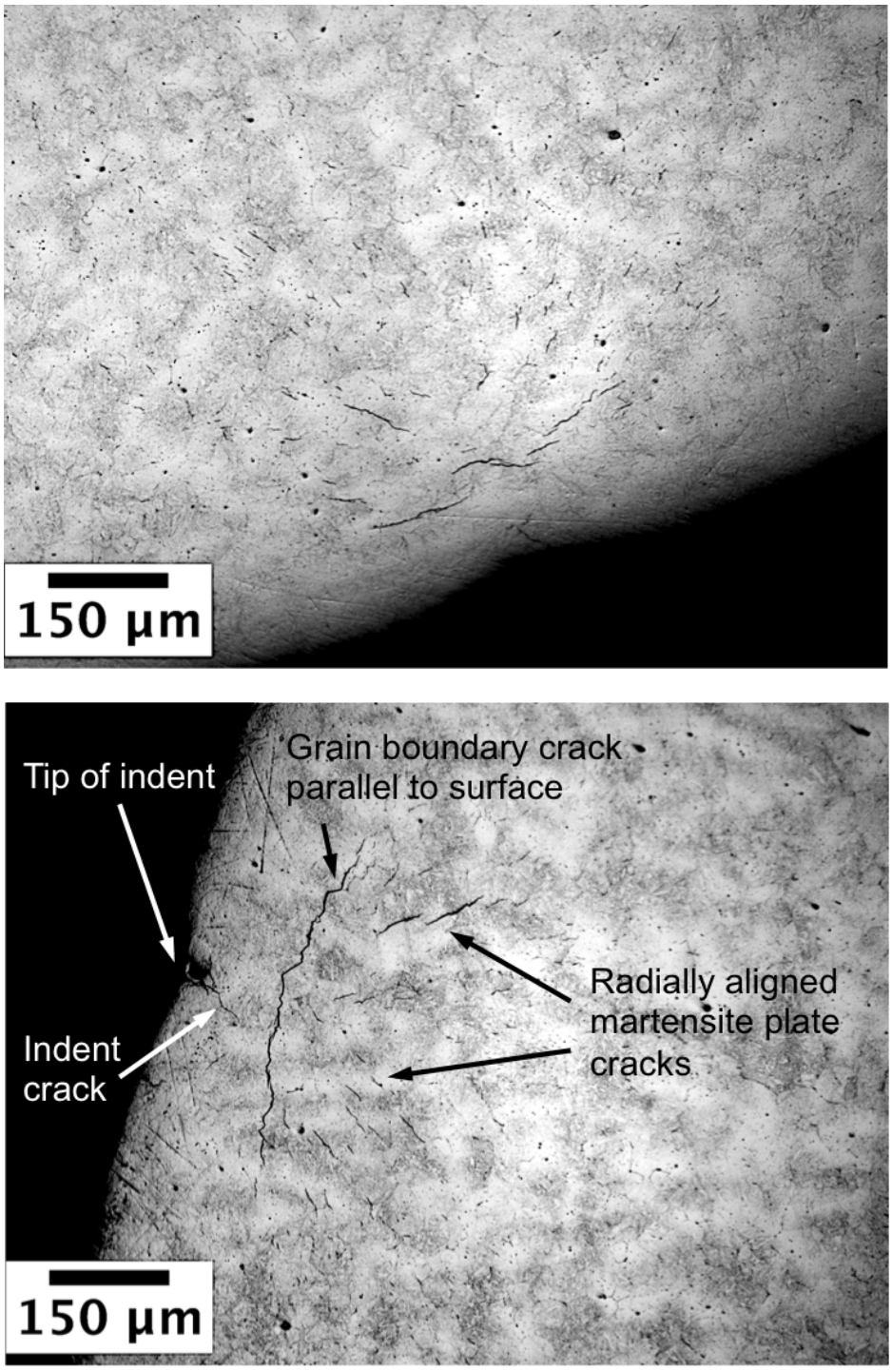

Fig. 3.11 Radial cross section of rod sample showing two different indents and the different types and orientations of cracks produced.

cracks parallel to the sample surface and most likely growing along the axis of the rod were observed. Finally, from a depth of 300 to 1000 µm, a family of martensite plate cracks all more or less radially aligned with the indent tip were apparent. Although no explanation for this phenomenon has been found, it is speculated that the cracks are due to the interaction of residual tensile stress at the surface of a quenched sample possibly caused by grinding or decarburisation [4] (fig. 3.12), the compressive residual stress caused by indentation, and the volume expansion of indentation-stress induced martensite in the untempered specimens. In any case, it is expected that after the final grinding procedure that erases the indents and most of the grain boundary cracks parallel to the surface, martensite plate cracks will remain for further studies.

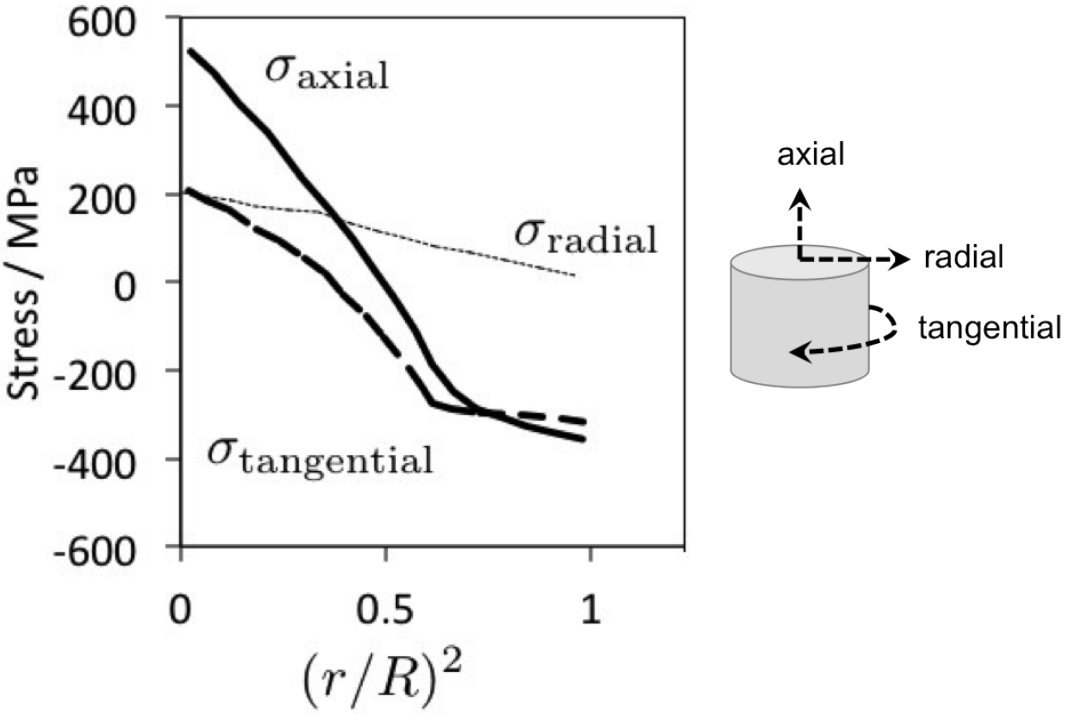

Fig. 3.12 Residual stress on quenching a steel cylinder in water at 273 K (0°C) from 873 K (600°C), where r is the position along the radial direction starting from the centre and R is the radius of the rod so that $(r/R)^2 = 1$ represents the surface. Adapted from [158].

The flow chart of fig. 3.13 summarises the pathways to different crack morphologies. In addition, fig. 3.14 schematically depicts the heat treatments necessary for such cracks to be created.

3.4 Conclusions

- The optimum treatment to produce a sparse dispersion of martensite plate microcracks in a 10 mm diameter sample requires austenitisation at 1153 K (880 °C) for 10 min followed by quenching in oil at room temperature. Alternatively, if fine grain boundary cracks are desired for the same sample size, austenitisation at 1173 K (900 °C) for 10 min and quenching in oil at room temperature is the heat treatment required.
- The best treatment to create many martensite plate cracks in a rod 10 mm in diameter requires austenitisation at 1313 K (1040 °C) for 90 min, followed by cooling in air for approximately 50 s, and quenching in oil at room temperature.
- Surface cracks can be introduced reliably by indenting with a Vickers diamond and a 130 kg load for samples harder than $\sim$ 750 HV30.
- Indentation cracks can be widened via isostatic pressure or propagated through bending if the sample geometry permits.
- The generation of additional martensite by cryogenic treatment in liquid nitrogen increases the frequency (though not the depth) of surface cracks during indentation. The Vickers diamond indentation load required is 130 kg because this permits the subsequent removal of the surface to a depth of 250 µm without grinding away the cracks.
- The most successful surface cracking treatment for a 10 mm in diameter sample, consists of austenitising at 1313 K (1040 °C) for 30 min, cooling in air for approximately 50 s and quenching in oil at room temperature. The sample should be then indented with a Vickers hardness tip and a 130 kg load. Finally, 120 µm of the surface material have to be ground away to eliminate completely the indent whilst the surface and subsurface cracks created upon indentation remain. For the study of real bearings, grinding away 250 µm is recommended.

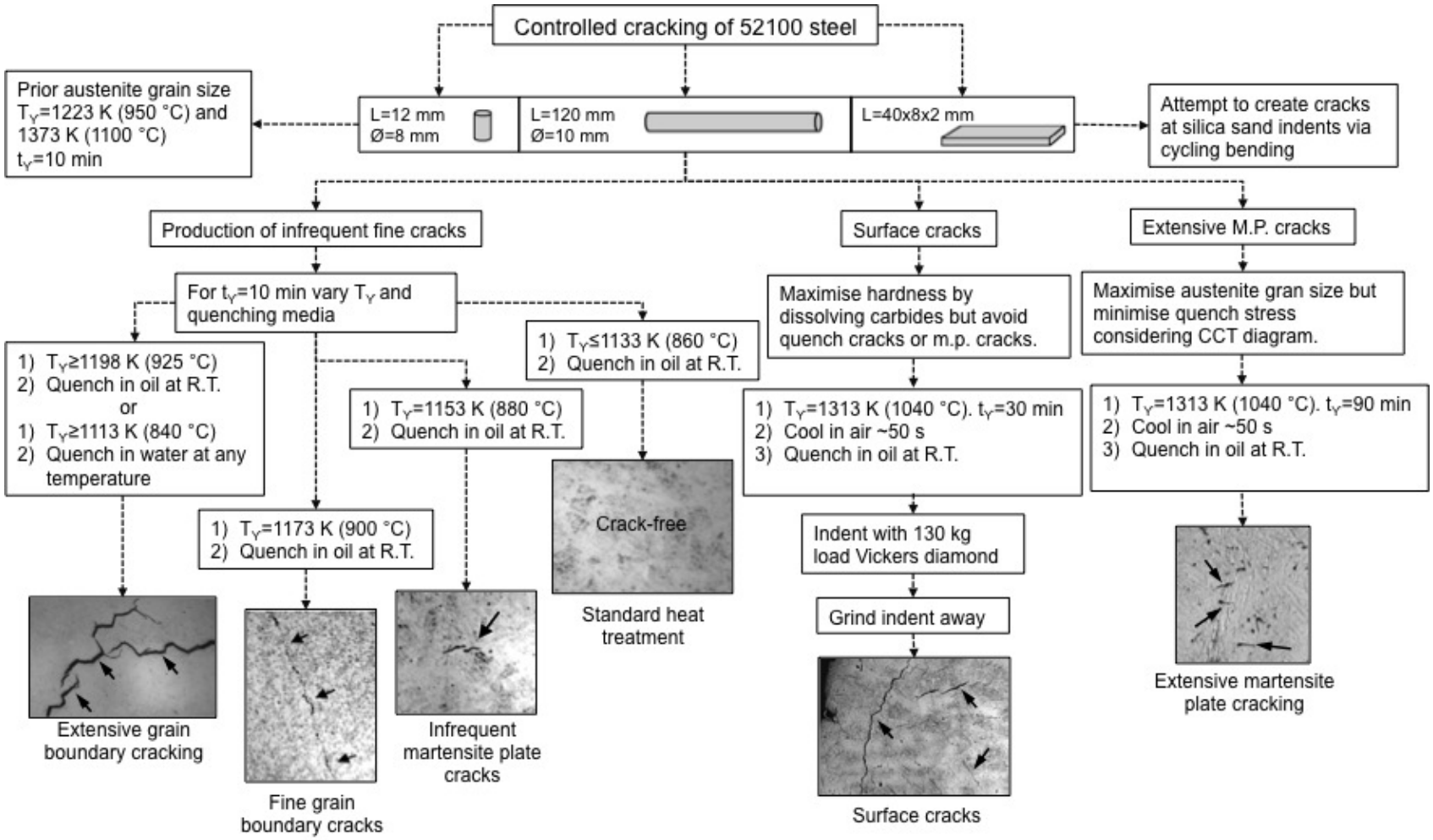

Fig. 3.13 Flow chart of experimental work, where m.p. stands for martensite plate cracks, R.T. for room temperature, and CCT for continuous cooling transformation.

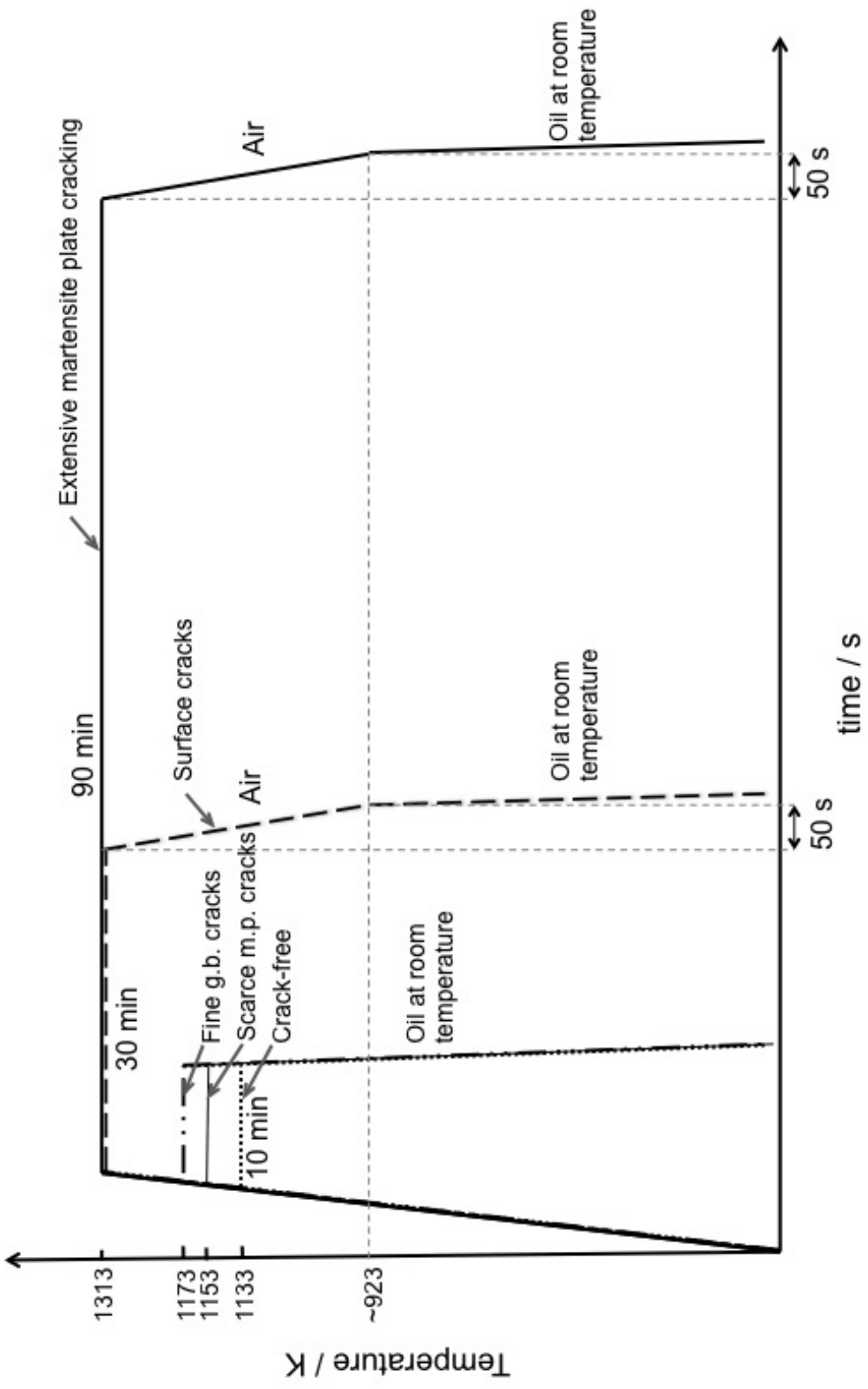

Fig. 3.14 Schematic of final heat treatments for a 10 mm in diameter and 120 mm long rod, where m.p. stands for martensite plate and g.b. for grain boundary cracks. The surface cracked sample was indented after the depicted heat treatment.

Chapter 4

Distinguishing cause and effect in bearing steel failure

4.1 Introduction

The premature failure of large bearings of the type used in wind turbines, possibly through a mechanism called “white-structure flaking", has triggered many studies of microstructural damage associated with “white-etching areas" created during rolling contact fatigue, although whether they are symptoms or causes of failure is less clear. Therefore, special experiments have been conducted to prove that white-etching areas are the consequence, and not the cause, of damage. By artificially introducing a fine dispersion of microcracks in the steel through heat treatment and then subjecting the sample to rolling contact fatigue, manifestations of hard white-etching matter have been created to a much greater extent than samples similarly tested without initial cracks. A wide variety of characterisation tools has been used to corroborate that the white areas thus created have the same properties as reported observations on real bearings. Evidence suggests that the formation mechanism of the white-etching regions involves the rubbing and beating of the free surfaces of cracks, debonded inclusions, and voids under repeated rolling contact. It follows that the focus in avoiding early failure should be in enhancing the toughness of the bearing steel in order to avoid the initial microscopic feature event.

4.2 Experimental Methods

4.2.1 Microscopic cracking

Using the same hot-rolled and spheroidised 52100 steel (table 3.1), long cylindrical samples 10 mm in diameter and 120 mm long were manufactured using a spark erosion machine and a lathe, followed by heat-treatment in a box furnace. Three different heat treatments were applied to obtain the standard and two different cracked microstructures, as presented in chapter 3. The crack-free control sample was austenitised at 1113 K (840 °C) for 10 min, quenched in oil at room temperature, and tempered at 433 K (160 °C) for 2 h that represents the standard heat treatment for 52100 steel. The sample containing cracked martensite-plates (MPC) was austenitised at 1313 K (1040 °C) for 90 min, cooled in air for 50 s, quenched in oil at room temperature, and finally tempered at 433 K (160 °C) for 2 h. After the heat treatment, these two samples were cylindrically ground to the final diameter of 9.53 mm to get rid of any decarburised layer and to achieve a reasonable surface roughness for rolling-contact fatigue testing.

The surface cracked sample (SC) was asutenitised at 1313 K (1040 °C) for 30 min, cooled in air for 50 s, followed by quenching in GP460 oil at room temperature. It was then indented twelve times along its circumference using a Vickers indenter and a 130 kg load to induce indentation cracks before cylindrically grinding to the final diameter of 9.53 mm. The grinding eliminated the upheavals caused by indentation but not the surface-breaking indent cracks; after grinding, it was finally tempered at 433 K (160 °C) for 2 h. Temperatures were monitored throughout the heat treatment of all samples by spot welding K-type thermocouples to the samples.

4.2.2 Rolling contact fatigue testing

Testing was carried out on a Delta Research Corporation BR-4 Ball-Rod Rolling Contact Fatigue machine [159]. The load is applied by three 12.7 mm in diameter balls, placed inside a bronze retainer, so that the balls push against the rotating test specimen of 9.53 mm in diameter through two tapered bearing cups held at a certain distance of each other by adjusting the length of three springs, as seen on fig. 4.1. Testing was performed at room temperature without transient conditions or hydrogen charging of the specimens that would accelerate, but might also alter the microstructural degradation process.

Before every test, three new 52100 balls with a surface roughness of 0.013 µm, the

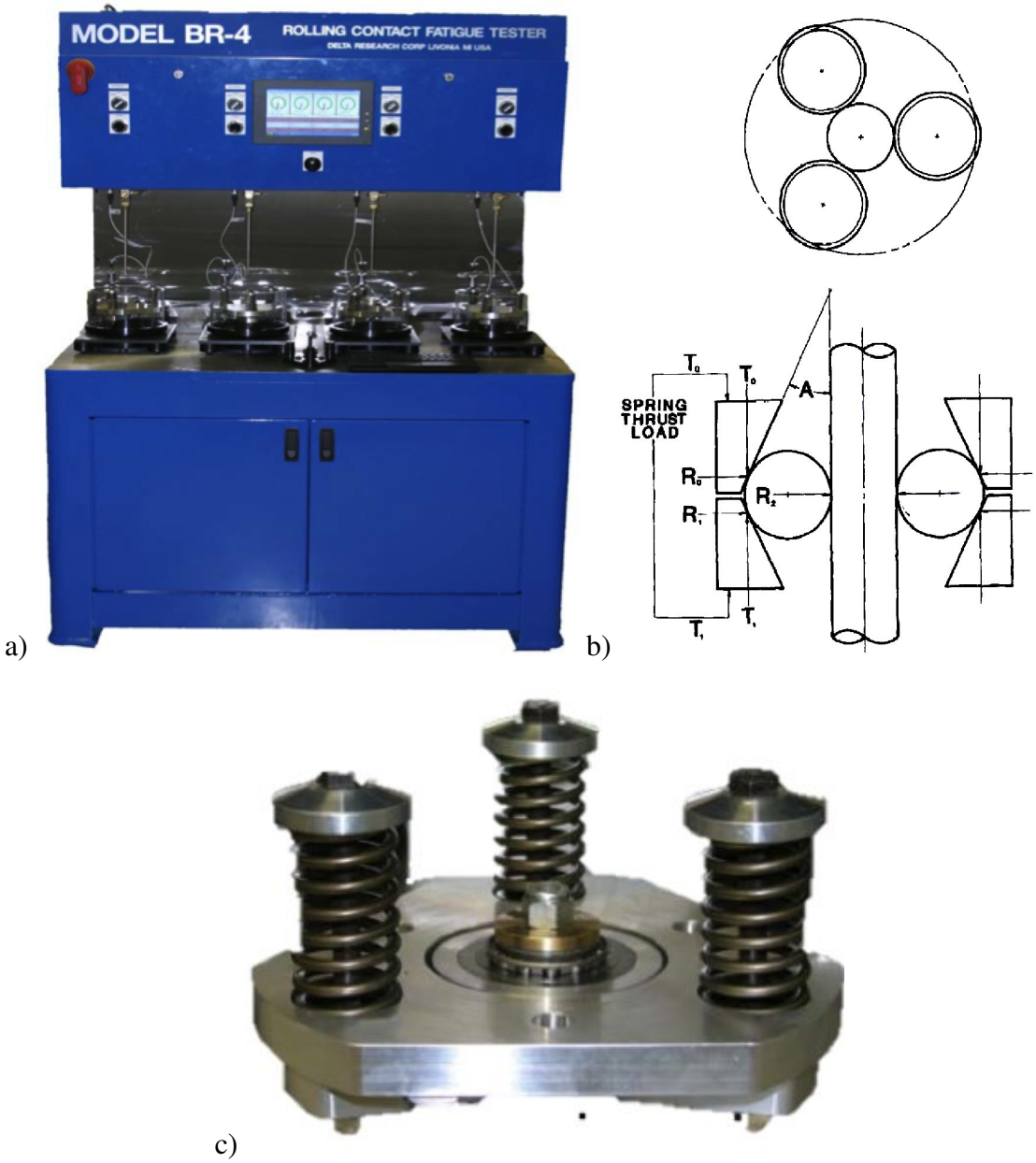

Fig. 4.1 a) BR-4 Ball-Rod Rolling Contact Fatigue machine, b) schematic of the rotating cylinder specimen stressed by three radially-loaded balls, which are thrust loaded by three compression springs [160], and c) individual retainer plate during the load setting configuration showing the three compression springs around three calibration bolts.

bronze retainer, and the rod specimen were ultrasonically cleaned for 5 min first in a mixture of 50% isopropanol-50% water, then in acetone, and finally in isopropanol. The tapered loading cups were changed every four tests and turbine oil BP2380 was used as a lubricant at room temperature and a rate of 10 drops min^{-1}. This oil was filtered and recirculated. Vibration levels were monitored through an accelerometer, which automatically stopped tests if the thresholds were surpassed, caused normally only by flaking or spalling. All tests were performed at a rotational speed of 3600 rpm (the design of the test rig allows $\sim$2.4 stress cycles per revolution as shown in the appendix A) and a Hertzian pressure of 3.5 GPa (191 N of load). The values and depths of the maximum unidirectional and orthogonal shear stresses induced by such Hertzian pressure are presented in table 4.1. However, the actual stresses experienced are likely to be somewhat smaller given groove formation (larger contact area). The nominal thickness of the 3D elastic contact area is 0.635 mm as given by [161]:

$$2a = \frac{\pi p_0 R^*}{E^*} \tag{4.1}$$

$$\frac{1}{R^*} = \sqrt{\frac{1}{R_1^2} + \frac{1}{R_1 R_2}} \tag{4.2}$$

$$\frac{1}{E^*} = \frac{1-\nu_1^2}{E_1} + \frac{1-\nu_2^2}{E_2} \tag{4.3}$$

where p_0 is the maximum contact pressure of 3.5 GPa, R_1, E_1 and ν_1 are the radius, Young's modulus, and Poisson's ratio of the ball and R_2, E_2 and ν_2 of the cylindrical sample. The Young's modulus of both samples was taken as 210 GPa and Poisson's ratio as 0.3.

Table 4.1 Maximum shear stress, τ_{max}, acting at $\pm 45^\circ$ with respect to the surface, and orthogonal shear stress $\tau_{xz,max}$, acting parallel or normal to surface, and their depths, for a 3-D contact area. The values assume frictionless and elastic Hertzian contact p_0=3.5 GPa where $r_0=(3p_0R_{eq}/4E^*)^{1/3}$ and $R_{eq}=(R_1^{-1}+R_2^{-1})^{-1}$ [161].

	τ_{max}		$\tau_{xz,max}$	
	GPa	Depth / μm	GPa	Depth / μm
	$0.31p_0$	$0.48r_0$	$0.25p_0$	$0.25r_0$
Circular contact	1.09	190	0.88	99

4.2.3 Characterisation

Before RCF testing, the average surface roughness, R_a, of the cylindrically ground specimens was measured using a Veeco Dektak 6M Stylus Profiler, which has a tip radius of 12.5 µm.

Optical and scanning electron microscopy (SEM) using a Zeiss optical microscope and a JEOL JSM 5500LV microscope were performed on test specimens prior to heat treatment, after heat treatment, and after RCF. For such characterisation, RCF specimens were cut along the centre of the racetrack in the circumferential cross section and also along the longitudinal section (fig. 4.2).

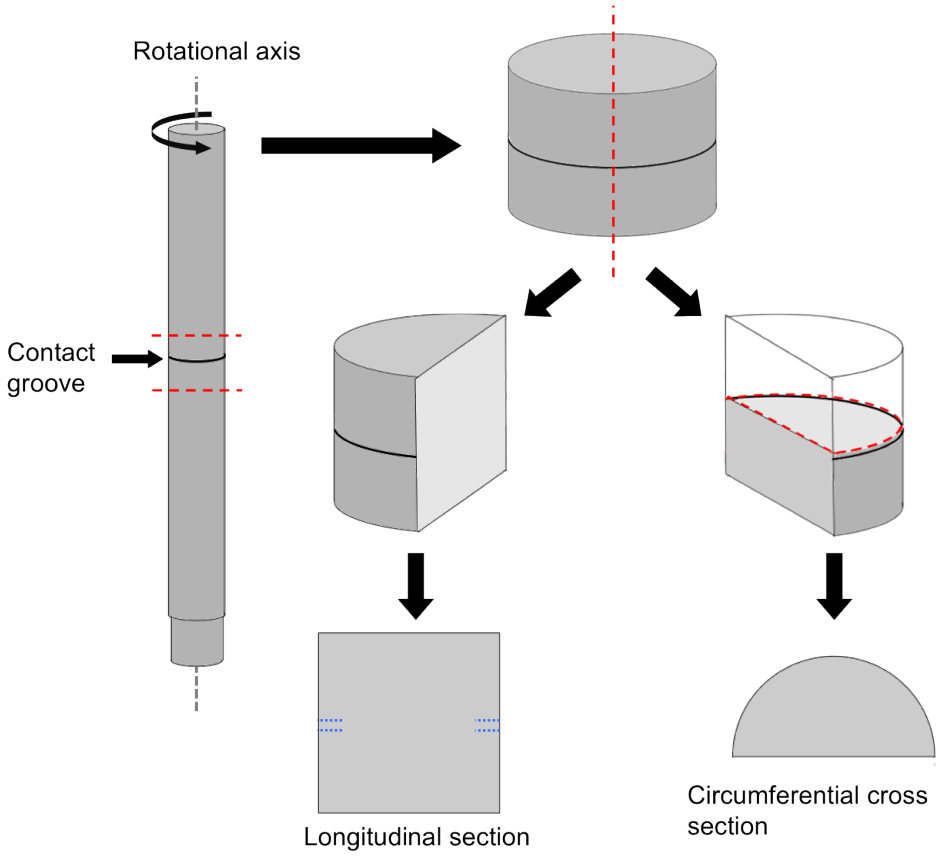

Fig. 4.2 Cutting procedure and sections of RCF test specimens.

The process of microstructural degradation around cracks and inclusions was characterised in more detail by carving out lamellae of white-etching cracks and butterflies from RCF samples, at different cycles, with a FEI Helios dual beam field emission SEM-focused ion beam (FIB) and an ion beam voltage of 30 kV. These lamellae were then observed with a JEOL 200CX transmission electron microscope (TEM) using an accelerating voltage of

200 kV to obtain images and diffraction patters of the matrix, white-etching matter, and inclusions. The chemical compositions of the WEM of butterflies and cracks (WECs), butterfly inclusions, and fatigue crack initiating inclusions were studied using energy dispersive X-ray spectroscopy (EDS) with an Oxford Instruments detector in the JEOL JSM 5500LV SEM using an accelerating voltage of 20 kV and a working distance of 20 mm. The chemical composition of FIB lamellae was studied using an EDAX r-TEM ultra-thin window (UTW) X-ray detector in the FEI Tecnai F20-G2 FEG-STEM with an accelerating voltage of 200 kV.

Although the main objective of this work was to establish whether WEM results from the collision of crack faces during RCF, butterflies were also studied as their WEM wings have been well characterised and would provide a bridge between the WEM created in this study and observations in the published literature.

Macro- and Nano-hardness

Since the crack-free (standard heat treatment) and pre-cracked samples were austenitised at different temperatures and times, their RCF responses were compared by taking into account differences in macrohardness and retained austenite. Macrohardness of the three differently heat-treated samples was evaluated using a Vickers indenter and a 30 kg load. An MTS Nanoindenter XP with a pyramidal Berkovich tip was used to perform nanoindentations on the white-etching matter around cracks and inclusions formed after RCF in order to determine its hardness compared with the matrix. Such measurements were performed at a constant depth of 1 μm. In each case, the mean and standard error of the mean reported correspond to ten indentations.

X-Ray Diffraction (XRD)

The retained austenite content was determined using a Philips PW1830 vertical diffractometer with a CuK_α radiation. Scans were performed from 30 to 125 °, with a step size of 0.05 ° and a dwell time of 26 s. A divergence slit of 0.5 °, an anti-scatter slit of 0.5 °, and a receiving slit of 0.2 mm were used to restrict the beam size and the counts obtained. A rotating stage was necessary for sample MPC in order to obtain sufficient counts due the larger size of its grains. Once the patterns were obtained, HighScore Plus and the Rietveld refinement method were used to fit body-centred tetragonal martensite to two isolated martensite peaks (020 and 121) for each spectrum. This pair of values of tetragonality were then used as minimum and maximum limits in the fitting of lattice parameters for martensite using either

the whole spectrum (30-125 °) or a cropped version (48-110 °), which eliminated martensite and austenite overlapping peaks (e.g. $110_{\alpha'}$ and 111_{γ}). Finally, the three control sample spectra were analysed accounting for cementite, using the whole spectra and the respective martensite tetragonality values.

Electron Backscattered Diffraction (EBSD)

EBSD was performed on colloidal silica polished samples using a Camscan MX2600 FEG-SEM operating at 20 kV and an Oxford Instruments HKL Nordlys camera with Channel 5 software in order to investigate if cracks nucleated at inclusions during RCF propagate along prior austenite grain boundaries. Areas of 400 by 250 μm were mapped using a step size of 0.25 μm. A minimum of seven Kikuchi bands were detected at each indexed point. Post-acquisition analysis of the patterns included removal of wrongly indexed points (wild spikes) and extrapolation of solution to non-indexed points first using non-iterative eight neighbouring points, then iterations with seven, and finally six neighbouring points.

This study was conducted to confirm the lack of toughness of 52100 steel that is the alleged cause of WEM formation through the processes of crack formation and rubbing of the cracked faces under repeated contact stresses. Toughness is here used to indicate the ability of the alloy to resist crack formation at impurities or defects during cyclic deformation, leading to propagation along prior austenite grain boundaries and ultimately, macroscopic failure. It is important to note that the cracks studied through EBSD were almost certainly not caused by the cracking heat treatments, but by RCF as will be explained later.

4.3 Results

The as-received microstructure of the steel, consisting of ferrite and spheroidised cementite particles, is illustrated in fig. 4.3. Once machined, the cylindrical test specimens were heat treated according to the standard (fig. 4.4), surface crack (fig. 3.11), and martensite plate crack procedures (fig. 3.7). The Vickers hardness values of all these samples are presented in table 4.2.

Surface roughness measurements performed along the length of the rods showed that the surface over which the balls rotate (tangential direction) is significantly smoother than the surface along the axial direction given the nature of the final grinding process, as shown in fig. 4.5.

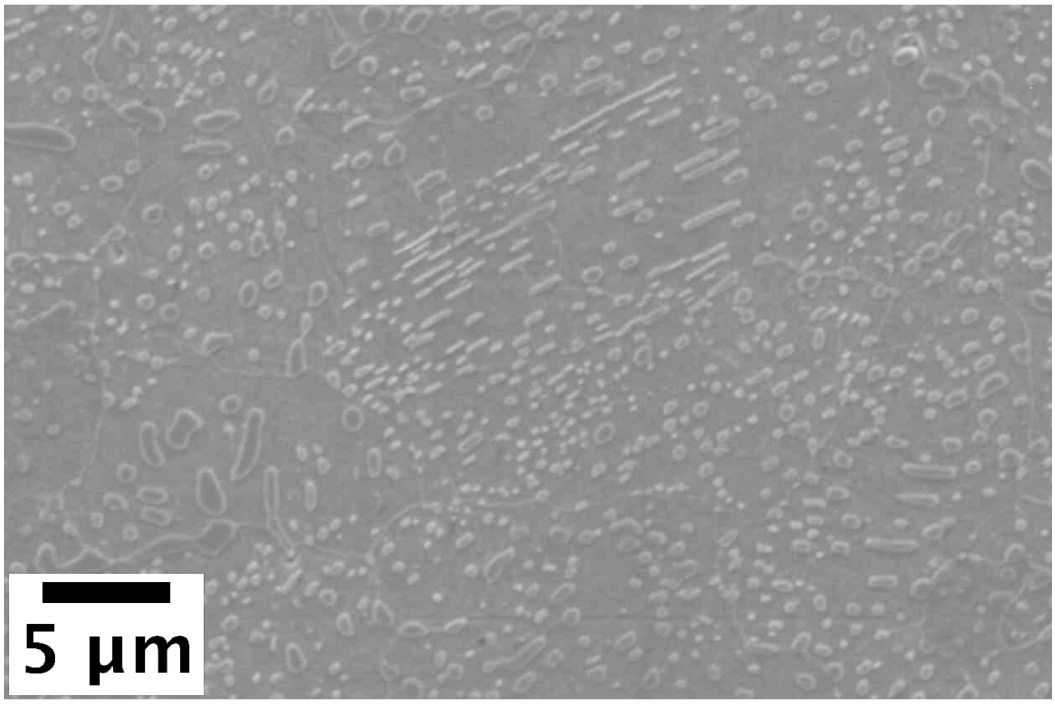

Fig. 4.3 SEM image of initial spheroidised microstructure of the 52100 steel used.

Table 4.2 Hardness values of the as-received material, crack-free, surface cracked, and martensite plate cracked samples.

Sample	HV30
As-received	193±2
Control (standard heat-treatment)	794±5
Surface cracked (SC)	742±9
Martensite-plate cracked (MPC)	770±8

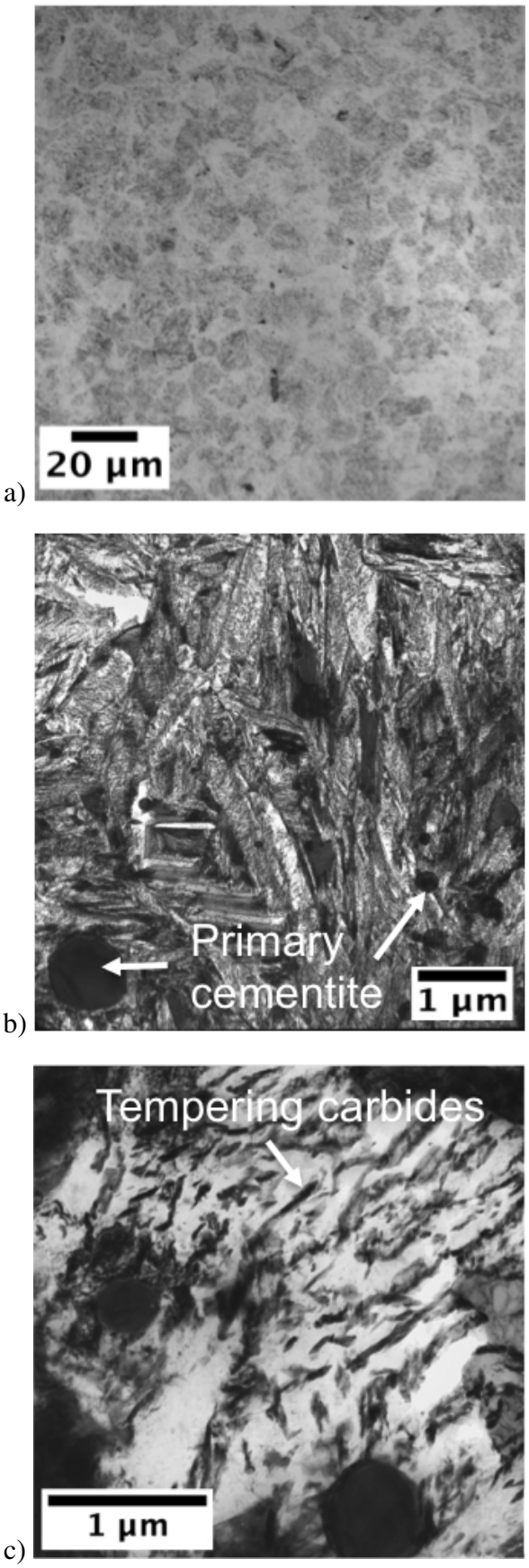

Fig. 4.4 Micrographs of the crack-free sample, resulting in a mixture of tempered martensite containing carbides, and primary cementite taken with a) optical microscope and b) and c) TEM.

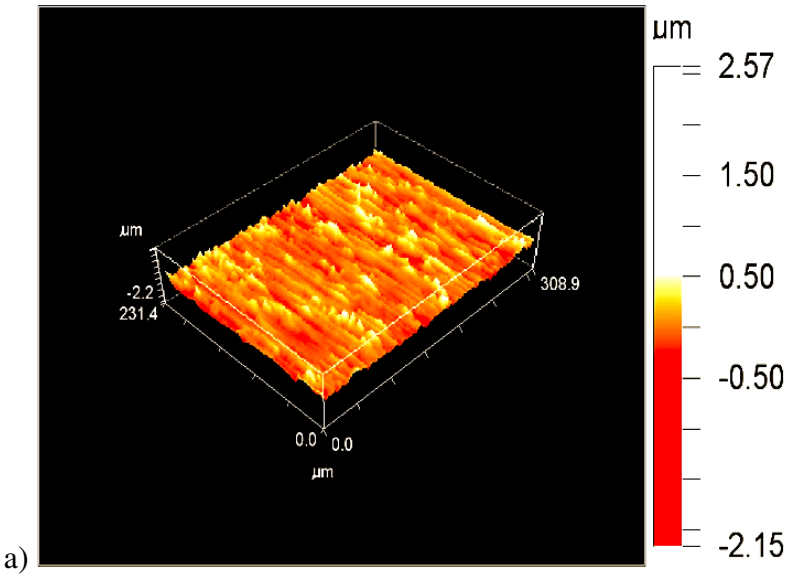

a)

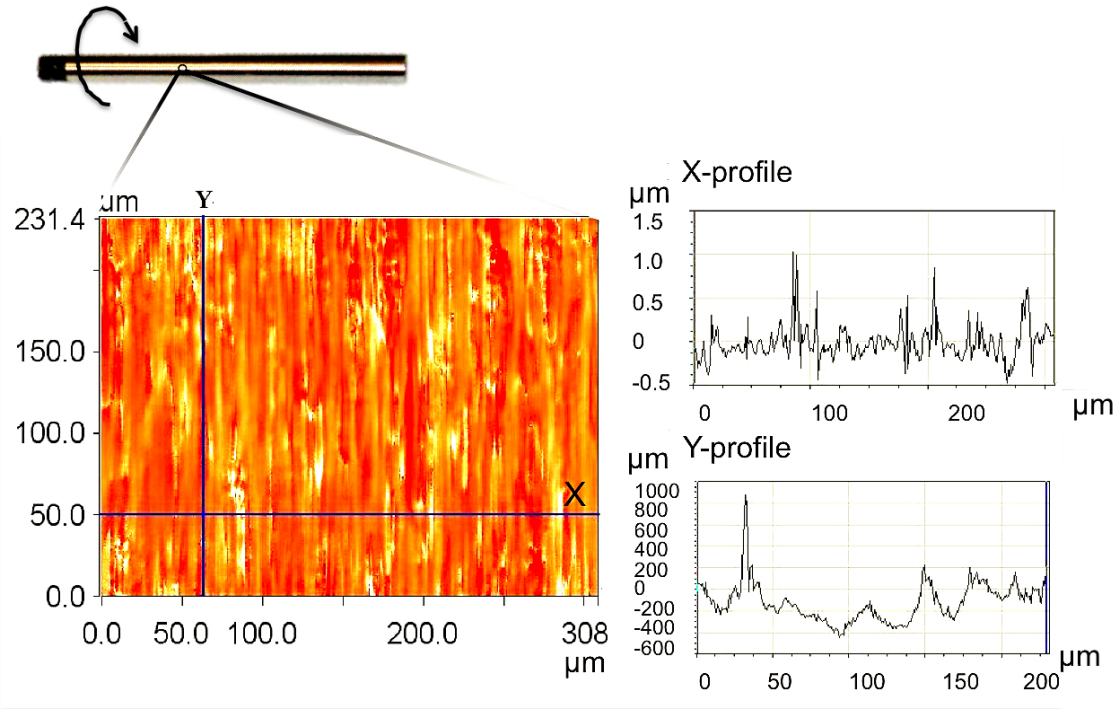

b)

Fig. 4.5 a) 3D surface morphology with an R_a value of 0.147 µm and b) 2D surface morphology of two intersecting lines, where X is parallel to the rotation axis and Y is the line along which balls rotate.

X-ray diffraction measurements of the three different heat treatments applied were performed to take into account the difference of retained austenite volumes when analysing the WEM generated during RCF. The volume fractions of retained austenite were obtained via Rietveld refinement on samples quenched (Q) from the three different austenitisation temperatures and times, quenched and tempered (Q-T) using the standard tempering temperature 433 K (160 °C) and time (2 h), and quenched, tempered, and RCF tested (Q-T-RCF). All values quoted have an uncertainty of ± 0.01, which corresponds to the generally achieved accuracy of the Rietveld refinement method using HighScore Plus. The results are summarised in table 4.3.

Table 4.3 Volume fraction austenite (V_γ) for control, SC, and MPC samples in the top part of the table, and austenite and cementite (V_θ) only for the control sample in the bottom half, which is the only sample with primary cementite particles.

Analysis method	Treatment	Volume fraction retained austenite		
		Control	Surface cracked SC	Martensite cracked MPC
tetragonality deduced from $020_{\alpha'}$ and $121_{\alpha'}$, only non-overlapping peaks used to determine γ content	Q	0.05	0.14	0.15
	Q-T	0.04	0.12	0.12
	Q-T-RCF	0.04	0.10	0.11
tetragonality deduced from $020_{\alpha'}$ and $121_{\alpha'}$, all peaks (including those that overlap) used to determine γ content	Q	0.06	0.16	0.14
	Q-T	0.05	0.12	0.12
	Q-T-RCF	0.05	0.08	0.11
		Control sample only		
		V_γ	V_θ	
tetragonality deduced from $020_{\alpha'}$ and $121_{\alpha'}$, all peaks (including those that overlap) used to determine volume %	Q	0.05	0.09	
	Q-T	0.04	0.05	
	Q-T-RCF	0.05	0.05	

After surface roughness measurements (table 4.4), the three different specimens were subjected to RCF testing until failure. The Hertzian pressure used (3.5 GPa) is greater than the normal wind turbine gearbox bearing operating pressure of 1-2 GPa [133], but was selected due to experimental time frames and test rig limitations. The results are presented in table 4.5. Since the test specimens are 12 mm long, several RCF tests can be conducted on the same sample but at different positions along their lengths. These different tests are denoted by the number next to the sample identifier e.g. MPC-1 and MPC-2.

Table 4.4 Average (R_a) and root mean squared (R_q) surface roughness values for each RCF specimen.

Sample	R_a / μm	R_q / μm
Control	0.08±0.02	0.13±0.04
SC	0.06±0.01	0.08±0.01
MPC	0.06±0.01	0.08±0.01

Table 4.5 RCF cycles for the crack-free (control) and pre-cracked samples (SC and MPC) all running at room temperature, 3600 rpm, and 3.5 GPa of Hertzian pressure.

Test	Cycles	Time / h	Reason of stoppage
Control-1	2.9×10^8	558.1	Excessive vibration
MPC-1	8.6×10^6	16.8	Lubrication system failure
MPC-2	2.8×10^8	551.2	Load bolt and spring got loose
SC-1	8.6×10^8	1672.5	Excessive vibration

After RCF, the three samples were cut along the circumferential cross section and the longitudinal section as illustrated in fig. 4.2. Careful metallographic preparation including nickel plating and mounting on hard bakelite (with silica or alumina additions) was needed to avoid rounding of the edges of the specimens where the majority of the RCF effects are manifested. Characterisation of these regions was performed mainly using optical microscopy since white-etching matter is defined as such due to its relative colour when etched in nital. Under SEM, WEM does not necessarily appear brighter than the matrix, but can be differentiated due to topographical contrast. Fig. 4.6, 4.7, and 4.8 show an ensemble of optical and SEM micrographs of the most notorious WEM manifestations around cracks, although butterflies are also included, in each of the three samples tested under RCF.

The WEM generated around microcracks and inclusions during RCF was then characterised mechanically, optically, chemically, and crystallographically using nanoindentation, FIB/TEM, EDS, and EBSD in order to identify the type of WEM generated (hard or soft) and provide insights on its formation mechanisms. In the case of nanoindentation, only the sample containing martensite-plate cracks was analysed given the larger size of WEMs present that allowed indents to be fully contained in the WEM regions of either butterflies or

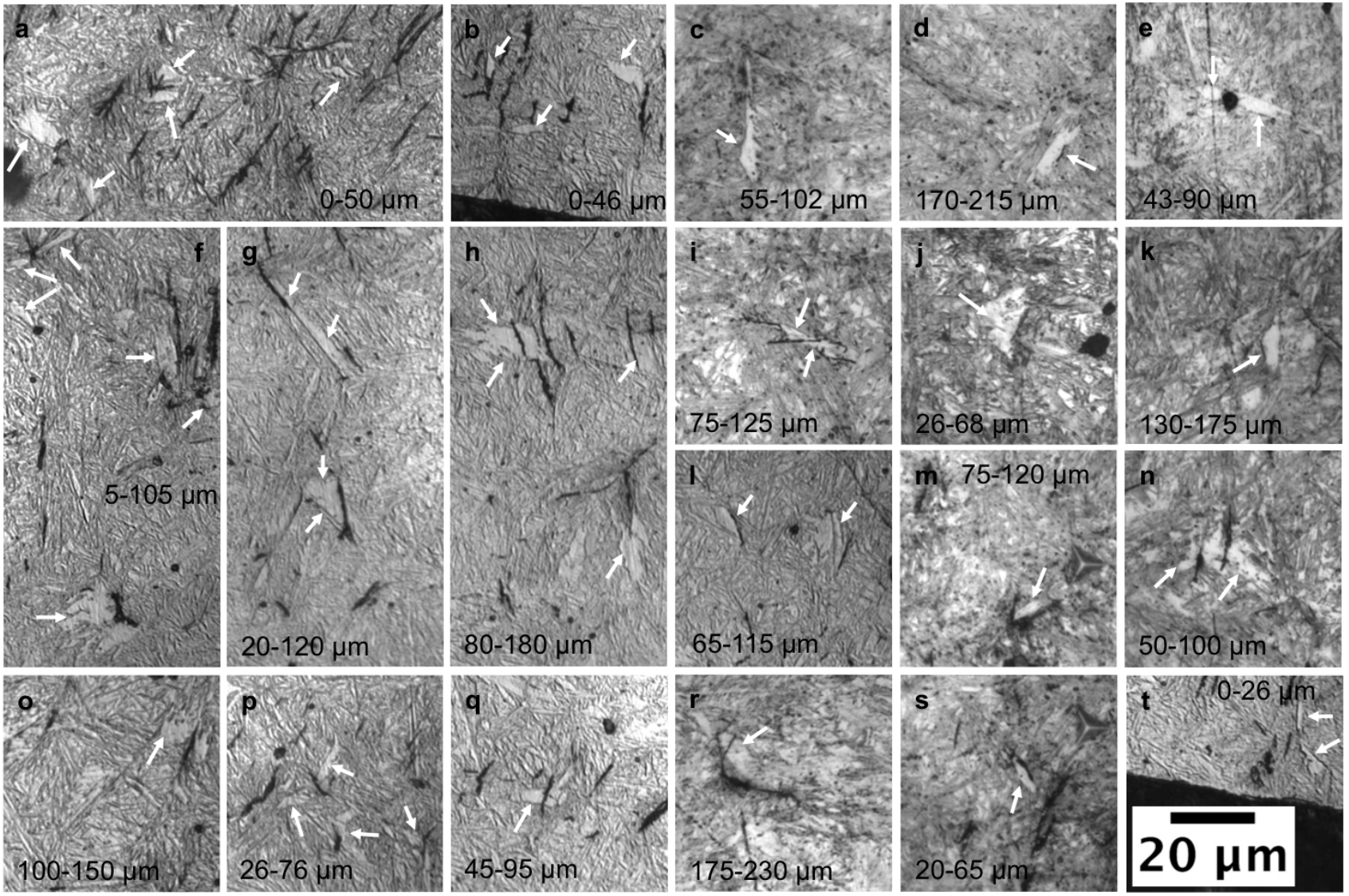

Fig. 4.6 WEM regions around cracks and inclusions (butterflies) in MPC sample. The depth range of the region photographed, relative to the contact surface is indicated on each image. The white arrows show the location of the WEM. All optical micrographs share the same magnification and have a similar orientation with respect to the free surface, which is shown in (t).

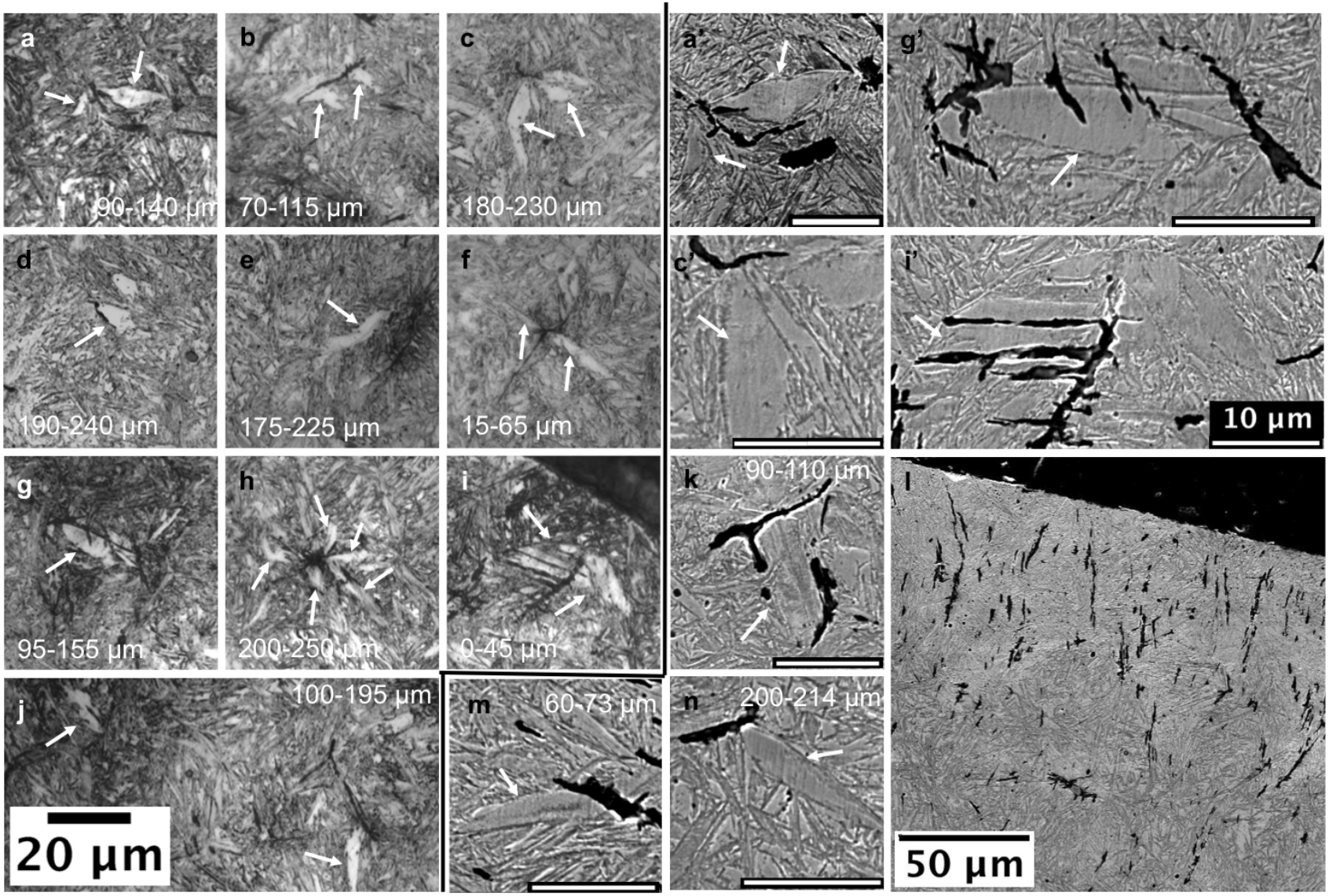

Fig. 4.7 WEM regions around cracks and inclusions (butterflies) in SC sample. The depth range of the region photographed, relative to the contact surface is indicated on each image. The white arrows show the location of the WEM. All optical micrographs (a-j) share the same magnification. All SEM images (a', c', g', i', k-n) to the right of the black line have a scale bar of 10 µm unless indicated. The images (a', c', g', i') are SEM versions of the same features shown in (a, c, g, i), with a slight difference in magnification and orientation.

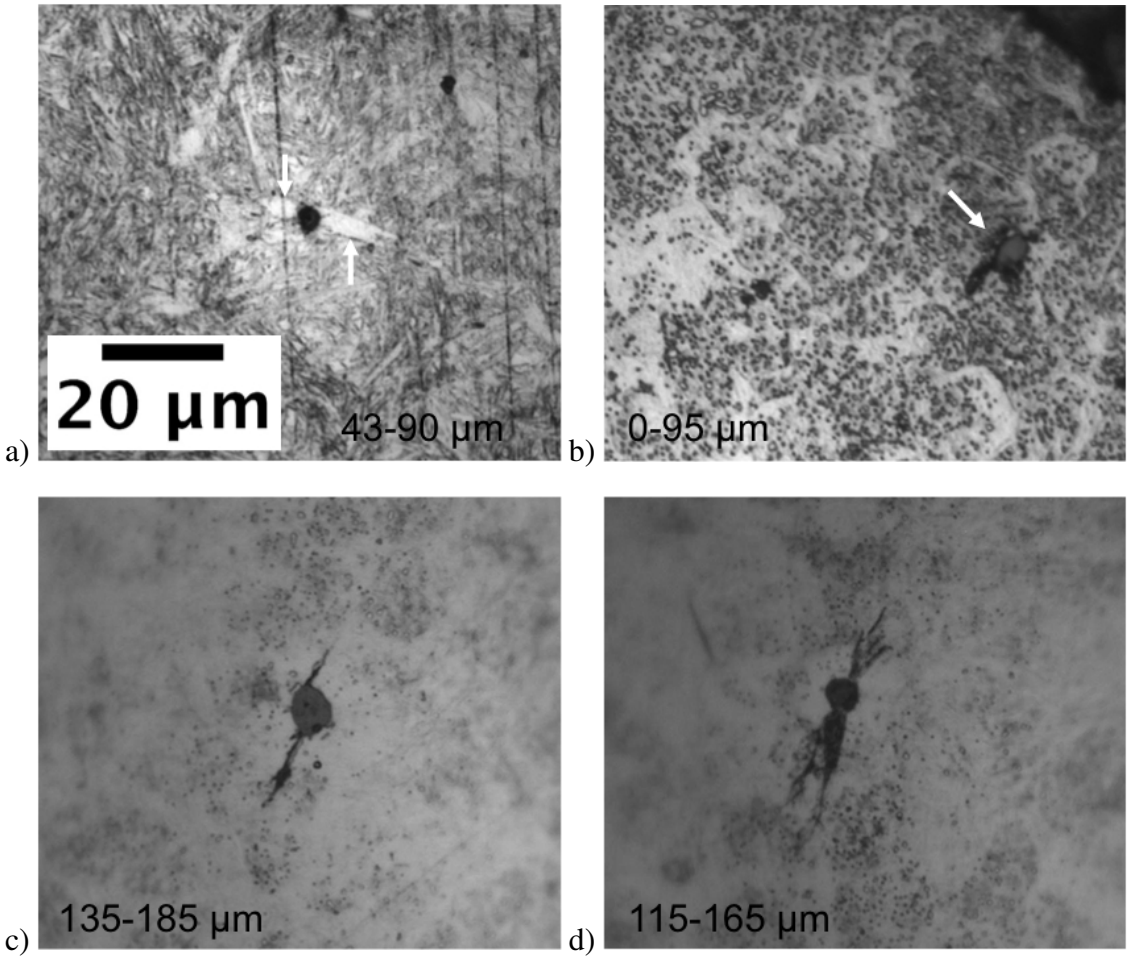

Fig. 4.8 WEM regions around cracks and inclusions (butterflies) in control sample. The depth range of the region photographed, relative to the contact surface is indicated on each image. The white arrows show the location of the the WEM butterfly wings. All optical micrographs share the same magnification.

cracks. These results are presented in table 4.6. An image of some of the indented regions is shown in fig. 4.9.

Table 4.6 Nanohardness values of the WEM and matrix of sample MPC using a constant indentation depth of 1000 nm.

Region	Nanohardness / GPa
WEM	12.3±0.2
Matrix	11.3±0.6

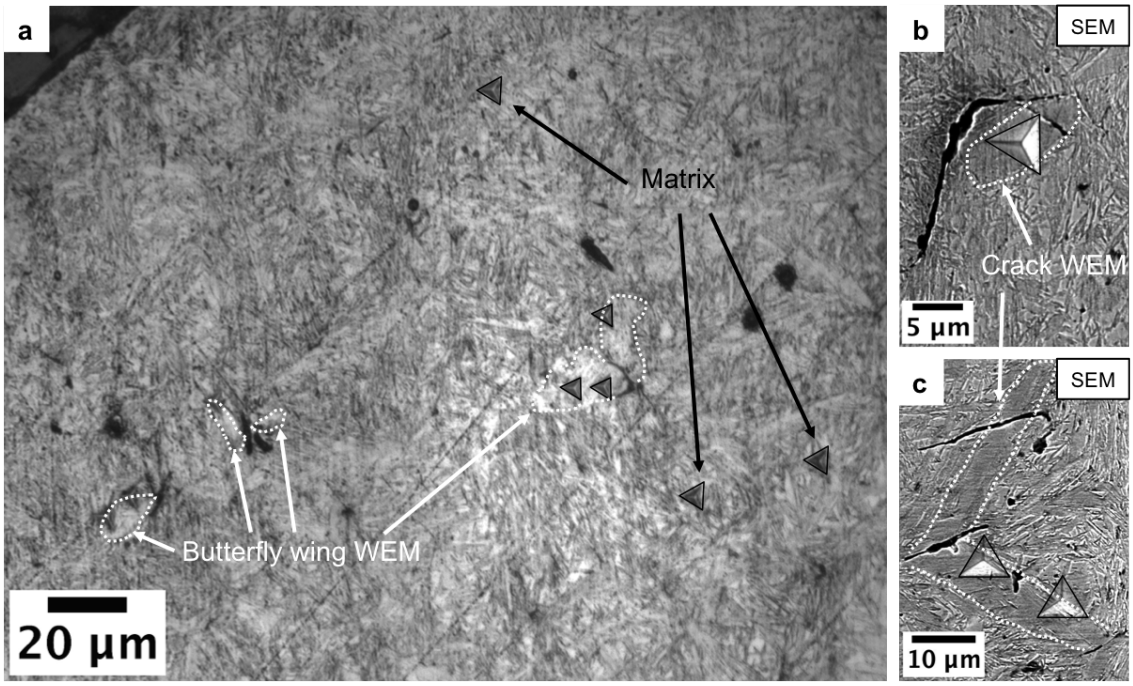

Fig. 4.9 SEM image of some of the nanoindentations performed on the MPC sample.

Following nanoindentation, WEM around cracks and inclusions was extracted from the bulk using focused ion beam machining according to the sequence portrayed in fig. 4.10. SEM images of the location of the extracted lamellae are shown in fig. 4.11, 4.12, and 4.13 along with TEM images of the lamellae themselves and diffraction patters of relevant features or regions. Finally, in fig. 4.14, a sequence of SEM images of lamella-2 (crack in SC sample) at several stages during the FIB thinning process is presented to give a 3D insight of the result of cracked-surface rubbing after long testing times.

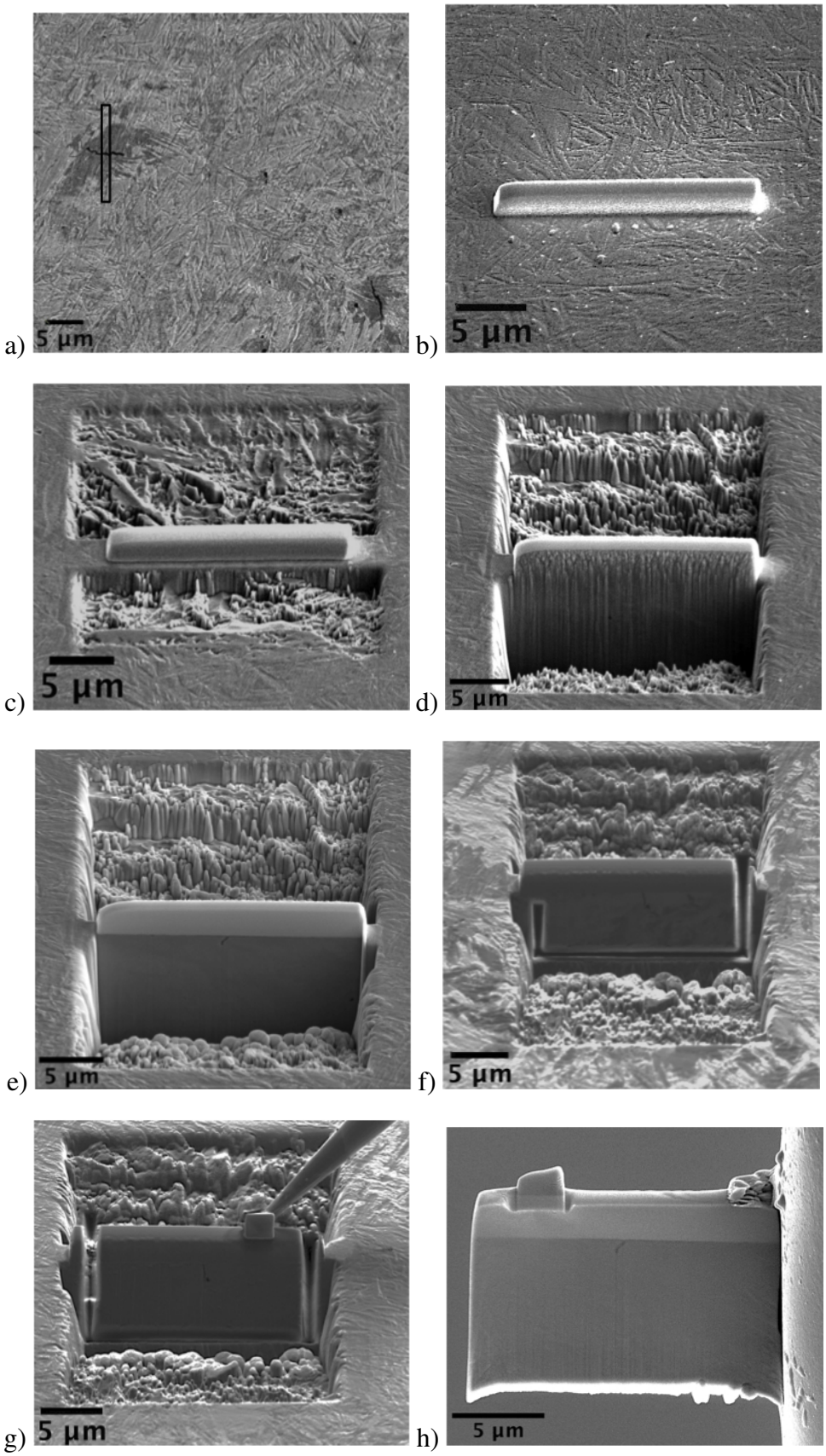

Fig. 4.10 SEM of FIB sequence followed to study the material around cracks and inclusions by extraction of thin lamellae. This sequence refers particularly to lamella-3 (fig. 4.13).

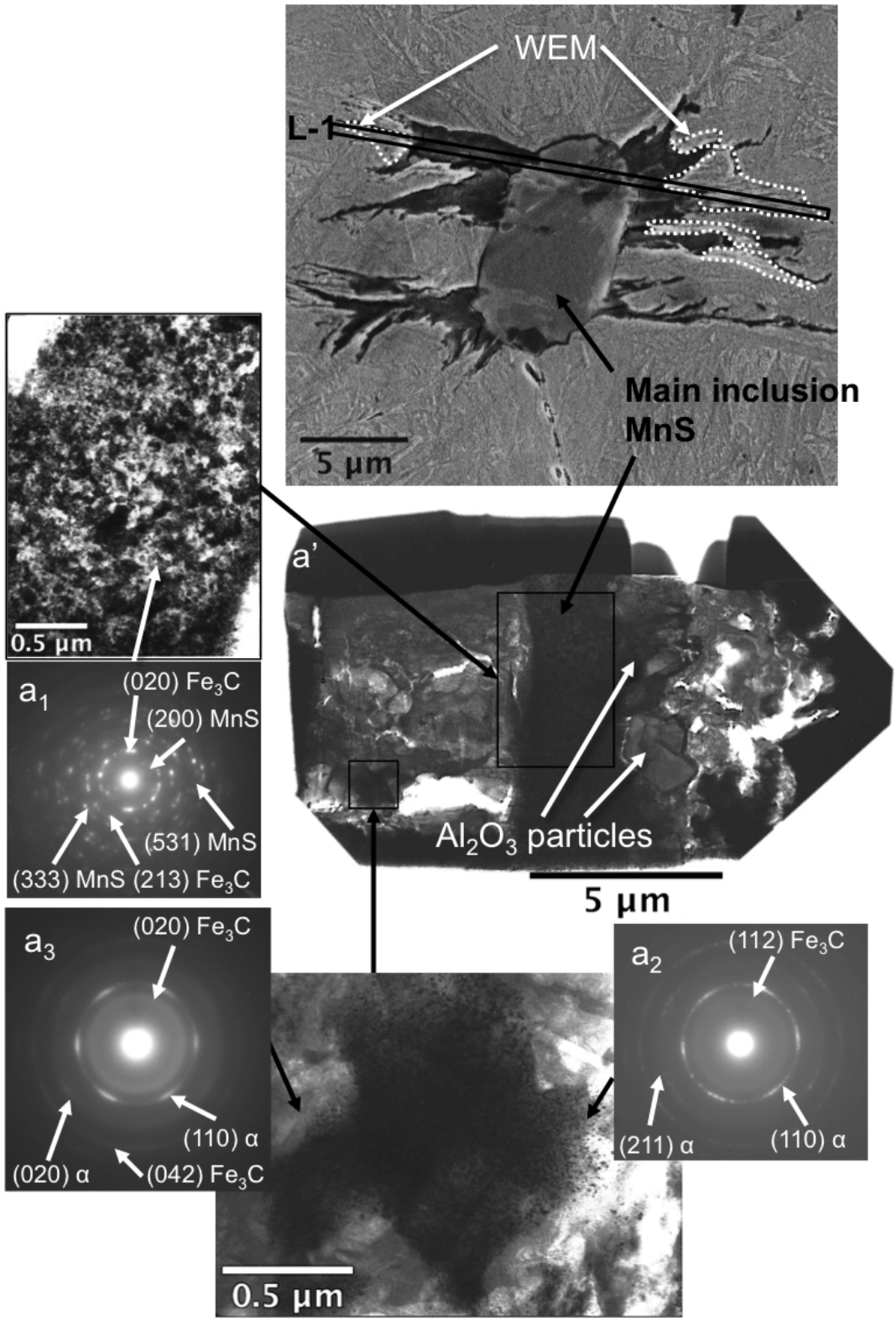

Fig. 4.11 SEM image of FIB milling location and TEM image of extracted lamella for inclusion 50 µm deep in SC sample tested for 1672.5 h (8.6×10^8 cycles).

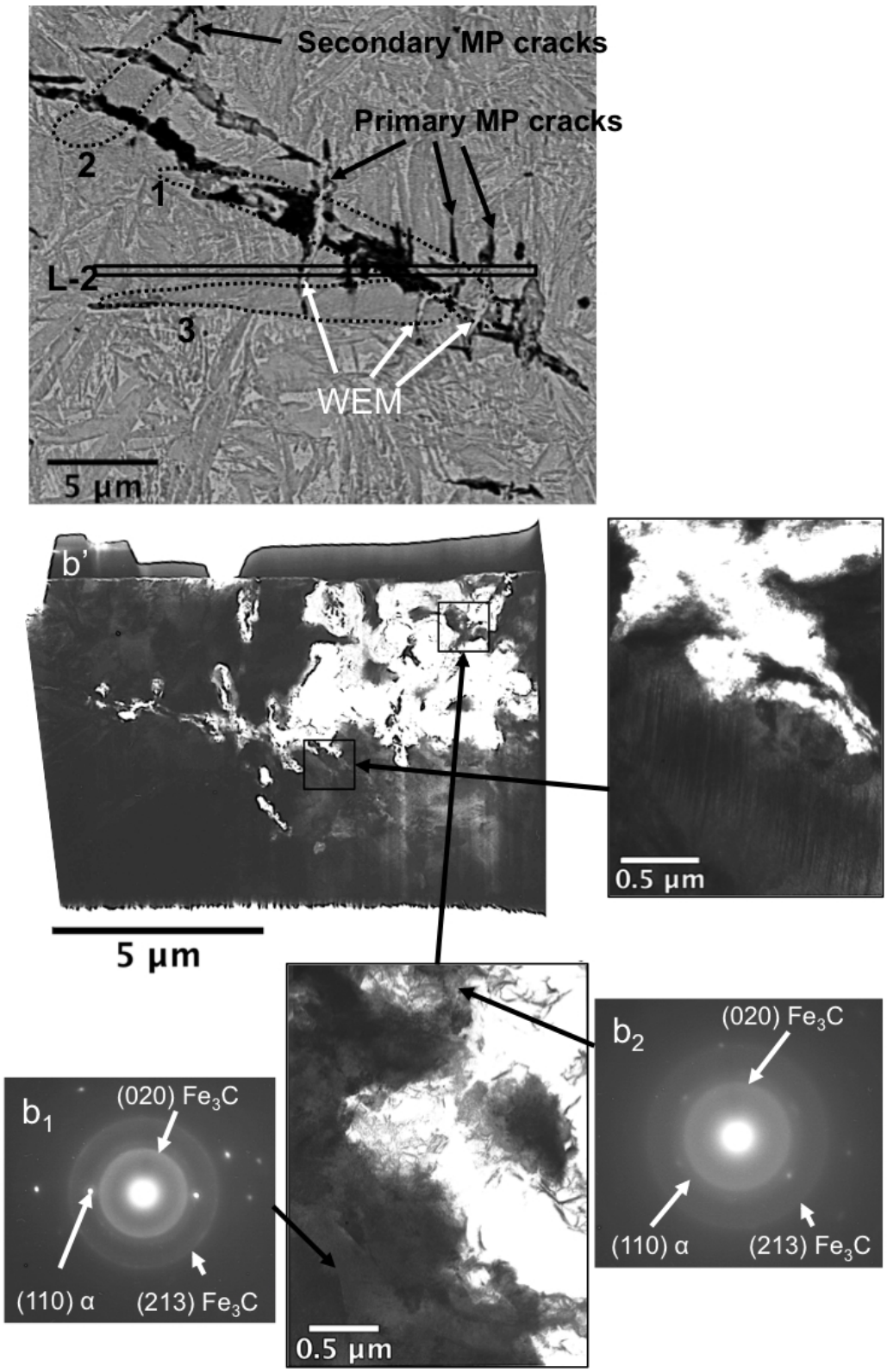

Fig. 4.12 SEM image of FIB milling location and TEM image of extracted lamella for crack 120 µm deep in SC sample tested for 1672.5 h (8.6×10^8 cycles).

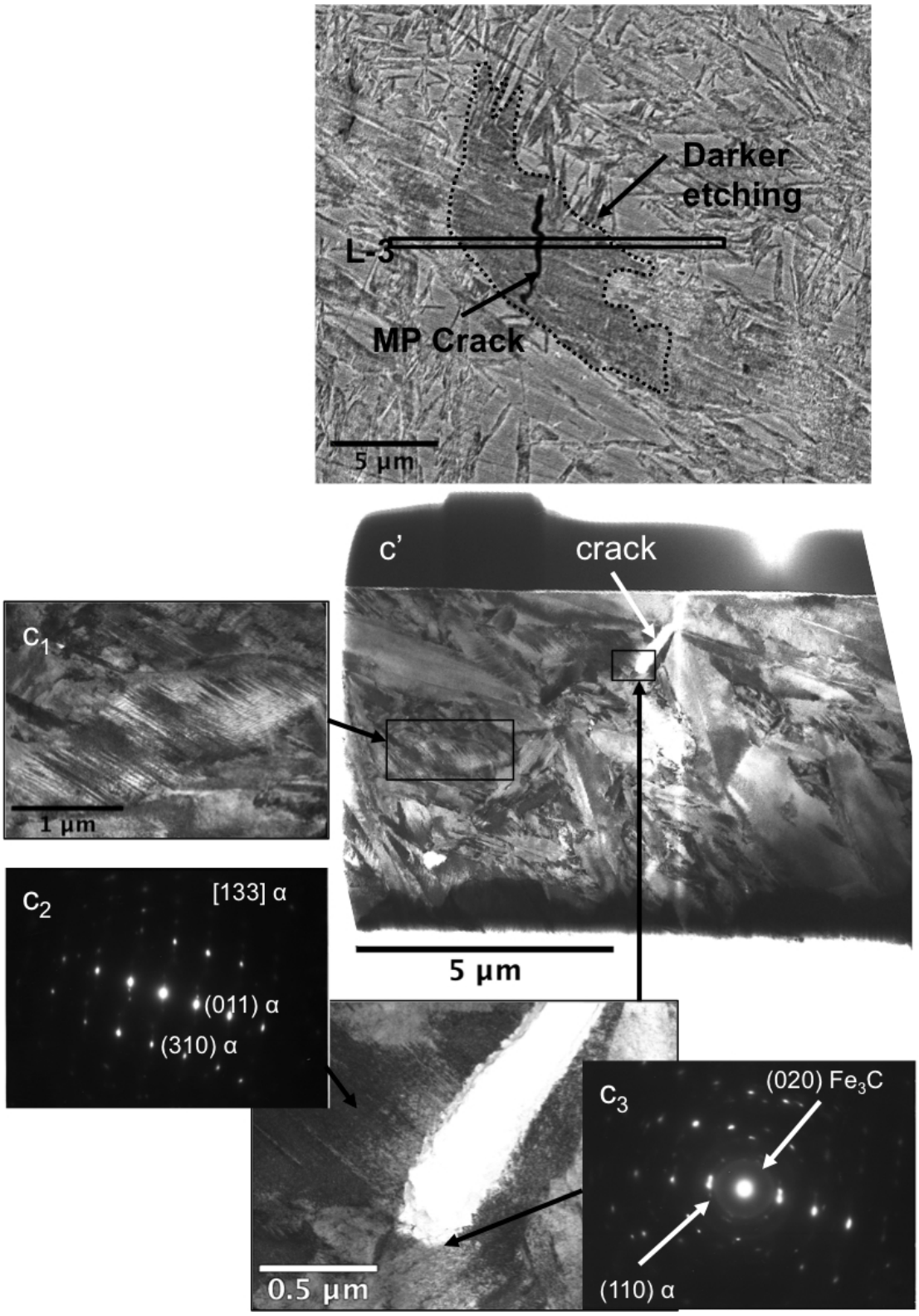

Fig. 4.13 SEM image of FIB milling location and TEM image of extracted lamella for crack 500 µm deep in MPC sample tested for 16.8 h (8.6×10^6 cycles).

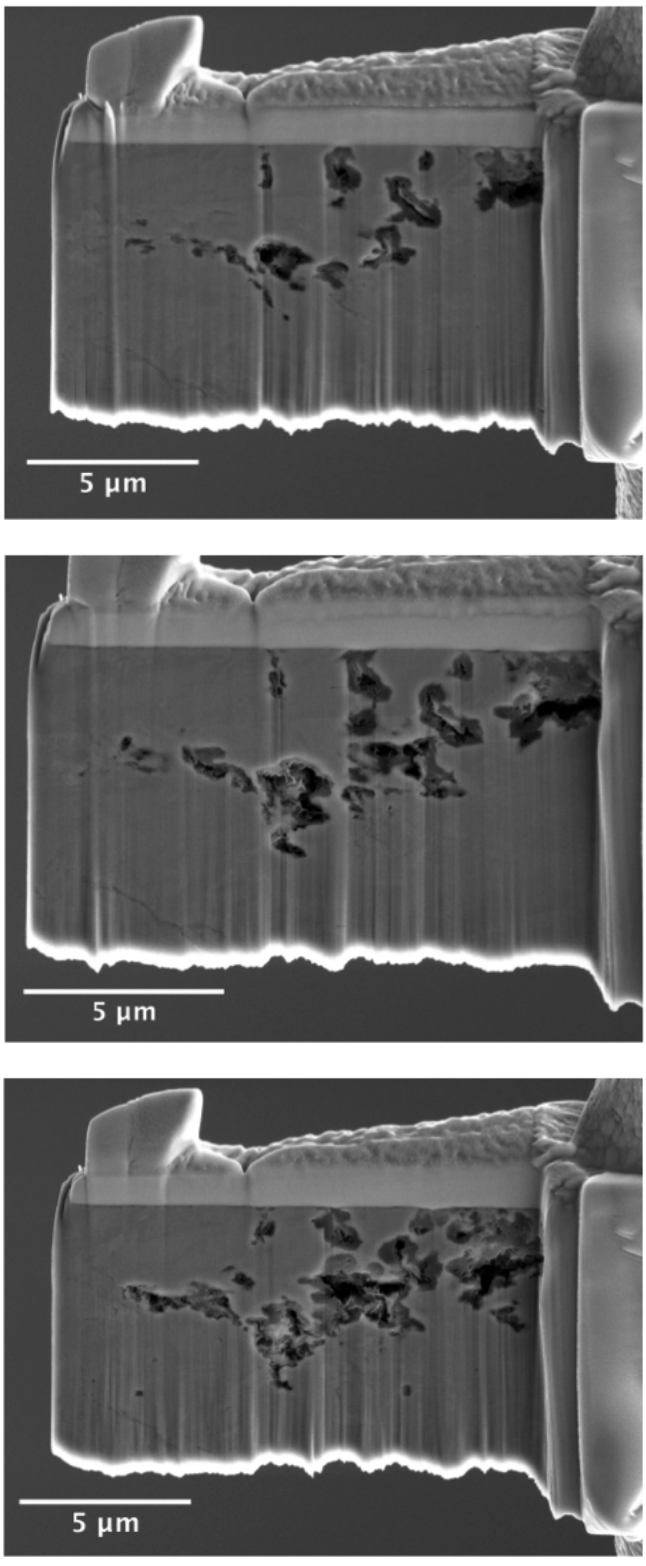

Fig. 4.14 SEM images of serial cross sections of the crack in lamella-2 (crack in SC sample, 120 µm deep, tested at RCF for 1672 h) during FIB preparation.

During microscopy of the circumferential cross section of the MPC specimen, a large crack approximately 1.7 mm long was found at a depth of around 400 µm. Its large dimensions and the considerable number of large inclusions entrapped in the path of the crack indicate that it might have formed during RCF. In order to determine its extent, the sample was sequentially ground and examined. Four cross sections are shown in fig. 4.15. Throughout the sections, no connections of this crack with the free surface were found. The crack was analysed using EBSD (fig. 4.16) to determine if it propagated along the prior austenite grain boundaries, which would evidence the relatively poor toughness of 52100 steel. Furthermore, five inclusions found in section d), but some still visible in c), were analysed using EDS to determine their chemical composition.

Continuing with the characterisation of the WEM generated, EDS was used to determine the chemical composition of the WEM compared to the matrix as well as analyse the composition of inclusions that caused butterflies (lamella-1) and fatigue cracks (fig. 4.15). The results of this analysis are presented in table 4.7.

4.4 Discussion

4.4.1 Heat treatments

As seen in fig. 3.11 and 3.7, the crack-forming heat treatments created a wide range of crack morphologies that allowed a detailed study of damage/ subsurface stress interaction. Whereas the MPC treatment created a fine dispersion of martensite plate cracks across the bulk, in orientations determined by the martensite habit-planes, the SC treatment led to radial, non-surface-breaking martensite plate and grain boundary cracks of different lengths and widths. Besides the cracks, these two pre-cracked samples have large grained high carbon tempered martensitic microstructures with an absence of primary carbides due to the high austenitisation temperatures and long times [48, 49]. The control sample heat treated using the standard procedure has finer lower carbon tempered martensite and primary carbides up to 1 µm in diameter.

Despite the different heat treatments and resulting microstructures, the macrohardness values of all three samples are relatively close and above the engineering requirement of 58 HRC (650 HV) [35], which allows a valid comparison of the RCF response of the samples.

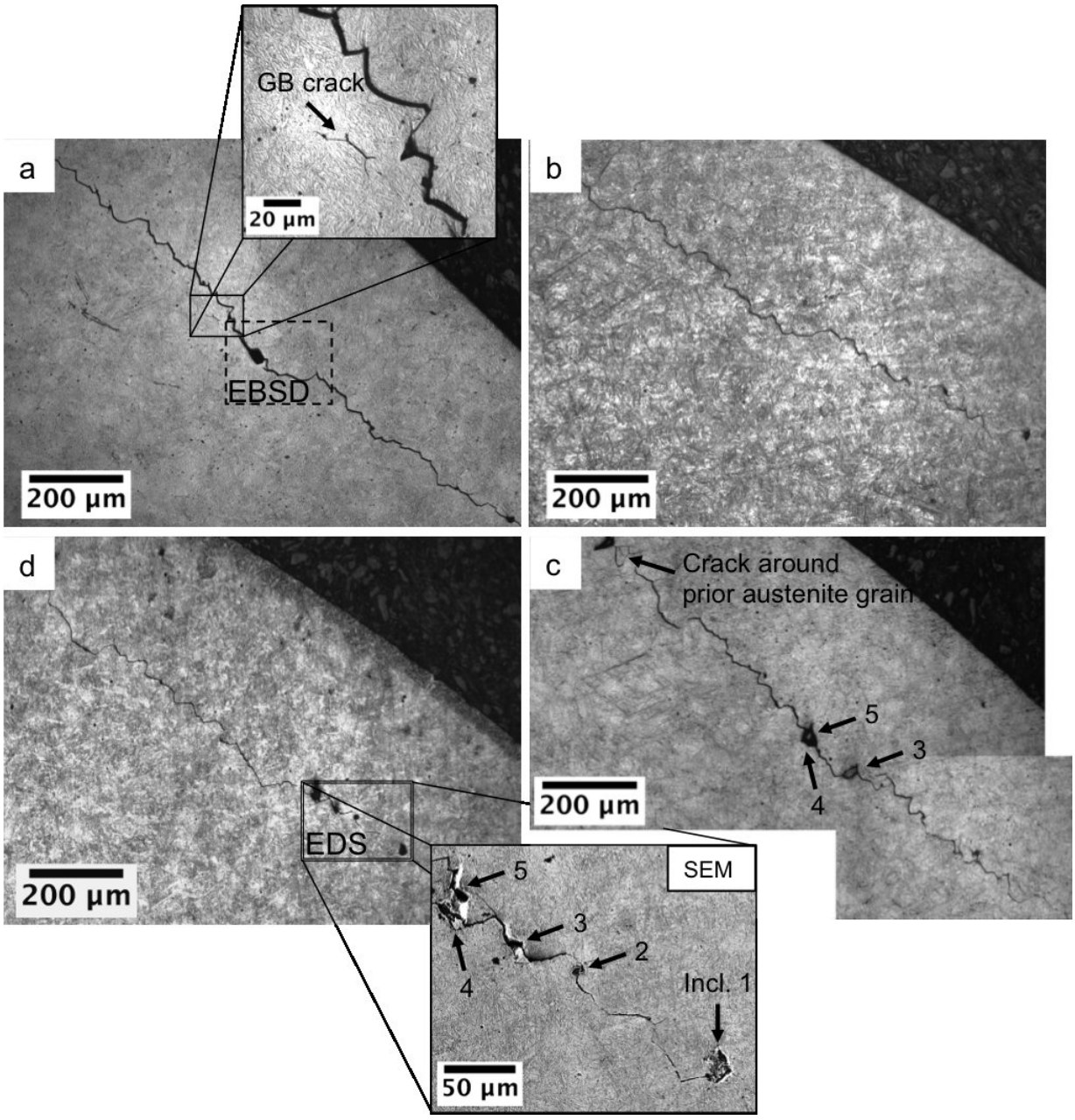

Fig. 4.15 Large crack found in the circumferential cross section of the MPC sample showing four sectional images of the same region. In a) is shown a smaller grain boundary (GB) crack denoting the lack of toughness, or cracking proneness, of the alloy and in d) a series of inclusions that are likely to have been the crack initiators. The distance from inclusion 5 to the crack tip to the left is 948 µm and to the right crack tip, 738 µm.

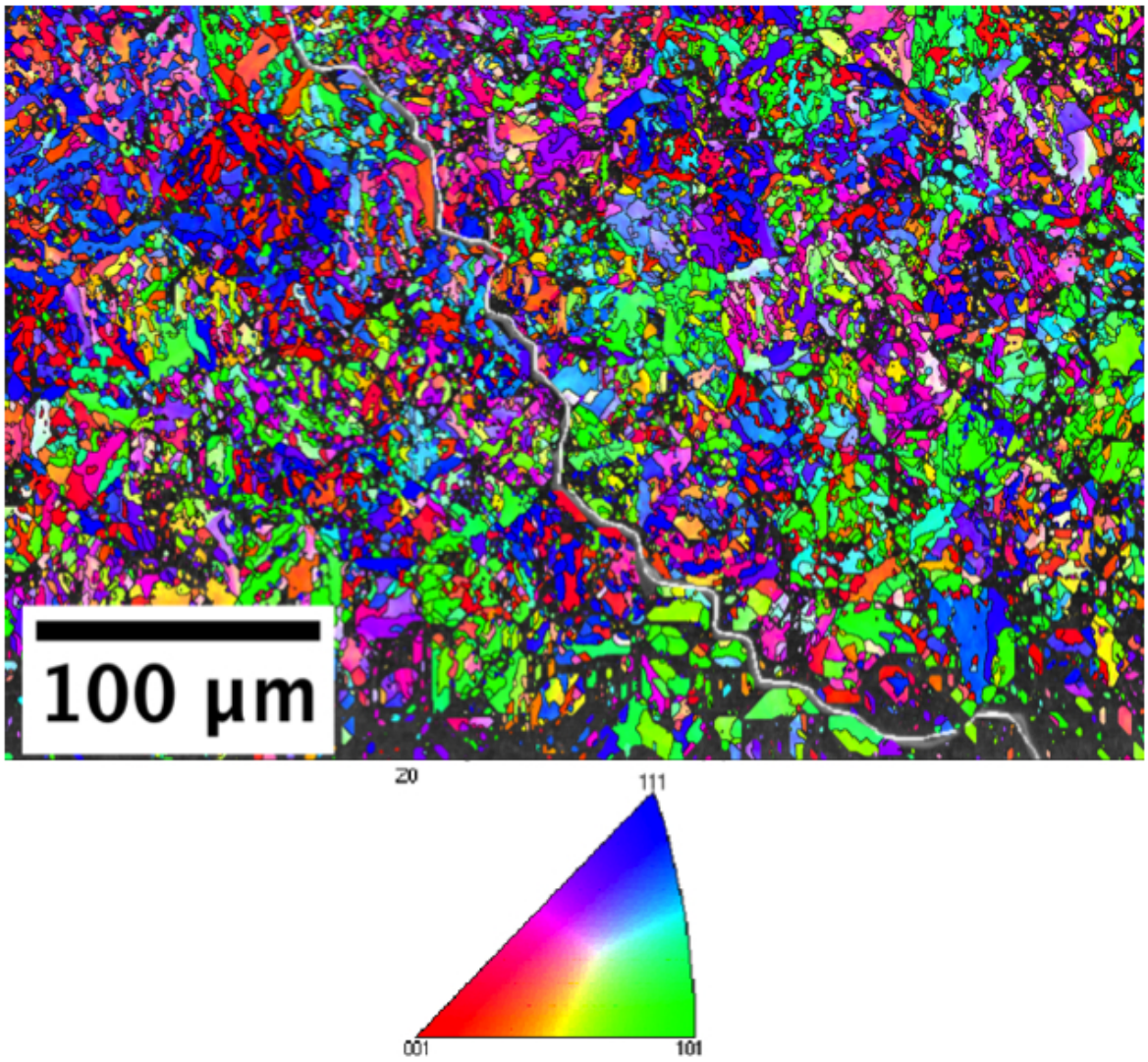

Fig. 4.16 Inverse pole figure coloured EBSD map of a section of the fatigue crack (highlighted in white) in MPC sample. The colour key corresponds to BCC Iron.

Table 4.7 Average values of energy dispersive spectroscopy data from the matrix and WEM around cracks and inclusions (butterflies) using FIB/TEM samples and SEM samples. The inclusions that most likely originated the RCF crack of fig. 4.15 and 4.16 were also analysed.

Sample	Region	Elemental composition (wt%)										
		Al	Si	P	S	Ca	Cr	Cu	Mn	Mo	O	Fe
L1 [SC]	WEM of butterfly	-	-	-	0.59±0.15	-	3.24±0.37	-	0.33±0.21	-	-	95.81±1.87
	Matrix	-	0.11±0.07	-	0.72±0.12	-	1.93±0.21	-	1.25±0.19	-	-	95.97±1.39
	Butterfly main inclusion	0.2±0.01	-	-	29.83±0.22	-	1.23±0.05	-	57.02±0.33	-	2.52±0.11	9.17±0.14
	Butterfly secondary inclusion	59.1±0.39	-	-	0.21±0.02	-	0.03±0.01	-	0.21±0.01	-	40.12±0.52	0.28±0.02
MPC	WEM of crack	-	0.35±0.03	-	-	-	1.65±0.15	-	-	-	-	98.00±1.95
	Matrix	-	0.45±0.03	-	-	-	1.50±0.13	-	-	-	-	98.05±1.95
EBSD1 [MPC]	Inclusion1	-	0.46±0.03	0.23±0.02	0.39±0.03	0.19±0.02	1.59±0.15	-	0.26±0.02	-	13.08±0.44	83.78±1.19
	Inclusion2	2.55±0.21	0.29±0.03	-	4.08±0.2	-	2.25±0.21	-	11.65±0.37	-	11.66±0.37	67.52±0.73
	Inclusion3	-	0.40±0.03	-	0.20±0.02	-	1.68±0.17	-	-	-	4.70±0.23	93.01±1.58
	Inclusion4	-	0.42±0.03	0.22±0.02	0.29±0.03	-	1.83±0.21	0.42±0.03	0.33±0.03	-	8.10±0.32	88.39±1.22
	Inclusion5	-	0.34±0.03	0.22±0.02	0.20±0.02	-	1.72±0.17	-	-	-	5.24±0.26	92.28±1.54

4.4.2 Retained austenite

The retained austenite data presented in table 4.3 show a consistent trend, that V_γ increases with austenitisation temperature and time, with a tendency for decrease upon tempering and rolling contact fatigue testing.

According to Voskamp, the values of retained austenite during RCF decrease depending on the number of cycles and Hertzian pressure applied [28]. For example, for 3.5 GPa it should be 0.03 after 2.8×10^8 cycles and virtually no retained austenite after 8.6×10^8 cycles. Due to experimental limitations, the present study did not allow precise measurement of the quantity of retained austenite after RCF in the small subsurface volume ($\sim$100 µm thick and $\sim$100-500 µm deep depending con Hertzian contact pressure and cycles) that experiences the largest shear stresses, the results reflecting an averaged determination from regions subjected to different levels of stress, which explains why these values are larger than reported ones and very similar to that of the Q-T samples. To avoid this averaging, Voskamp performed repeated XRD measurements using Mo K_α radiation and a spot size of only 1 mm^2 on continuously rotating inner bearing rings with one measurement per depth level after layer removal through electropolishing of the whole ring, but such technique was not accessible in this study [28].

The larger retained austenite contents of samples SC and MPC will be shown in subsequent discussion to play an important role in the generation of WEM.

4.4.3 Surface roughness and RCF testing

Before analysing the RCF response of each sample in terms of WEM generation it is important to note the relationship between the cycles that each sample ran for and parameters that can lead to failure attributable to surface roughness or the consequences of retained austenite. As seen in table 4.4, the surface roughness of the pre-cracked samples was lower than the crack-free one, however both control and MPC specimens ran for almost the same amount of time ($\sim$550 h). Instead, despite MPC and SC having almost identical surface roughness values and retained austenite contents, SC ran for over three times longer than MPC, indicating counterintuitively, that the subsurface case of cracks created by indenting played a key role in *enhancing* RCF life.

Microscopy demonstrated that the initial radial microscopic and grain boundary cracks in sample SC had propagated and branched, thus toughening the steel in a manner similar

to the behaviour of other brittle materials [162, 163]. The indentation cracks introduced prior to RCF testing, and any cracks in martensite plates, serve to deflect the contact-stress induced fractures. The initial microscopic cracks in martensite plates are themselves randomly oriented on a macroscopic scale and hence serve the same purpose; this is evident in fig. 4.12 where two roughly normal families of martensite plates, 2 and 3, had their cracks propagated and intersected in 1 causing deflection of at least five crack paths (three vertical and two roughly horizontal).

Many voids and cavities where discovered when a TEM lamella (L-2) was carved out of region 1 where the cracks intersect (figs 4.14 and 4.12b'). Evans observed similar voids in the non-WEM side and at the tips of butterfly cracks, which led him to conclude that these coalesce to form butterfly cracks at defects, and that the formation of WEM is cooperative with the propagation of such crack [164]. In the SC sample, microcracks were already present before RCF and the diffraction patterns of fig. 4.12 reveal in b_1 (away from crack edge) an amorphous-type structure of carbides in a body centred cubic (BCC) ferritic matrix and in b_2 (closer to crack edge) the same carbide structure and a faint presence of small ferrite crystallites, i.e. WEM in its very early stages. This evidence suggests that voids do get generated during RCF but only propagate pre-existing cracks rather than creating them and that WEM generation is not cooperative [164] or simultaneous [126], but posterior to damage.

When examining the amount of WEM generated in the three samples tested, it was seen that most WEM in the MPC sample (551.2 h) occurred at depths consistent with the $\tau_{xz,max}$ (99 µm), whereas for the SC sample (1672.5 h) more counts were found in the depth of the τ_{max} (190 µm). Note that in the SC sample, the maximum depth at which cracks remain after grinding and before testing is $\sim 300\,\mu m$. In the case of the control sample (558.1 h), all WEM counts were related to butterfly wings and found between 10 and 100 µm deep. This is because the SC and MPC samples contain pre-existing cracks, some of which are appropriately located to begin the process that leads to WEM formation, whereas an initiation stage is necessary in the case of the control sample, and this initiation must occur in the most highly stressed region. Although it is clear from the images of fig. 4.6, 4.7, 4.8 that more WEM regions were found in the pre-cracked samples, all three samples had similar amounts of butterfly wing WEM since all were manufactured with the same material and roughly contain the same amount of inclusions. It is also worth clarifying that the butterfly cracks of the inclusions in the control sample shown in fig. 4.8 are oriented either parallel or up to 45 ° to the rolling surface and that not all (fig. 4.8b, c, and d) exhibit WEM as butterfly

cracking at inclusions occurs at different times of the RCF life, mainly depending on the inclusion depth, size, and interface with the matrix [132].

4.4.4 WEM characterisation

When analysing the WEM formed in RCF tested samples, it was clear that the morphology of the cracks along with the presence of primary or secondary carbides around cracks plays an important role in WEM generation.

Although no direct relationship was found between the orientation or length of cracks and WEM, crack orientation is a parameter that must interact with the subsurface shear stresses and the rolling direction. In other words, the contact-induced stresses will promote closing of certain regions of a crack or the separation of crack faces depending on the crack-orientation. In general, the narrower regions of the crack develop more WEM due to more intense rubbing of their surfaces. It is clear how the narrower cracks in the MPC sample developed more WEM than the wider ones in the SC sample, despite the fact that the latter sample survived almost three times longer (fig. 4.6 and 4.7). Nevertheless, some surface-cracks, such as those observed in fig. 4.7a', m, and n, appear relatively wide, possibly due to an etching effect since these cracks are in fact surrounded by WEM and do not show evidence of branching.

The location of cracks with respect to certain microstructural features also influenced WEM generation/absence and two cases were identified: 1) cracks surrounded by the tempered martensitic matrix, and 2) cracks in contact with retained austenite. It is important to bear in mind that there were no primary carbides in samples SC and MPC because of the high austenitising temperatures used, so that the wavy lines found in white-etching areas of butterfly wings for example (see inside dotted white line of fig. 4.11), are not due to be elongated carbides as is sometimes claimed [164].

In the first case, fine carbides resulting from the tempering of martensite dissolve upon crack rubbing, allowing WEM formation. As Loy and McCallum established, WEM is carbon supersaturated nanosized ferrite [118]. Due to a high austenitisation temperature and long time, all the cementite in MPC and SC samples was fully dissolved so the only dissolvable carbides to supersaturate the ferrite upon crack rubbing are tempering carbides. This was corroborated through TEM fig. 4.11 and 4.12 where no crystalline tempering carbides were seen near cracks, only amorphous rings likely corresponding to extremely fine carbides in the process of dissolution. In the second case, cracks under RCF acting as stress

concentrators cause the stress-induced transformation of the neighbouring retained austenite into untempered martensite, which then is free from primary and secondary carbides to be dissolved into solution and form hard white-etching matter, i.e. carbon supersaturated nanosized ferrite [118, 126]. The stress-induced martensite shows dark contrast (in SEM) in the vicinity of the cracks (see fig. 4.13), which should not be confused with the dark-etching regions thought to be an over-tempering of the microstructure [113, 115]. In this second case, observations tend to suggest that either very little or no WEM at all is formed for the amount of cycles tested since carbon would have to be made available through autotempering or short-circuiting via dislocation clouds, for example. Since the pre-cracked samples had more retained austenite, the cracks that after RCF were not surrounded by WEM are likely to be either formed at late stages of the RCF process, neighbouring retained austenite regions, not in the regions of maximum subsurface shear stress, or sliced in a plane in which WEM is not visible.

4.4.5 Nanohardness

It is well-known that nanohardness values reported in GPa differ considerably from the macrohardness HV30 values because of the small volume of material involved in the former case [165, 166]. However, the relevant fact is that the WEM is approximately 9% harder than the matrix although the indents are just a few micrometres away from the cracks (table 4.6, fig. 4.9). It is possible that this represents an underestimate because of the relatively small size of the WEM regions and the necessarily close proximity of WEM to the cracks. When larger regions of WEM have been studied, most reported values are found to be 30-50% harder than the surrounding matrix [125, 126] mainly due to the carbon supersaturated composition of WEM, but also to its nanosized structure. However, other authors have reported a hardness only 5% higher than the matrix for WEM layers formed in hard-turned AISI O1 steel [167].

4.4.6 FIB/TEM

By analysing the images and diffraction patterns of one inclusion and a crack in the SC sample and one crack of the MPC sample, it was possible to obtain a wide spectrum of detail on the deformation mechanisms that take place during RCF and lead to the formation of WEM. The cross section of a butterfly 50 µm deep (fig. 4.11) reveals three interesting features: (i) the main inclusion, later confirmed to be MnS through EDS, has a very fine grained structure as seen in the micrograph and through its ring-like diffraction pattern indexed as MnS and M_3C carbide (a_1). This structure is surprisingly similar to that of WEM

(nanosized crystallites), possibly because the attached hard Al_2O_3 particles focus the strain on the soft MnS in a similar fashion as hard inclusions beat on the softer ferrite around them during RCF promoting carbide dissolution and recrystallisation that give rise to the carbon supersaturated nanosized ferrite known as WEM. (ii) At the tip of one of the butterfly cracks, a region of very small grains (a_2) was found, which was indexed as nanosized ferrite with a faint halo of amorphous-like carbide. (iii) Regions further away from the butterfly crack where no small grains were present were indexed as a single but heavily deformed ferrite crystal with a heavy presence of amorphous-like carbide.

When comparing these observations with a deflected crack, in the same sample, and 120 µm deep (fig. 4.12), the cross section revealed a crack with faces widely separated, possibly propagated through the presence of voids, that had: (i) twinned regions very close to crack surfaces, possibly stress-induced mechanical twins (fig. 4.12b'), (ii) regions further away from cracks (b_1) that were indexed as undeformed ferrite crystals with a strong dispersion of amorphous-like carbide, and (iii) regions very close to the crack surfaces (b_2) that had a lighter amorphous-like carbide response and a weak peak of small ferritic crystallites. In conclusion, wherever there is a presence of nanosized ferrite, the amount of amorphous-like carbide seems to diminish compared to regions where ferrite is coarser and simply deformed (further away from cracks).

The inclusion and crack analysed in the SC sample had been subjected to a larger number of RCF cycles than the crack of the MPC sample (fig. 4.13). However, the MPC sample shows already after 16.8 h of RCF a more densely twinned region in the vicinity of the crack (c_2) when compared with normal regions of twinned martensite away from it (c_1). There also is amorphous-like carbide in the ferritic matrix near the crack tip. These observations seem to suggest that after the stress induced transformation of retained austenite neighbouring the crack to untempered martensite, the process of ferrite deformation through rubbing and eventual recrystallization (nanoferrite) is progressive but for the short running time of lamella 3, only the stress-induced transformation/deformation twinning took place.

4.4.7 EBSD

The large crack found in a cross sectional cut of the MPC sample exactly below the centre of contact (see fig. 4.15) was analysed through serial sectioning and EBSD which revealed at least twelve inclusions in the crack path, five of which were analysed using EDS. No WEM was observed around the crack, there were no connections with the free surface, and the crack showed wider and narrower crack sections depending on orientation relative to the

rolling surface. Sections of the crack sometimes followed prior austenite grain boundaries (fig. 4.15c), with adjacent nascent cracks at austenite grain junctions (fig. 4.15a). These observations suggest this is a subsurface fatigue crack initiated at inclusions, propagated through brittle grain boundaries and arrested near the free surface due to the compressive stresses developed during RCF. The EBSD map, initially 53% indexed but extrapolated to 76% using post-acquisition software as described in the experimental section, showed that the regions to the left and right of the crack path have different orientations confirming that the crack propagates along grain boundaries. Furthermore, EBSD confirms the lack of WEM in this crack as WEM is normally non-indexable due to the size of the ferrite crystallites (5-500 nm) and the high degree of localised deformation required to generate it [126]. None of the inclusions entrapped in the crack path displayed signs of WEM butterfly wings despite the fact that butterflies have been shown to form after 10^5 cycles ($\sim$11 min for the testing conditions used in this study) meaning that the lack of WEM around the inclusions and fatigue crack is likely to be because they are located over 200 µm away from the regions of maximum subsurface shear stresses [168, 169].

4.4.8 EDS

Measurements of the chemical composition of the WEM relative to the matrix were performed in two different scenarios (table 4.7). The WEM formed around an inclusion in the SC TEM sample using an EDS-STEM detector and secondly, WEM formed around a crack in the MPC SEM sample using an EDS-SEM detector. In both cases the results agree that the WEM has a higher chromium concentration than the matrix, which matches previous EDS analyses of white-etching areas [164]. The observation cannot be attributed to, for example, the deformation-induced dissolution of Cr-rich primary carbides that are not present in the SC and MPC samples. The reason behind the high concentration of Cr in WEM is not clear, but could be attributed to mechanisms such as a dissipative temperature increase due to the rubbing of crack faces, vacancy assisted diffusion, or a dislocation-mediated atom transport process [170].

EDS was also used to analyse the composition of butterfly and fatigue-crack causing inclusions. The results in table 4.7 confirm that the main butterfly inclusion of fig. 4.11a' (L-1) is manganese sulphide and the secondary inclusions are alumina. In the case of the inclusions of fig. 4.15, only inclusion 2 was clearly identified as a manganese sulphide with alumina encapsulation. Inclusions 1, 3, 4, and 5 appear to have fallen out during preparation, but the relatively high oxygen content picked up suggest they were a family of globular oxides, which are the second most common inclusion after sulphides in 100Cr6 steel [134].

4.5 Conclusions

Critical experiments using a wide range of mechanical tests and characterisation tools have permitted the following conclusions regarding the white-etching matter formation in bearings:

- Evidence has been provided to show that the presence of microscopic cracks in samples prior to RCF testing leads to the formation of hard white-etching matter in their close proximity, akin to the butterfly wings in conventional bearing tests. Therefore, hard white-etching matter is likely to be a symptom of microscopic fracture rather than the cause. During rolling contact fatigue, the crack faces rub and beat against each other, creating minute grains as a result of recovery and recrystallisation, with the possibility of the mechanical solution of fine cementite playing a role. Coarse primary cementite was absent in two of the samples studied and hence its presence is not a critical requirement for WEM formation.

  The corollary of this conclusion is that WEM can in principle be mitigated by increasing the toughness of the bearing steel, or in other words, increasing the energy required for cracks to form and propagate.

- Consistent with previous work, the WEM formed around inclusions (butterflies) and cracks is essentially nano-sized ferrite with a very fine distribution of carbide particles that is at an advanced stage of subdivision, so much so that these particles display an amorphous-like ring-diffraction pattern. This WEM was also found to be approximately 9% harder than the tempered martensitic matrix.

- In order to form WEM around cracks through the rubbing of surfaces two parameters are highly important: the width of the crack and the amount of carbides in the matrix around the crack. On the one hand, the orientation of the crack with respect to the rolling direction and the depth of subsurface shear stress will determine which part of the crack widens under the applied pressure and which contract, rub, and generate WEM. On the other hand, if austenitised in the γ phase field, cracks neighbouring retained austenite regions, that strain transform to untempered martensite under RCF seem to generate less WEM due to the lack of carbides compared to cracks found in tempered martensite. Since inclusions are better stress concentrators than cracks, no retained austenite is found around them but only tempered martensite, hence why they proved to be more effective WEM generators than cracks. Carbides act as a source of carbon to be dissolved through cyclic stress and supersaturate the nanostructured ferrite crystallites, which is what hard WEM is. Without carbides in the proximity,

ferrite deforms into nanosized crystallites, but does not get enriched by carbon so no hard WEM or very little is formed.

- Since the pre-cracked samples used in this work were austenitised in the γ phase field where all spheroidised carbides were dissolved, the wavy contours found in the WEM wings of butterflies are more likely to be flow marks rather than elongated carbides as previously believed.

- Just like hard inclusions under RCF are able to deform the softer steel around them by creating nano-sized ferrite with a distribution of very fine carbides, a hard oxide like alumina encapsulating a softer inclusion like manganese sulphide (duplicate inclusions) can create a nano-sized manganese sulphide structure with a very fine carbide distribution due to the beating action of the hard alumina particle.

- FIB-TEM characterisation of RCF samples confirmed the formation of voids and cavities around cracks and butterflies, which seem to widen and lengthen the existing cracks, but no evidence was found of those voids coalescing into newly formed cracks.

- Despite being counterintuitive, the surface cracked sample displayed the longest RCF life of all samples (more than three times longer) although it virtually had the same surface roughness and was tested under the same conditions. Micrographs show how these subsurface microcracks toughen the steel by deflecting damage through crack branching.

Chapter 5

Cracks in martensite plates as hydrogen traps

5.1 Introduction

In this chapter, the likelihood of employing the macroscopically homogeneous distribution of microcracks introduced into a martensitic bearing steel sample as hydrogen traps was studied. This phenomenon has been investigated through thermal desorption spectroscopy and hydrogen permeation measurements using both cracked and integral samples. The effective hydrogen diffusion coefficient through the cracked sample was found to be far less than in the un-cracked one. Similarly, when samples are charged with hydrogen, and then subjected to thermal desorption analysis, the amount of hydrogen liberated from the cracked sample is smaller due to the trapping by the cracks. Theoretical analysis of the data shows that the traps due to cracks are so strong, that any hydrogen within the cracks can never in practice de-trap and cause harm by mechanisms that require the hydrogen to be mobile for the onset of embrittlement. Finally, rolling contact fatigue testing was performed to analyse whether hydrogen trapping at cracks affected the mechanical integrity of the specimen.

5.2 Experimental Methods

5.2.1 Material

The same hot-rolled and spheroidised 52100 steel (table 3.1) was cut using an electrical discharge machine into thin rectangular samples 40 mm long, 12 mm wide, and 2 mm thick for the hydrogen thermal desorption spectroscopy tests, into thin squares 20 mm a side and

2 mm thick for measuring hydrogen permeation, and into rods 120 mm long and 9.53 mm in diameter for rolling contact fatigue testing.

5.2.2 Heat treatments

Two different processes were applied to the samples, the standard heat treatment for 52100 steel and the extensive martensite-plate cracking treatment described in chapter 3. The former consists of austenitisation at 1113 K (840 °C) for 20 min followed by quenching in oil at room temperature and then tempering at 433 K (160 °C) for 2 h. It is worth remembering that some of the cementite does not dissolve during this austenitisation treatment, so spheroidal (up to 2 μm in diameter), proeutectoid particles are inherited in the final structure that also contains much finer carbides resulting from the tempering of martensite.

To produce samples in which the martensite plates are microscopically cracked, the thin samples were austenitised at 1313 K (1040 °C) for 30 min (90 min for the rod samples), cooled in air for 50 s, quenched in oil at room temperature, and tempered at 433 K (160 °C) for 2 h [87]. The higher austenitisation temperature dissolves all the cementite so the only carbides that are in the microstructure are those resulting from the tempering treatment [49].

5.2.3 Specimen preparation

After heat treatment, the thermal desorption samples were ground with 800 grit sandpaper to achieve the required finish, whilst the permeation samples were ground down to ∼0.5 mm in thickness using a Struers AbraPlan-20 automatic rock grinding machine and then manually ground with 1200 grit sandpaper for the desired surface roughness. A few samples were then prepared for metallographic examination using an optical microscope to confirm the desired microstructure and a good density of cracks were formed.

5.2.4 Thermal Desorption Spectroscopy (TDS)

A thermal desorption spectroscope can measure the hydrogen desorption rate when a hydrogen containing sample is heated inside a pyroprobe unit (induction furnace). As the temperature of the sample raises and gases such as hydrogen get released from traps with increasingly higher binding energies, a carrier gas like helium conducts the desorbed gases to a gas chromatography (GC) unit where they get separated in a column according to their molecular weight and reactivity with the porous material coating the inside of the column. Since the total amount of gases released from the sample is small, a valve collects gases for

a fixed interval and injects them (0.5 ml at a time) to the GC unit to be analysed in 3 min until the next injection takes place. After the column separates the gases, a pulse discharge detector ionises them with photons produced from the dissociation of diatomic helium. Ionisation releases electrons, which are collected by electrodes and converted into a signal that allows plotting counts against time. The area under the peaks is then integrated to estimate the amount of hydrogen released against temperature. Before the analysis, the machine is calibrated by measuring the hydrogen content of a gas with known composition [171, 172].

Due to the difference in heat treatments, the integral (crack-free) and cracked specimens have different grain sizes, carbide volume fraction, and in particular retained austenite, which might make the study of the role of cracks as trapping sites uncertain. Since the binding energy of cementite is smaller than that of dislocations or grain boundaries and is approximately an order of magnitude lower than that of cracks [59, 173, 174], the focus of the experiment design was to separate the role of retained austenite content due to the large difference in hydrogen diffusivity between ferrite and austenite.

Three different thermal desorption experiments were designed:

1. **Partially charged samples:** 7 h hydrogen charging, desorption measurement during ramped heating at $100\,\mathrm{K\,h^{-1}}$ ($100\,^{\circ}\mathrm{C\,h^{-1}}$) until 673 K (400 °C), hydrogen recharging for another 7 h and a second ramped heating desorption measurement at the same heating rate to compare the influence of cracks after retained austenite decomposition.

2. **Isothermal experiments:** 7 h hydrogen charging and desorption measurement during isothermal heat-treatment at 363 K (90 °C) for 4 h as an alternative method to evaluate hydrogen trapping by cracks.

3. **Prolonged charging experiments:** 120 h hydrogen charging and desorption measurement during ramped heating at $100\,\mathrm{K\,h^{-1}}$ ($100\,^{\circ}\mathrm{C\,h^{-1}}$) until 673 K (400 °C) (no recharging) to study a greater level of saturation in the samples, which would tend to reduce the significance of traps in thermal desorption experiments as hydrogen diffusing through the sample would not be attracted into saturated traps. This condition can provide a better indication of the consequences of local equilibrium between ferrite and austenite.

The seven hour charging time is to ensure that samples are not saturated meaning that the hydrogen concentration in spatially non-uniform due to the diffusion front not reaching the centre of the sample. Therefore, if strong traps exist, the amount of hydrogen released during thermal desorption would be limited when compared with a sample without the cracks.

The temperature readings of the furnaces were calibrated with the actual specimen temperature by welding a thermocouple to each sample.

Initially, all of the samples were electrochemically charged with hydrogen using a 3% NaCl + 0.3% NH_4SCN solution and a current density of $1\,A\,m^{-2}$. The charging current was calculated by considering only the area of the top and bottom surfaces of the samples and not the sides, given their low thickness. For samples with ramped heating, TDS testing started 45 min after charging and for the isothermal desorption, only 20 min after in order to allow the readily diffusible hydrogen to leave the sample and for the TDS machine to purge out the air introduced in the system when the sample is placed in the tube furnace. Using an Agilent Technologies 7890A gas chromatography system coupled to an EPKRO-12K Isuzu tubular furnace and a Seahwa SERO2000-1CH flow regulator, hydrogen desorption data were collected every 3 min from which the hydrogen content was calculated as the area under the curve divided by the heating rate, and the desorption rate as the evolved hydrogen per minute. Helium was used as the carrier gas and a standard mixture of He + 60 ppmv H_2 was used for calibration.

5.2.5 Retained austenite

In order to investigate the volume fraction of retained austenite before and after TDS heating to 673 K (400 °C), XRD spectra were collected using the same diffractometer and parameters described in section 4.2.3. The volume fractions of martensite and austenite were obtained using the Rietveld refinement in HighScore Plus as described before.

The onset of retained austenite decomposition was investigated prior to TDS analysis by heating up separate un-cracked and cracked samples in a Theta Industries Dilatronic III using a heating rate of $100\,K\,h^{-1}$ ($100\,^{\circ}C\,h^{-1}$) up to 723 K (450 °C) and quenching at $50\,K\,s^{-1}$ ($50\,^{\circ}C\,s^{-1}$).

5.2.6 Electrochemical Hydrogen Permeation

An electrochemical hydrogen permeation test allows to obtain values of diffusivity, permeability, and apparent solubility of hydrogen in a material, such as steel, by placing a sample between the two compartments of an electrolytic cell. Hydrogen is then absorbed to an entry surface of the sample, which is in contact with the cathodic side of the cell, by galvanostatically polarising it with a constant charging current density. The hydrogen then moves through the thickness of the sample and gets desorbed from an exit surface inside the anodic

side of the cell where a constant potential is applied to oxidise the hydrogen atoms. The anodic current density can be measured as a function of time, which allows the determination of the steady state flux of hydrogen or permeation flux through the sample [175].

Using a Devanathan and Stachurski cell, hydrogen permeation tests at room temperature were conducted according to ISO 17081-2004 standard [176, 177]. After cleaning the samples in hydrochloric acid, a Pd film was deposited electrochemically by submerging one side of the sample in a solution of 2.54 g of $PdCl_2$ in 500 ml of 28% aqueous ammonia and applying for 2 min a current density of 2.83 mA cm^{-2}. This coating is performed to increase the efficiency of the hydrogen oxidation reaction at the hydrogen detection side. The detection side was then filled with a 0.1 M NaOH solution at a constant potential of 250 mV. Once a a steady state current below 3 μA cm^{-2} was reached, the hydrogen charging side of the cell was filled with a 3% NaCl + 0.3% NH_4SCN solution and a density current of 1.5 mA cm^{-2} was applied. The hydrogen oxidation current was measured as a function of time and the effective diffusivity, permeability, and apparent solubility were calculated as described in [178].

5.2.7 Rolling contact fatigue

After heat treatment, the martensite plate cracked rod sample was charged with hydrogen using the same solution and current density described before, but only for 1 h to allow hydrogen to penetrate only to the region of maximum subsurface shear stresses. This procedure was followed in order to establish if the hydrogen trapping by cracks would lead to embrittlement at the crack tips that would lead to early failure of the specimens, for which complete saturation is not necessary as the maximum subsurface shear stresses are no deeper then 250 μm deep below the surface [179]. RCF testing started 30 min after hydrogen charging given the complicated sample loading process and ran for 314 h or 1.62×10^8 cycles. The specimen did not fail but was intentionally stopped due to machine scheduling limitations. The sample was then cut as described in section 4.2.3, and observed under the optical microscope and SEM after polishing and etching with nital.

5.3 Results and discussion

5.3.1 Basic characterisation

Optical microscopy after the heat treatment for the cracked samples confirmed the expected distribution of martensite-plate cracks [87], as shown in fig. 5.1a.

The XRD spectra of the cracked and un-cracked specimens before and after 120 h charging and TDS testing up to 673 K (400 °C) are presented in fig. 5.1b. The difference in austenitisation temperatures led to corresponding differences in the retained austenite content of 0.05±0.01 for the integral (no cracks) sample and 0.12±0.01 for the cracked one. However, the retained austenite in both samples decomposed on heating to 673 K (400 °C) during TDS. This was confirmed using dilatometry (fig. 5.1c). For both samples, the onset of retained austenite decomposition is at ∼548 K (275 °C).

The hardness values of the samples before and after TDS testing are presented in table 5.1.

Table 5.1 Vickers hardness for the cracked and un-cracked samples used in each of the three TDS experiments. The average value and standard error of the mean were calculated based on ten indentations per sample.

Experiment	Partially charged		Isothermal heating		Prolonged charging	
	No cracks	With cracks	No cracks	With cracks	No cracks	With cracks
Before run 1	737±3 HV30	751±4 HV30	785±2 HV30	754±3 HV30	758±2 HV30	780±1 HV30
After run 1	495±3 HV20	490±5 HV20	785±1 HV30	754±2 HV30	505±1 HV20	546±3 HV30
After run 2	493±1 HV20	489±3 HV20	-	-	-	-

5.3.2 Thermal Desorption Spectroscopy (TDS)

The desorption curves for each of the three TDS experiments on partially charged samples are presented in fig. 5.2, together with an indication of the total amount of hydrogen desorbed.

Focusing first on the cracked sample, two desorption peaks were observed, the one beyond 523 K (250 °C) being attributed to hydrogen released when retained austenite decomposes is consistent with the dilatometric and X-ray data, and with the fact that the higher-temperature peak disappears when the sample already subjected to TDS up to 673 K (400 °C) is recharged with hydrogen and once again studied using thermal desorption spectroscopy. Furthermore, the second peak is only perceptible in the cracked sample that has a much larger retained austenite content. It is also worth noting that the hardness of the sample does not change at all within the limits of scatter, when subjected to the second TDS experiment (table 5.1).

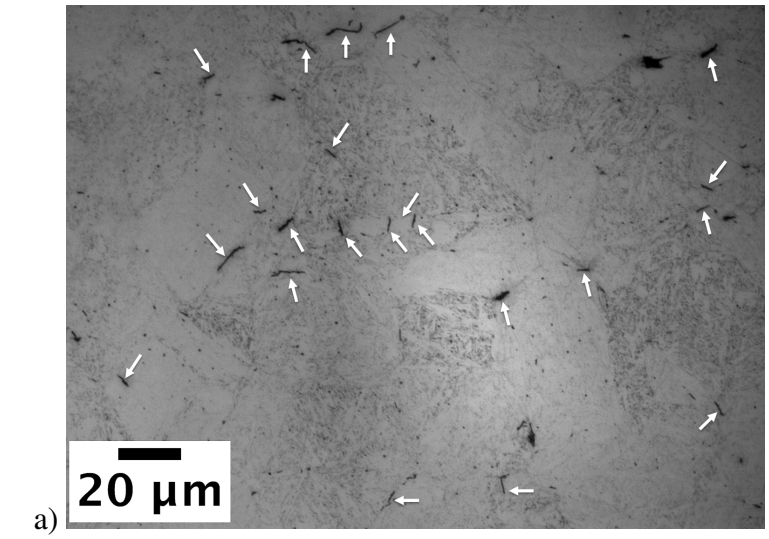

a)

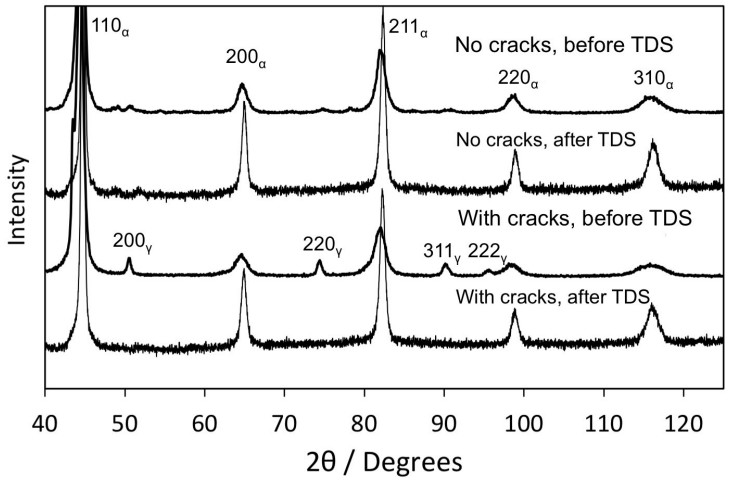

b)

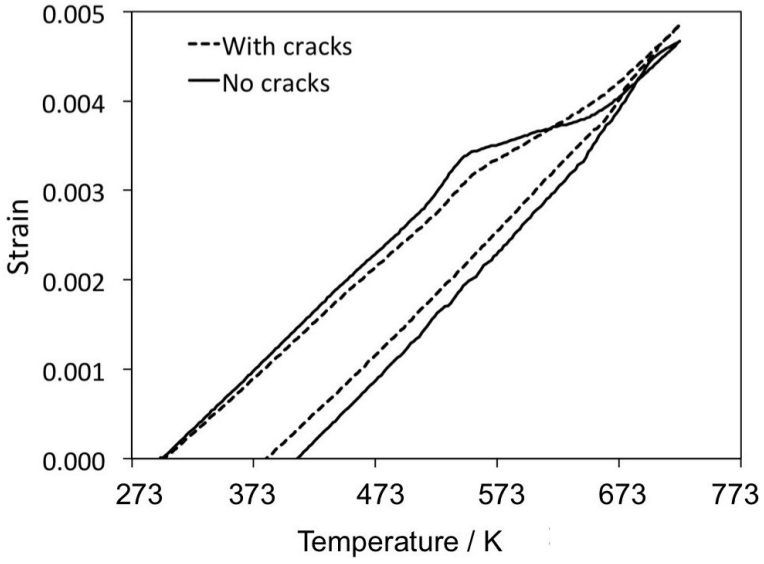

c)

Fig. 5.1 a) Optical metallography of cracked sample prior to TDS testing, b) X-ray diffraction data for retained austenite determination, and c) dilatation curve for the cracked and un-cracked samples using the same heating rate as the first TDS experiment, $100\,\mathrm{K\,h^{-1}}$ ($100\,^{\circ}\mathrm{C\,h^{-1}}$).

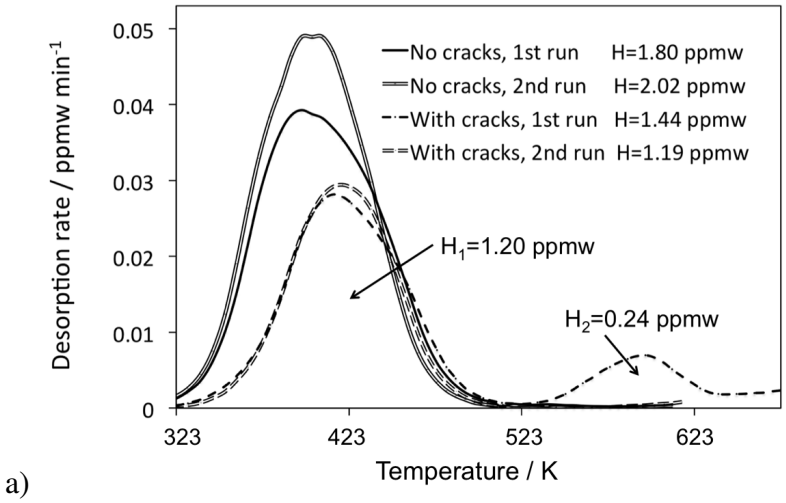

a)

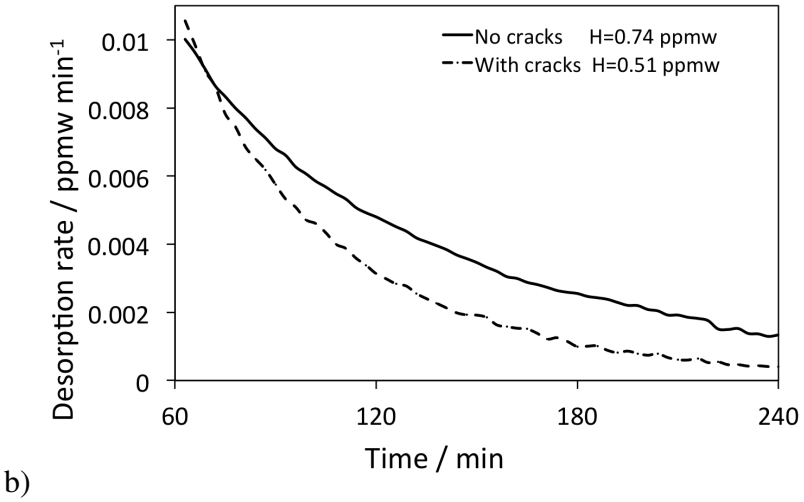

b)

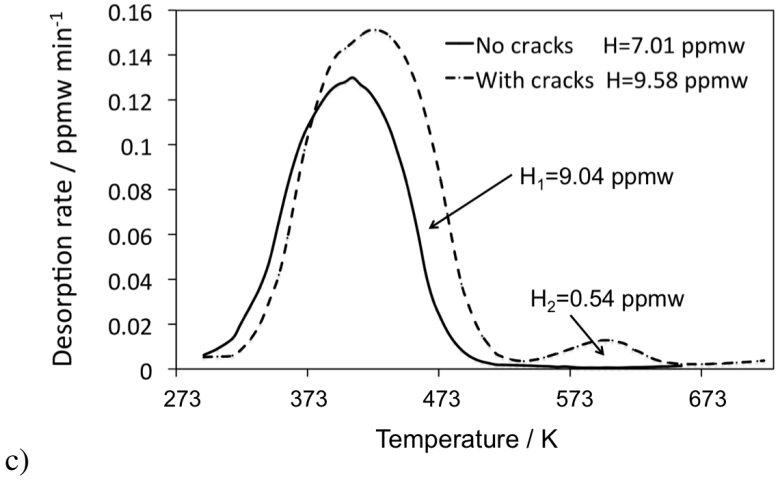

c)

Fig. 5.2 a) Experiment 1: Desorption during ramped heating at 100 K h^{-1} (100 °C h^{-1}) after 7 h charging (recharged once), b) Experiment 2: Isothermal desorption at 363 K (90 °C) for 4 h after 7 h hydrogen charging (no recharging), c) Experiment 3: Desorption during ramped heating at 100 K h^{-1} (100 °C h^{-1}) after 120 h charging, (no recharging).

It is noteworthy the un-cracked samples release more hydrogen during TDS than those containing cracks (fig. 5.2a), consistent with the hypothesis that in the latter case, some of the charged hydrogen will become strongly trapped. For the same reason, there is less readily diffusible hydrogen evolved below 423 K (150 °C) from the cracked sample, resulting is a smaller TDS peak that is in effect shifted to a greater temperature. Retained austenite is not responsible for the relatively small TDS peak of the cracked sample in the temperature range below 523 K (250 °C) because that peak does not change when the austenite is absent in the *recharged* sample.

The isothermal experiments performed at 363 K (90 °C) and illustrated in fig. 5.2b confirm the interpretations above. The evolved hydrogen is about 31% less for the cracked sample.

The data for the samples that underwent prolonged charging for 120 h are particularly revealing about the role of austenite (fig. 5.2c). The general features of the TDS curves are similar to those of samples that were charged for only 7 h, with the cracked sample exhibiting the second desorption peak associated with the decomposition of austenite. However, there are detailed differences that arise from the fact that austenite and ferrite are in local equilibrium prior to the decomposition of austenite. The concentrations ($c = x/V$) associated with the first and second peaks, where x is the amount of hydrogen evolved over the temperature range of each peak, and V is the fraction of the phase with which that peak is associated are listed in table 5.2. When austenite is in equilibrium with ferrite, it has a much greater solubility[1] for hydrogen since hydrogen occupies the octahedral interstices of austenite and its dissolution energy is smaller than in ferrite [180, 181]. However, during the desorption of hydrogen as the sample is heated, hydrogen in the ferrite escapes into the surrounding environment, and the austenite acts as a source for more hydrogen since equilibrium is maintained at the α/γ interface. This process does not require the decomposition of that austenite so the hydrogen released in the second peak beyond 523 K (250 °C) is simply a reflection of the *remaining* quantity in the γ just before its decomposition. This explains several observations:

(a) A second peak is not observed in the sample with $V_\gamma = 0.05$ (un-cracked) because the austenite is essentially exhausted by the time the temperature reaches 523 K (250 °C).

[1] Solubility can only be defined when referring to two phases, for example, the solubility of carbon in ferrite in equilibrium with cementite is different from ferrite in equilibrium with austenite.

(b) Considering the samples that were charged for 120 h, contrary to expectations of a greater solubility in γ, the concentration $c_\gamma \ll c_\alpha$, because the austenite releases hydrogen into the ferrite during heating as the concentration in the latter phase decreases by escape into the environment.

(c) The concentration c_α in the samples charged for 120 h is greater in the cracked than un-cracked samples. This is because the cracked sample has a reservoir of hydrogen in the 0.12 volume fraction of retained austenite, that released hydrogen into the surrounding ferrite during heating.

(d) The actual amount of hydrogen in austenite of the 120 h specimen immediately after charging and before heating, must have been much larger than indicated by the second peak (c_γ). The lower limit of this concentration, c_γ^0 can be estimated by comparing the two curves below 523 K (250 °C) in fig. 5.2c. The two samples have a difference in retained austenite fraction of $0.12 - 0.05 = 0.07$, and the difference in the hydrogen released is $9.04 - 7.01 = 2.03$ ppmw. If this difference is purely due to the hydrogen released by austenite into ferrite during heating, then the total concentration is given by $c_\gamma^0 = (2.03/0.07) + (0.54/0.12) = 33.5$ ppmw. This is a much larger concentration than the c_α values listed in table 5.2, as might be expected from the relative solubilities of hydrogen in austenite and ferrite.

Table 5.2 Concentrations associated with the TDS experiments as described in the text. The accuracy of determining x_α and x_γ is approximately 0.01 ppmw [182]. The uncertainty of V_γ is 0.01 as described in section 5.3.1.

	V_γ	x_γ / ppmw	x_α / ppmw	c_γ / ppmw	c_α / ppmw
Cracked, partially charged	0.12	0.24	1.20	2.00±0.03	1.34±0.02
Cracked, prolonged charging	0.12	0.54	9.04	4.50±0.06	10.27±0.11
Un-cracked, partially charged	0.05	0	1.8	0±0.01	1.90±0.03
Un-cracked, prolonged charging	0.05	0	7.01	0±0.01	7.37±0.08

5.3.3 Hydrogen Permeation

We were not able, for practical reasons, to implement sufficient experiments to obtain conclusive results that separate out the effects of retained austenite and cracks. Both of these factors would reduce the effective diffusivity of hydrogen because the diffusivity in austenite is much smaller than in ferrite, and cracks are such strong traps that they would also

hinder the passage of hydrogen through the steel. An ameliorating factor is that the retained austenite in both samples is not in the form of films that percolate through the microstructure [183], but mostly present as blocks about 3 µm in size. Consistent with [183], such austenite would not form continuous barriers to the path of hydrogen, so it might be speculated that the role of the austenite can be neglected.

The hydrogen permeation curves for each of the two samples are presented in fig. 5.3. Using these data as well as the sample thickness L, the break-through time t_b, and steady-state current density I_{ss}, the values of the effective hydrogen diffusivity D_{eff}, permeation P, and apparent hydrogen solubility C_{app} were calculated using the break-through method in reference to the ISO17081 standard (table 5.3). Both the effective diffusivity and permeability values are much greater in the case of the un-cracked samples, potentially suggesting the role of the cracks in trapping the hydrogen as it attempts to pass through the steel.

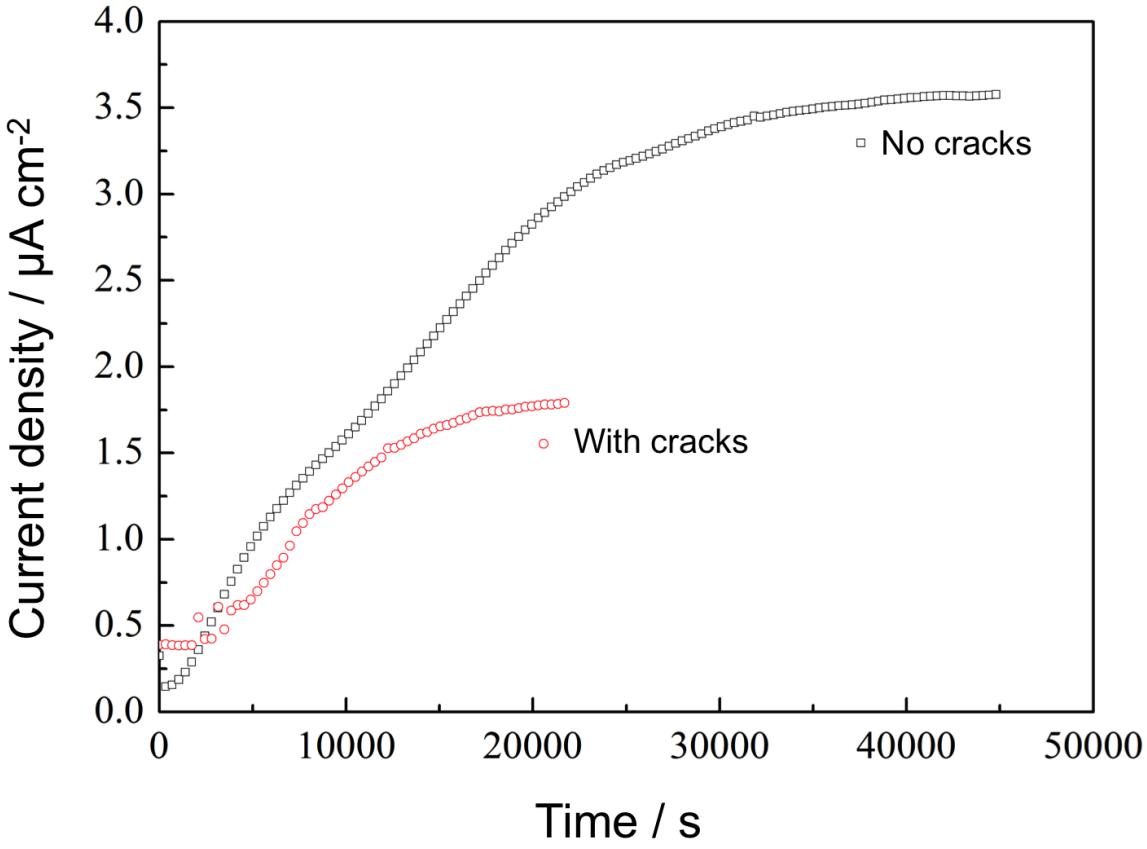

Fig. 5.3 Hydrogen permeation curves for cracked and un-cracked samples.

Table 5.3 Parameters determined through the hydrogen permeation test. The uncertainty of the sample thickness is ±2% and that of the diffusivity, permeation, and solubility is ±4%.

Parameters	No cracks	With cracks
L / m	0.00058	0.00062
t_b / s	420	1600
I_{ss} / A m^{-2}	0.0358	0.0179
D_{eff} / m^2 s^{-1}	5.235×10^{-11}	1.57×10^{-11}
P / mol m^{-1} s^{-1}	2.15×10^{-10}	1.15×10^{-10}
C_{app} / mol m^{-3}	4.11	7.32

5.4 Rolling Contact Fatigue

The results of microscopical examination of the hydrogen charged and RCF tested sample are displayed in fig. 5.4. The typical microstructure of the edge of the circumferential cross section sample is shown in fig. 5.4b, where it can be seen that hydrogen trapped at cracks did not accelerate crack propagation, as they display the previously mentioned signs of damage deflection via crack branching of non-hydrogen charged samples. By observing the inclusions such as the one marked by the white arrow, which is 77 µm deep (22 µm shallower than the maximum orthogonal shear stress) it can be seen that hydrogen did not accelerate the formation of white-etching matter either. In fact, the small cracks to the sides of the inclusion correspond to very early stages of butterfly formation despite the running time of 314 h at 3.5 GPa of contact pressure confirming the successful hydrogen trapping ability of cracks. In comparison, the two cracked martensite plates of fig. 5.4a, one with three cracks and the longer one with five cracks show no branching and the inclusions marked by white arrows at the bottom of the image show no decohesion with the matrix, which is expected from a region away from large subsurface shear stresses and the hydrogen diffusion front. Although it is not possible to categorically conclude that hydrogen would not lead to an acceleration of white-etching matter formation and crack propagation when trapped at martensite plate cracks from a single test ran for a shorter time than the non-hydrogen charged sample, it is worth noting that any signs of hydrogen embrittlement would only show while the hydrogen is mobile. After the trapping of some of the hydrogen by cracks and the room temperature desorption of the lattice hydrogen left, the damage mechanisms should be the same as those of the uncharged sample, making very long running RCF testing times unnecessary.

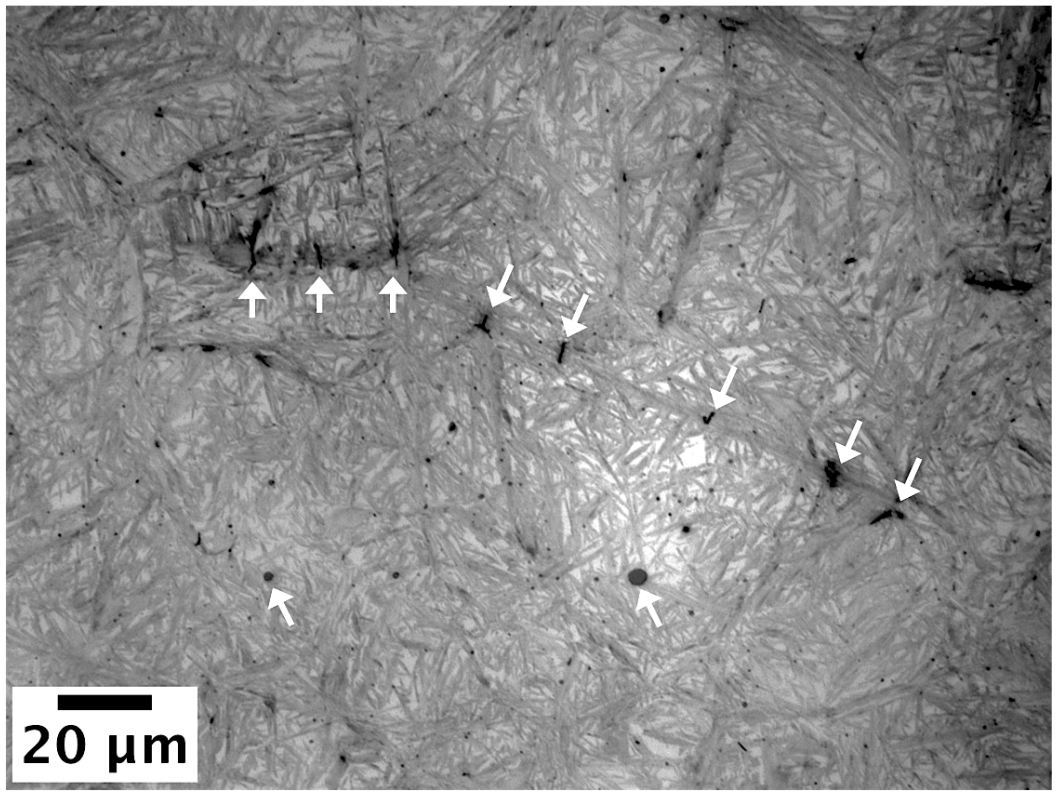

a)

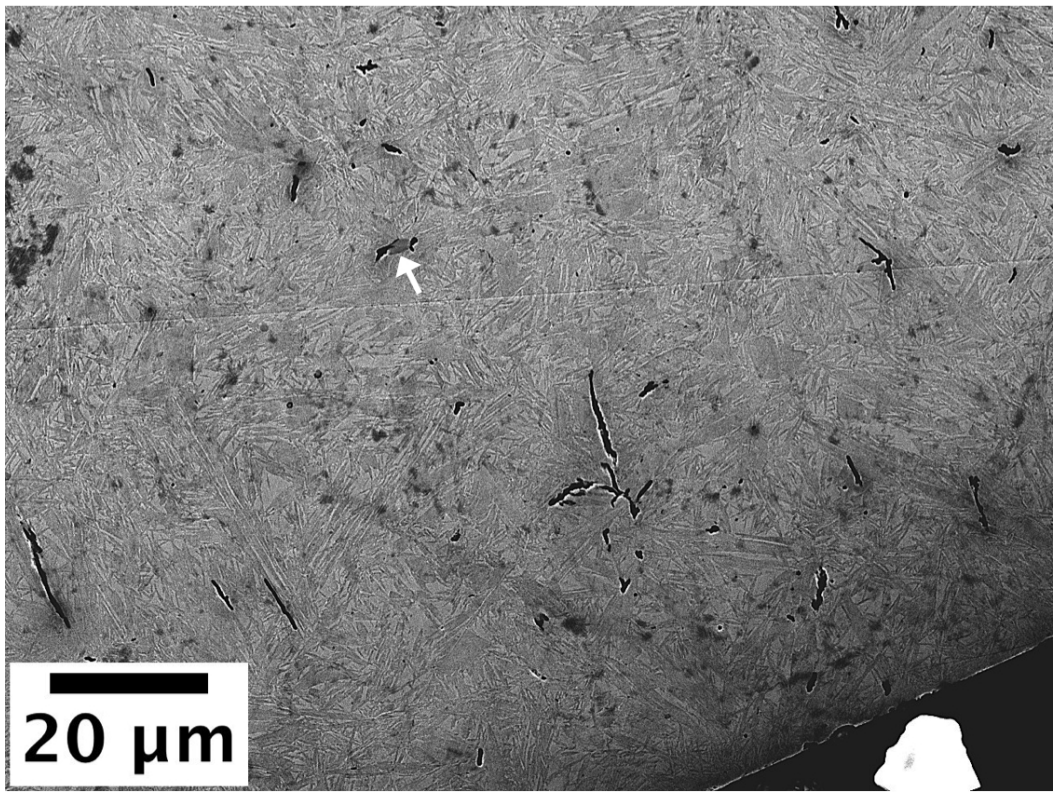

b)

Fig. 5.4 Martensite plate cracked sample after hydrogen charging and rolling contact fatigue testing for 314 h (1.62×10^8 cycles) showing in: a) the centre of the sample under OM and b) the edge of the sample under SEM.

5.4.1 Model

The purpose of the work presented here was to study primarily the influence of cracks on the thermal desorption curves in order to gain more confidence in the interpretation of experimental data. The effect of hydrogen trapping at cracks during TDS experiments was simulated by adapting one of the hydrogen desorption models developed by Song et al. to include a fine dispersion of microcracks in a ferritic matrix, These cracks were modelled as surface disconnections within the matrix making them behave in a similar way to voids [184]. A key aspect of this model is that it permits multiple traps to be included in the analysis whereas none of the existing analytical methods can deal with more than one type of trap. As will be seen, a certain amount of calibration is needed to assign trap number-densities, and this was done on the basis of data collected for the samples without cracks.

In the model, the consequence of the initial charging stage is to distribute the hydrogen across the lattice and trapping sites assuming local equilibrium. The diffusion is assumed to be parallel to the thickness direction, while the hydrogen interacts with multiple kinds of traps of different binding energies: grain boundaries, dislocations, and microcracks. A more detailed explanation of the theory behind the numerical model and the consequences of different dislocation densities in hydrogen trapping can be found in [184].

The binding energies and densities of trapping sites by interfaces and dislocations were obtained from the previous study by Song et al. [184]. The reported binding energies were 49 and 44 $\mathrm{kJ\,mol^{-1}}$ for grain boundaries and dislocations, respectively. However, in those experiments the sample temperature was assumed to be that of the furnace rather than measuring the sample temperature directly, which was $\sim$20-30 °C higher in the 100-200 °C range. Therefore, the temperature calibration described in section 5.2.4 was used to correct these values to 50 and 47 $\mathrm{kJ\,mol^{-1}}$ respectively, with an uncertainty of $\pm 2\,\mathrm{kJ\,mol^{-1}}$. The density N_t^{ρ} of trapping sites due to dislocations was calculated using equation 15 in [184]:

$$N_t^{\rho} = 12\pi b^2 \rho / \Omega \tag{5.1}$$

where b is the magnitude of the Burgers vector, $\rho = 10^{13}\,\mathrm{m^{-2}}$ is the dislocation density equal for both cracked and integral samples [185], Ω is the atomic volume of iron, yielding $N_t^{\rho} = 6.73 \times 10^{23}\,\mathrm{m^{-3}}$. The density of trapping sites due to interfaces, $N_t^{gb} = 1.65 \times 10^{25}\,\mathrm{m^{-3}}$, was obtained by fitting the numerical model to the TDS curves for the recharged un-cracked samples that did not contain any retained austenite but maintained their hardness after the first TDS run. It is worth mentioning that the value of diffusivity used in the model is not the

one derived from the hydrogen permeation tests, affected by defects such as cracks and retained austenite, but the standard value of hydrogen diffusing through a ferritic lattice [186].

The crack number-density N_V^c=4.1×10^{14} m^{-3} was obtained by measuring 700 cracks using metallography and assuming that the crack depth was equal to the average length. The trapping site density on the crack faces was calculated as the number of iron atoms on each of the two faces of the cracks present, per unit volume of steel. This assumed circular martensite discs of mean linear intercept $\overline{L} = 45\,\mu$m [87] and 2.25 μm in thickness (c/a aspect ratio of 0.05 [187]) knowing that there is an equivalent of 1/2 iron atom at the face of the BCC lattice. By fitting the data to the simulated curves it was possible to determine the amount of hydrogen atoms that get trapped per iron atom of the cracked surfaces.

This model allowed the simulation of the desorption of hydrogen from various kinds of traps in a purely ferritic matrix, limiting the analysis to the TDS curves of the un-cracked and cracked samples, after partially charging with hydrogen for the second time, which contained virtually no retained austenite. The closest fit to the data under the assumptions of unidirectional hydrogen flow, local equilibrium, and the three kinds of traps used (not considering trapping at cementite) is presented in fig. 5.5a.

By modelling the peak of the recharged cracked and integral samples in the partially charged experiment it was found that the closest fit to the data was achieved for a crack binding energy of above 200 kJ mol^{-1} assuming one hydrogen ion gets trapped by each iron atom. In fact, increasing the value up to 500 kJ mol^{-1} made no changes in the height or shape of the peak since all these values represent already irreversible trapping sites (fig. 5.5b). Since it was considered in this model that hydrogen absorbed by cracks becomes molecular inside them, the binding energy is linked to the bond dissociation energy of hydrogen, 458 kJ mol^{-1} [188], and not to that of free surfaces, 70-95 kJ mol^{-1} [189].

By taking a binding energy above 200 kJ mol^{-1}, the trapping site density of cracks was then varied to find the best fit at N_t^c=41×10^{23} m^{-3}, which is approximately eight times the amount of iron atoms calculated to be at the surfaces of cracks present per unit volume of steel (N_{Fe}^c=5.1×10^{23} m^{-3}). In other words, approximately eight hydrogen ions are actually trapped at each iron atom found at the crack surfaces, meaning that there are at least $\sim 9.95 \times 10^9$ trapping sites per crack. It is expected that once the hydrogen ions get trapped at the crack surfaces, hydrogen combines to form molecular hydrogen which fills up the volume of the crack. This means that although hydrogen adapts its molecular state

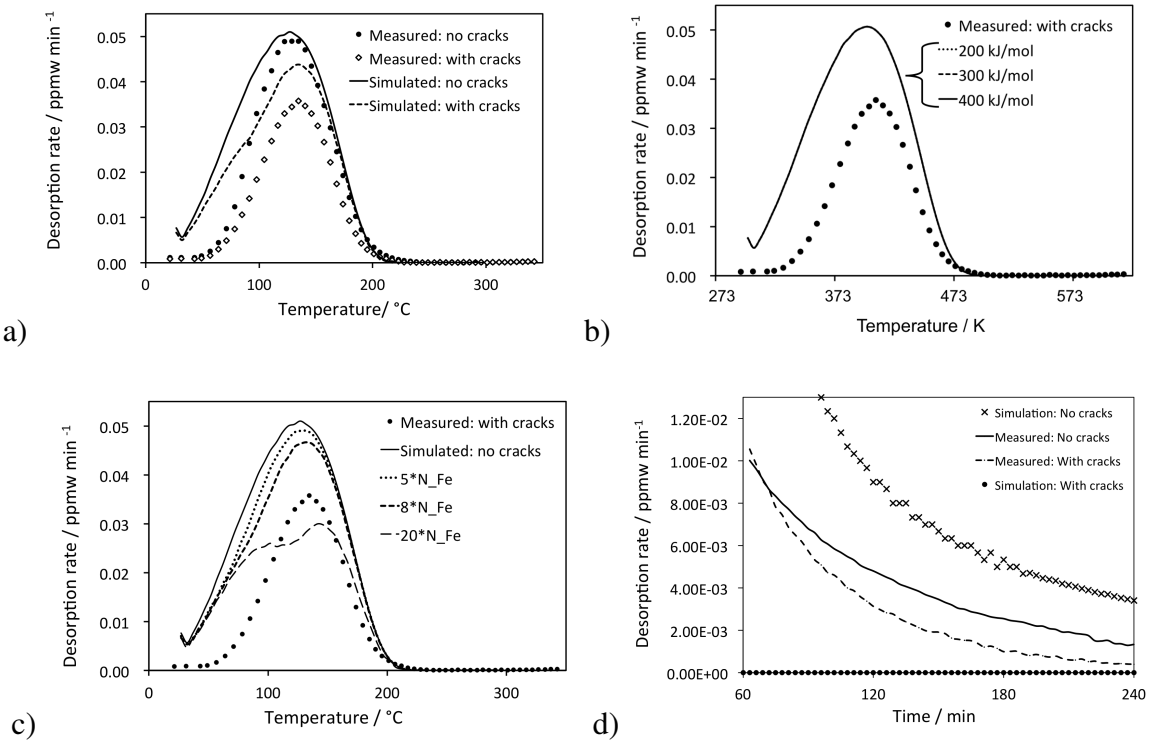

Fig. 5.5 a) Comparison between experimental and simulated hydrogen desorption curves for cracked and integral samples (second run, partial charging), b) variation of the binding energy to fit the peak of the cracked sample after partial recharging, whilst having a constant trap density of N_{Fe}^{c}=5.1×10^{23} m^{-3} (one hydrogen ion per iron atom), c) variation of the trapping site density of cracks as a multiple of the number of iron atoms at the surface of cracks present in unit volume of steel, N_{Fe}^{c}, and d) comparison between experimental and simulated hydrogen desorption curves for cracked and integral samples containing retained austenite during isothermal heating.

which is not pernicious, desorption of it would require complete meltdown of the sample [4]. Trapping of hydrogen by cracks will saturate when the volume of the crack has been filled by molecular hydrogen which could potentially create a internal pressure that would promote crack propagation. However, this internal pressure could be beneficial in avoiding the crack surfaces to rub against each other under rolling contact fatigue, which has been suggested to be the cause to “white-etching matter" formation [179]. In other words, the presence of cracks in the bulk would not only render pernicious hydrogen immobile and not damaging, but could also limit it from fostering microstructural degradation in the form of white-etching matter.

As shown in fig. 5.5c, increasing the trapping site density of cracks as a multiple of N_{Fe}^{c} decreases the height of the peak up to a maximum of $\sim 8N_{Fe}^{c}$ after which the peak splits in two due to incomplete saturation at the middle of the sample that alters the diffusion distance of hydrogen. This is shown in fig. 5.6 where the hydrogen profile after charging, room temperature aging, and heating are plotted for the case of N_{t}^{c}=$8N_{Fe}^{c}$ and $20N_{Fe}^{c}$. In fig. 5.6b, 5.6d and 5.6f, it can be seen that in the case of the partially charged samples, hydrogen diffuses not only out through the surface, but also towards the middle of the sample after charging and before heating. Despite hydrogen diffusing inwards, the centre of the sample still remains unsaturated. After heating, there is hydrogen in the centre (fig. 5.6f), unlike the previous graph (fig. 5.6d), trapped at cracks due to their strong binding energy. Since the depth of penetration of trapped hydrogen increased, the effective diffusion distance is longer than the sample thickness for the hydrogen that diffused into the sample after charging causing the desorption peak to split.

In an attempt to model the results of the partially charged samples containing retained austenite of the isothermal heating experiment (fig. 5.5d), it was found that in the un-cracked case, the simulation over-predicted the amount of hydrogen desorbed although the trend of desorption was accurate. This is due to the difference in absorbed hydrogen and effective diffusivity, knowing that the model only accounts for ferrite. However, the important part to note is that for both experimental observations and simulations, cracks have the ability to re-trap hydrogen freed from reversible traps. In the case of the cracked sample, there was no desorption since the cracks were partially charged (unsaturated) from the beginning and in fact kept trapping the hydrogen freed from low binding energy traps at 363 K (90 °C). Desorption would only occur until all the cracks are saturated. The measured cracked sample does show hydrogen desorption since the real distribution of cracks is less homogenous than the one assumed in the model so it is unlikely freed hydrogen will always meet a crack,

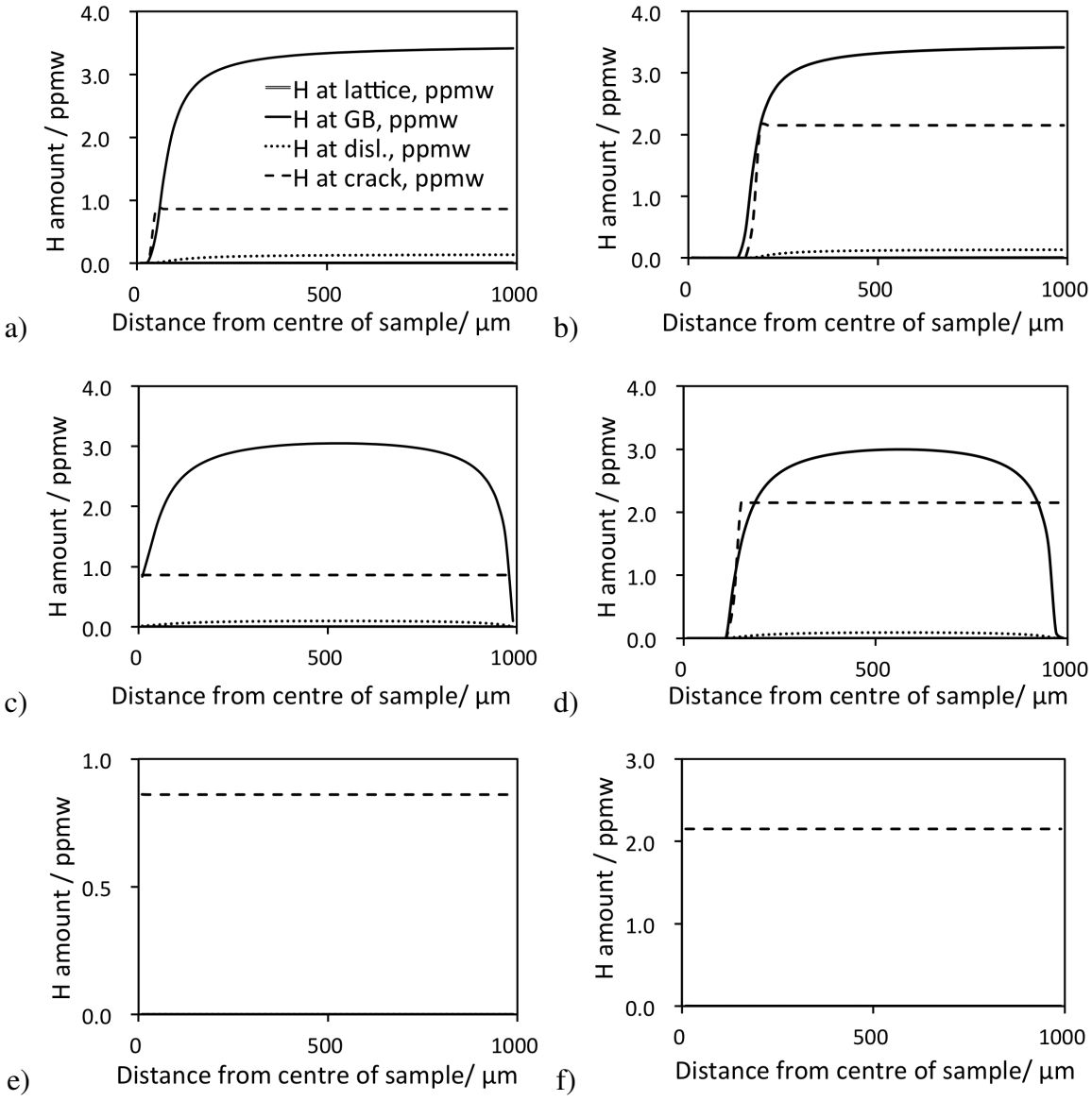

Fig. 5.6 Hydrogen profiles in the modelled sample for $8N_{Fe}^{c}$ in the left column and $20N_{Fe}^{c}$ in the right column, where a) and b) represent the hydrogen present after charging, c) and d) the hydrogen after room temperature ageing, and e) and f) the hydrogen after heating trapped at lattice, grain boundaries (GB), dislocations, and cracks. The x-axis represents the centre of the sample (0 µm) and the surface (1000 µm), showing in b) and d) how an increased trap density leaves the centre of the specimen uncharged.

and be re-trapped, as it effuses out.

5.5 Conclusions

The following conclusions can be reached from the present work, based on critical experiments using thermal desorption spectroscopy and electrochemical hydrogen permeation of 52100 bearing steel samples heat treated according to the standard procedure and through a process to develop microcracks, as well as on the model developed to describe and predict the results obtained:

- Martensite plate cracks or microcracks act as irreversible traps for diffusible hydrogen in 52100 steel. When absorbed by cracks, hydrogen ions will become molecular and lose their damaging character. If not saturated, these cracks can also retrap hydrogen freed from reversible, low-binding energy traps such as dislocations or grain boundaries.

- As confirmed by XRD and dilatometry, partially charged and supersaturated hydrogen samples containing around 0.12 volume fraction of retained austenite showed a second peak in ramped heating TDS experiments corresponding to the hydrogen desorption caused by retained austenite decomposition at $\sim$548 K (275 °C). The samples heat treated according to the standard procedure containing around 0.5 volume fraction of austenite after tempering did not show such second peak.

- Through electrochemical permeation tests, the effective hydrogen diffusivity D_{eff} was found to be 5.235×10^{-11} m^2 s^{-1} for the crack-free sample and 1.57×10^{-11} m^2 s^{-1} for the cracked sample. The experiment also allowed to obtain the apparent hydrogen solubility C_{app} which is 4.11 mol m^{-3} for the crack-free sample and 7.32 mol m^{-3} for the one with cracks.

- Hydrogen charging previous to RCF testing showed no acceleration of white-etching matter formation at cracks or inclusions (butterflies) or martensite plate crack propagation via embrittlement at the crack tips confirming the ability of cracks to render hydrogen immobile and non-damaging by turning it into its molecular form inside them.

- A model assuming local equilibrium was able to reproduce the hydrogen desorption behaviour of the integral (crack-free) and cracked samples containing no retained austenite by taking into consideration the effect of multiple binding energy traps such as grain boundaries, dislocations, and cracks.

- The binding energy for cracks was estimated to be of at least 200 kJ mol^{-1}, whereas the density of cracks was measured to be N_V^c=4.1×10^{14} m^{-3}, and the trapping site density generated by cracks N_t^c=41×10^{23} m^{-3}.

Chapter 6

Degradation of nanostructured bainite under rolling contact fatigue

6.1 Introduction

In this chapter, the consequences of rolling contact fatigue on a carbide-free nanostructured bainitic steel intended for bearing applications are presented for the first time in the open literature. Tests performed at various intervals followed by mechanical, microscopical, and crystallographic characterisation lead to the conclusion that the degradation mechanism is ductile void formation at interfaces, followed by growth and coalescence into larger voids that lead to fracture along the direction of the softer phase. This is different from the conventional damage mechanism that involves crack initiation at inclusions and propagation, for example in typical bearings steels such as 52100. The huge density of interfaces in the nanostructure allows the formation of a large dispersion of voids, and ultimately cracks, at depths consistent with the maximum orthogonal shear stress below the contact surface. This study should prove useful for the eventual usage of nanostructured bainitic steels in rolling bearings.

6.2 Experimental Methods

6.2.1 Material and sample preparation

The alloy was produced by Tata Steel UK as an ingot subjected to electroslag remelting, vacuum arc remelting, annealing, cold straightening, smooth turning, and rolling to a shaft 180 mm in diameter with the composition described in table 6.1.

Table 6.1 Chemical composition, wt%, of the steel studied.

C	Mn	S	P	Si	Al	Cu	Cr	Ni	Mo	V	Nb	Ti	B
0.8	2.03	0.006	0.006	1.51	0.057	0.03	0.22	1.05	0.377	0.004	0.007	0.019	0.0007

Long cylindrical samples for rolling contact fatigue testing with a diameter of 9.53 mm and a length of 120 mm were cut out along the longitudinal direction of the shaft using a band saw, turned, ground, and polished to a 1 μm finish.

6.2.2 Heat treatment

Samples were wrapped in four layers of steel foil and austenitised in a box furnace at 1203 K (930 °C) for 30 min, cooled in air to 523 K (250 °C) which took around 6 min, introduced to an oven for isothermal heat treatment at 473 K (200 °C) for 10 days, and cooled in air. In order to corroborate that the heat treatment was successful, one of the samples was cut along the radial cross section and prepared for metallographic characterisation and macrohardness testing with a load of 30 kg and a dwelling time of 5 s.

6.2.3 Rolling contact fatigue testing

Testing of the cylindrical samples was carried out on the Delta Research Corporation BR-4 Ball-Rod Rolling Contact Fatigue machine using the same sequence and parameters described in section 4.2.2.

6.2.4 Characterisation

Surface roughness profile

After extracting the samples from the RCF equipment, the profile of each wear track in the longitudinal direction of the cylindrical test specimens was measured in at least three different positions with the Veeco Dektak 6M Stylus Profiler. The most representative profile per sample is presented in the results.

Microhardness profile

Using a Mitutoyo MVK-H2 machine, the Vickers microhardness profile of the surface up to a depth of ∼1 mm using a load of 1 kg and a dwelling time of 5 s was performed on a

new and a used ball cut in half and on the cylindrical test samples cut along the radial cross section at the centre of the wear track after RCF testing.

Microstructural characterisation

In order to study the structural degradation of nanostructured bainite after RCF, the unetched and etched (2% Nital) microstructure and surface of the balls (used and new) and cylindrical test specimens were characterised using an optical microscope, an Olympus Stereo microscope, and the JEOL JSM 5500LV SEM equipped with an EDS detector. For such characterisation, RCF specimens were cut along the centre of the racetrack in the radial cross section as shown in fig. 4.2. More detailed characterisation of the longest lasting RCF sample was performed by carving out lamellae using a focused ion beam. These lamellae were then observed under the JEOL 200CX TEM using an accelerating voltage of 200 kV.

X-Ray diffraction

The volume fractions of the phases present after heat treatment and after the longest running RCF test were determined using the same diffractometer and parameters described in section 4.2.3. To account for a possible stress-induced transformation of retained austenite into martensite in the sample under RCF, a different Rietveld method analysis in HighScore Plus was followed in comparison with the previous two chapters. In this case, austenite was fitted to three isolated austenite peaks: 002, 022, and 113. The maximum and minimum estimates for the lattice parameter of austenite could be obtained, which were then used to calculate its carbon concentration through the Dyson and Holmes equation [190]. Since this carbon concentration is inherited by the stress-transformed body centred tetragonal BCT martensite, its maximum and minimum values of tetragonality were obtained by referring to the Honda and Nishiyama charts [191]. These lattice parameters (a_γ, $a_{\alpha'}$, and $c_{\alpha'}$) were used to fit martensite, retained austenite, and bainitic ferrite to either the whole spectrum (30-125 °) or a cropped version of it (48-110 °), which eliminated martensite and austenite overlapping peaks (e.g. $110_{\alpha'}$ and 111_γ). Given the importance of phase quantification, an alternative method based on magnetic measurements is presented as an independent study in appendix B with the intention of promoting this technique as an alternative to X-ray diffraction.

6.3 Results and Discussion

6.3.1 Heat treatment

After heat treatment, the sample consisted of a typical structure of fine ferritic plates and intervening austenite films as seen in fig. B.3. The sample had an average hardness and standard error of the mean of 632 ± 2 HV30 corresponding to ten indentations. Quantitative measurements of the phase fractions are presented further on.

6.3.2 Rolling contact fatigue and surface roughness

The results of the RCF tests are listed in table 6.2. The number of cycles is given by the product of the time, revolutions per minute, and a factor of 2.389 (Appendix A). The latter factor comes from the number of stress cycles between balls and specimen for one revolution of the specimen, given that the balls and sample have different diameters [160]. All five samples ran until the accelerometer of the rig automatically stopped the tests when a set threshold level of vibration was exceeded, caused not by the failure of the sample but by unintended failure of the lubrication system. Nevertheless, the times at which these tests were automatically stopped, proved to be very useful in determining the progressive degradation of the nanobainitic structure underneath the contact surface. All samples were characterised except that from test 2 since the number of cycles is similar to sample 3.

By analysing the profile of the contact grooves, two cases were identified: an even distribution of the load with a single wear track (fig. 6.2a and b), and that where two parallel tracks are formed, separated 450 µm in the case of fig. 6.2c and d. In the latter case, the depths of the grooves indicate that the tracks are traversed by either one ball (shallow groove) or two balls, so that the number of cycles experienced will at most be two-thirds of those listed in table 6.2. From the samples with single wear tracks it can be seen that the width of these is $\sim$0.6 mm, which is in agreement with the calculated value of 0.635 mm for the 3D elastic contact thickness presented in table 4.1.

6.3.3 Microhardness

After cutting a new and a used ball of the longest running test, as well as the test samples along the radial cross section at the centre of the deepest wear track, the hardness of the material below the contact surface was characterised, fig. 6.3. The hardness indents, each about 55 µm across the corners, were placed in parallel arrays inclined to the surface in order

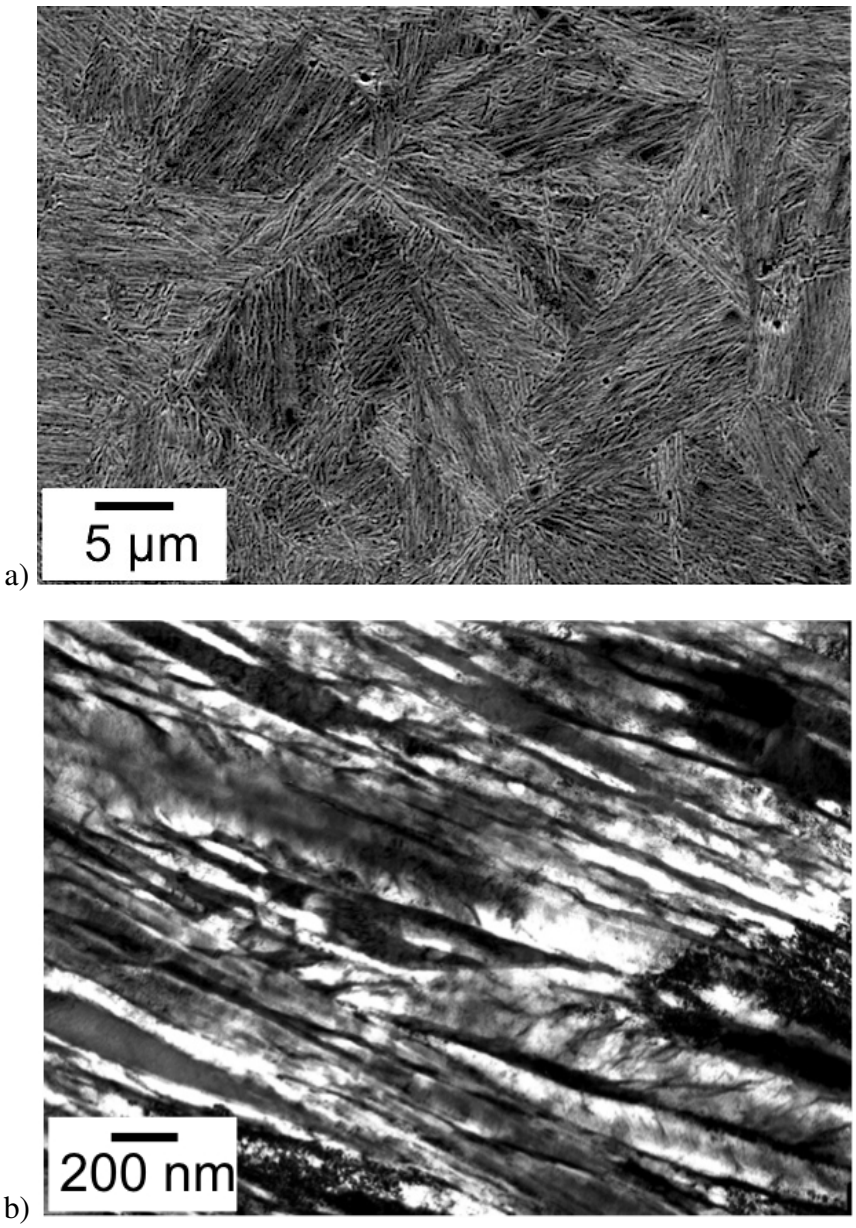

Fig. 6.1 Nanostructured bainite formed after austenitisation at 1203 K (930 °C) for 30 min and isothermal heat treatment at 473 K (200 °C) for 10 days in a) scanning electron micrograph and b) transmission electron micrograph.

Table 6.2 RCF cycles for nanobainitic samples running at room temperature, 3600 rpm, and 3.5 GPa of Hertzian pressure. In the case of the samples identified with a †, one of the balls did not follow the track created by the other two balls, so the deepest groove formed by testing will have experienced two-thirds of the cycles quoted.

Test	Cycles	Time / h
1	2.1×10^7	41
2	1.2×10^8	226
3	1.3×10^8	252
4	2.3×10^8 †	450
5	4.9×10^8 †	948

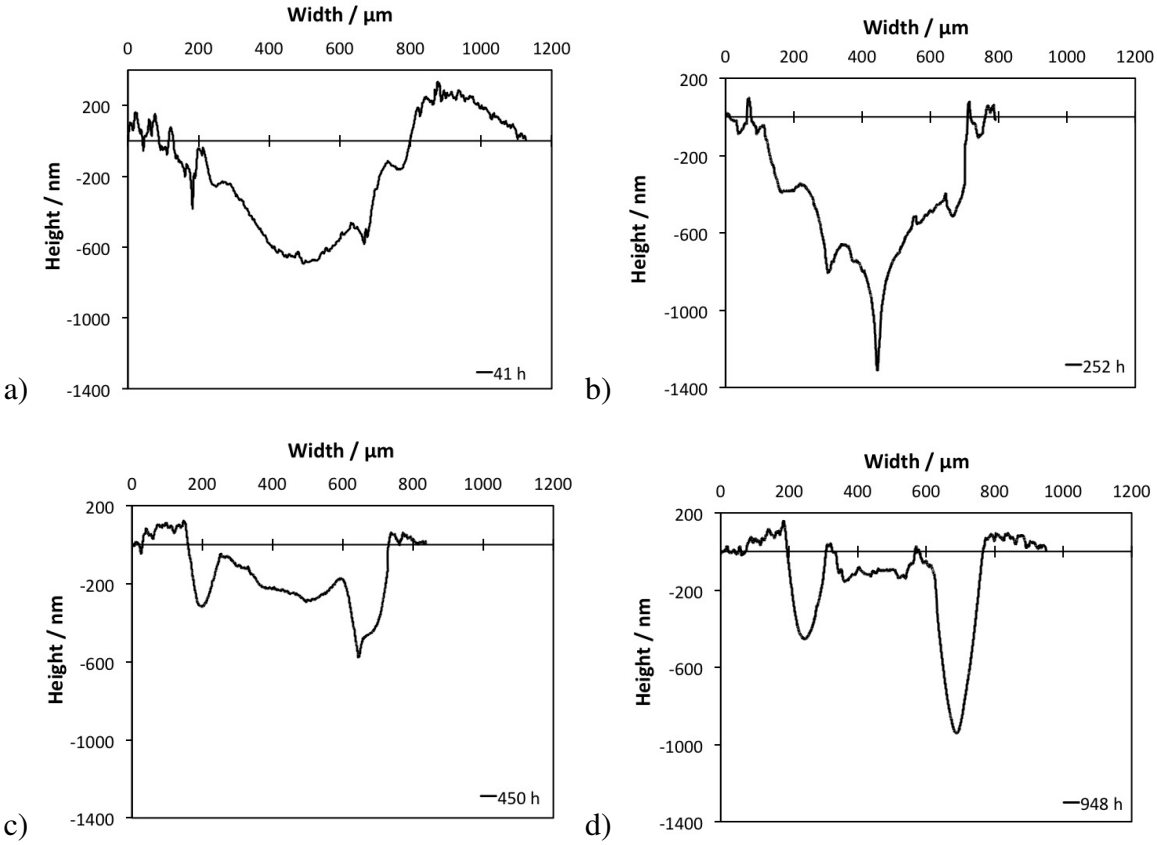

Fig. 6.2 Most representative profiles of the contact grooves for each of the different samples tested: a) 41 h, b) 252 h, c) 450 h, and d) 948 h. All graphs are plotted on the same scales for comparison.

to avoid interference between indents. However, it is not possible to obtain reliable hardness values within about 150 µm from the surface since the plastic zone of each indent extends about three times the indent size [192]. The results show that there is some hardening of the balls as a result of testing, but not much of a change with the bainitic rods. Note that only the rods with the single tracks are illustrated; tests have been done on the other rods but the hardness values are found to be similar, though they may not be reliable due to the multiple wear-tracks.

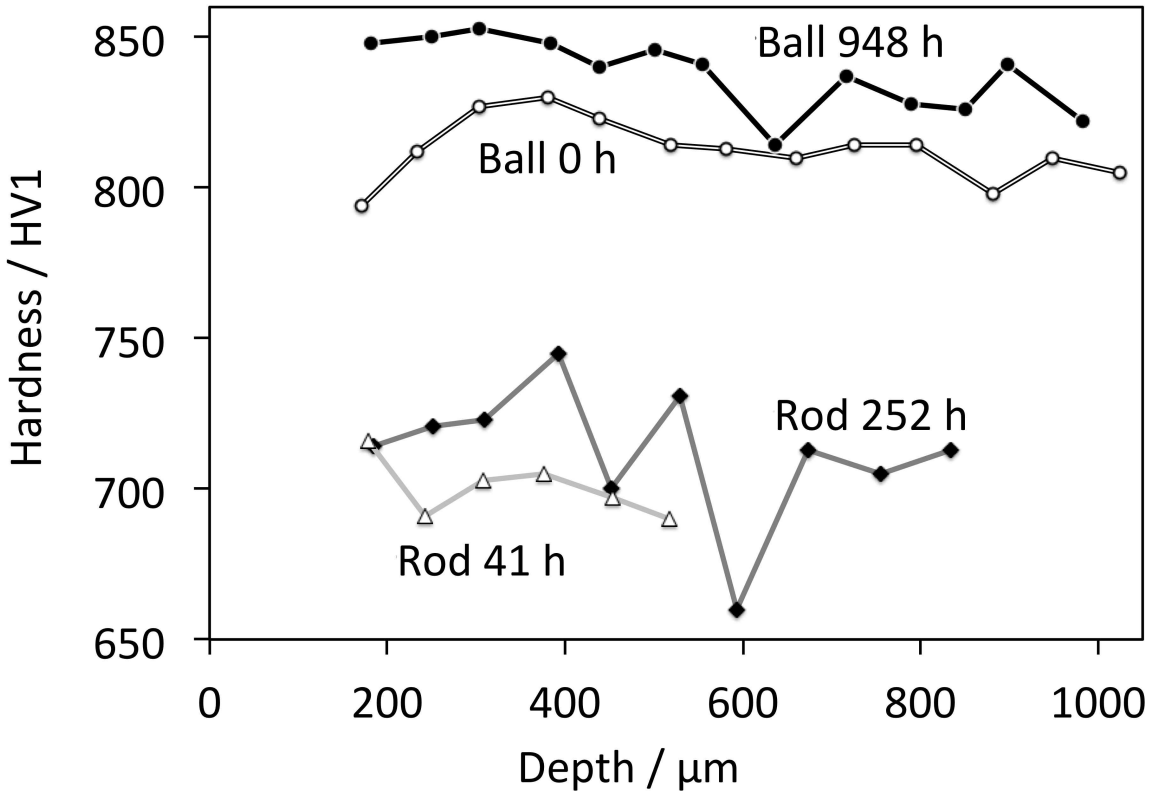

Fig. 6.3 Microhardness profile of the subsurface of balls and samples tested under RCF.

6.3.4 Microstructural characterisation

Balls

The microstructure of the new ball consists of a fine tempered martensite with an even distribution of proeutectoid cementite as shown in fig. 6.4, whereas the surface is polished to a nominal roughness of 0.013 µm and displays only a few shallow scratches. After 948 h of RCF under a Hertzian pressure of 3.5 GPa, all three balls displayed several contact grooves in random orientations denoting free movement of the ball within the bronze cage. In theory,

at least three grooves should be seen on each ball, all parallel to each other due to contact with the upper cup, the sample, and lower cup if there is a fixed rotational axis, parallel to the rotational axis of the test specimen. Although the grooves are signs of considerable material flow, there were no pits or cavities from flaked material of the balls that could have been indented into the surface of the test sample causing surface cracks. The microstructure below the contact grooves shows no signs of degradation apart from debonded inclusions and a run-in surface.

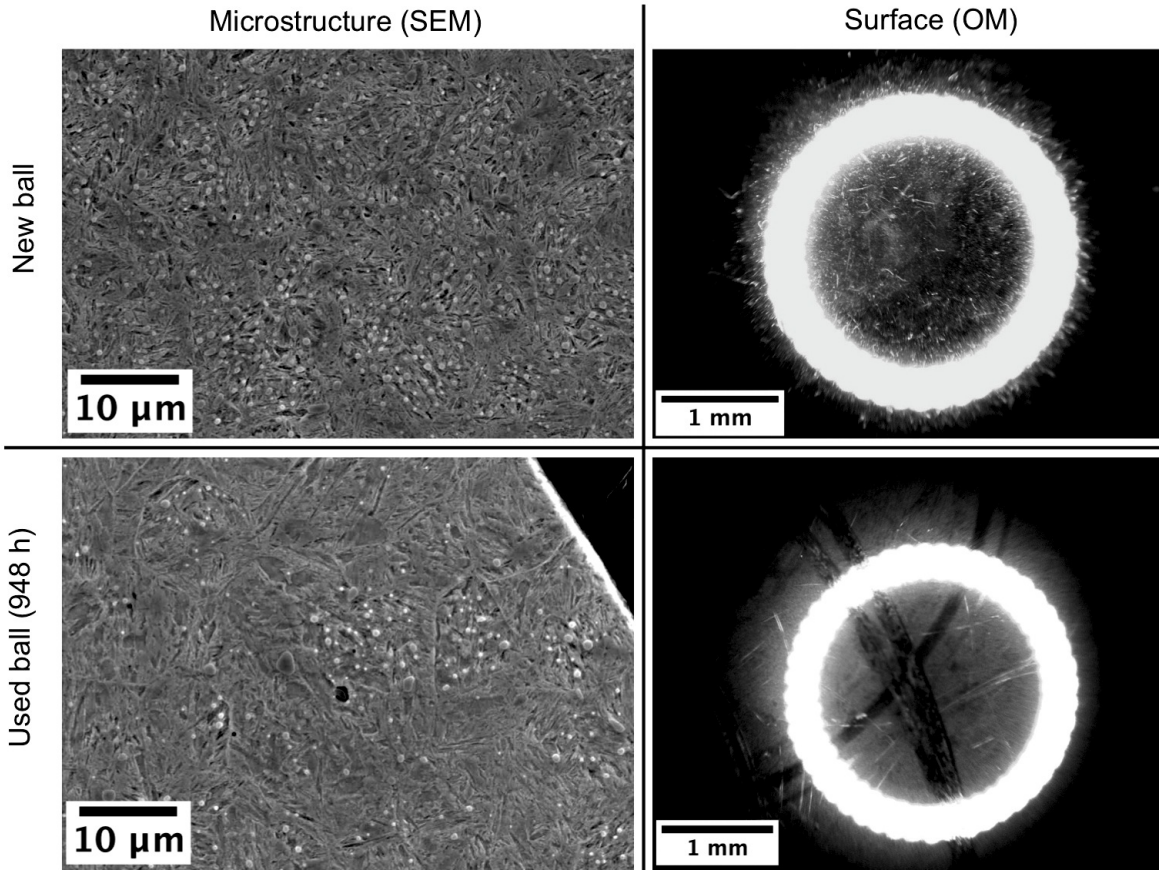

Fig. 6.4 Microstructure and surface of a new and used ball after RCF.

Test specimens

The unetched and etched (nital) microstructure of the test specimens that run for different times under RCF was characterised using OM and SEM. As seen in fig. 6.5a, the 41 h sample displays an infrequent distribution of clouds of tiny voids, marked by white arrows, that are sometimes located around inclusions. Some large inclusions like the one in fig. 6.5b, identified with EDS as a duplex aluminium and magnesium oxide, debonded from the matrix

and developed crack morphologies reminiscent of “butterflies" [4, 193], although without the classical white-etching wings.

More severe damage developed with time; the 252 h sample in fig. 6.5c and d shows a larger distribution of these clouds of voids, which were more severe around debonded inclusions, as marked by the white arrows, but also present in less intensity away from them. This sample also displayed a completely smoothened surface compared with the 41 h sample.

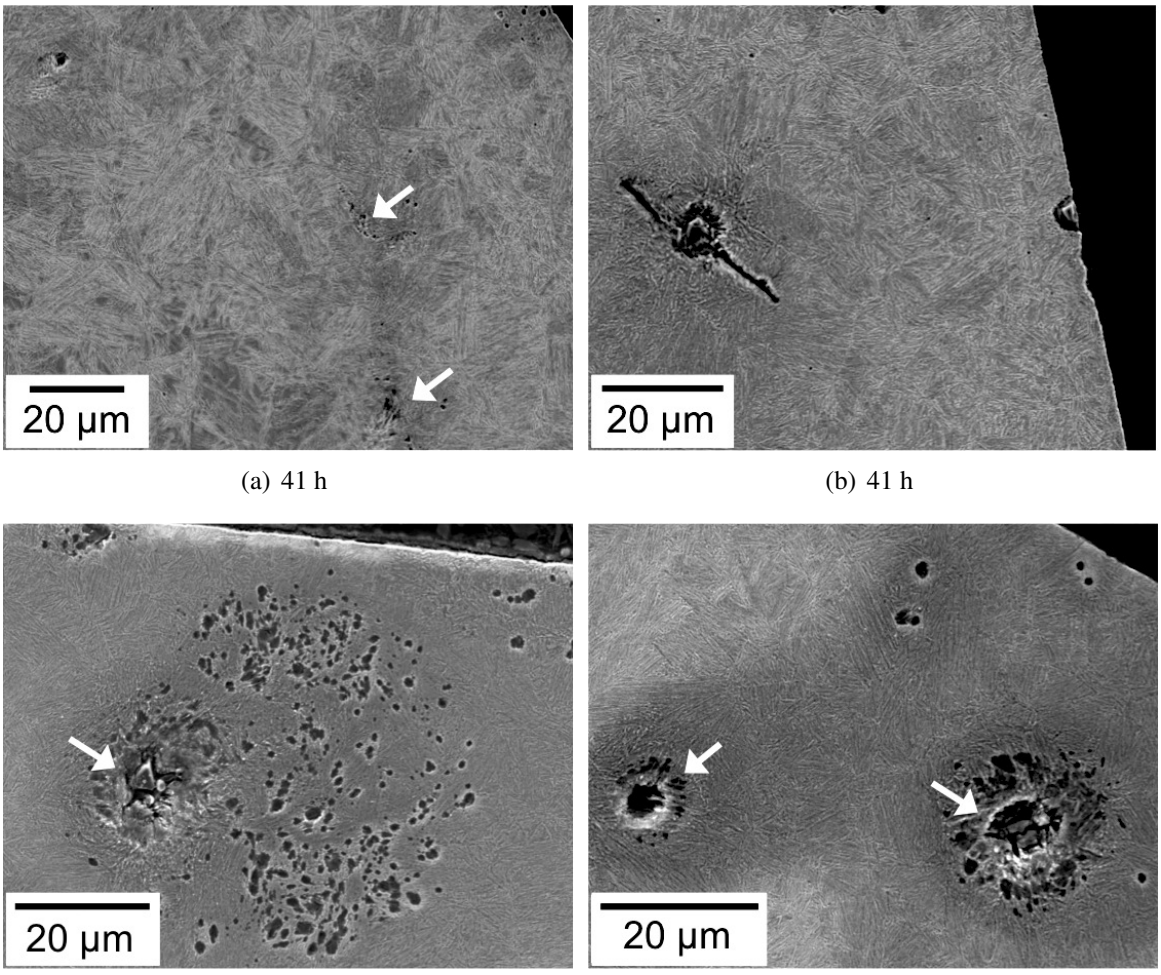

(a) 41 h (b) 41 h

(c) 252 h (d) 252 h

Fig. 6.5 SEM images of the radial cross section at the centre of wear tracks of two different RCF samples in the etched condition.

In the sample tested for 450 h a large collection of cracks up to a depth of $\sim 85\,\mu m$ was found in directions parallel and perpendicular to the contact surface, fig. 6.6a and b. This depth is consistent with the location of the maximum orthogonal shear stress at 99 µm, and

is consistent with the literature [194]. These cracks appear to form as result of the coalescence of the families of voids shown in the 41 h and 252 h samples. After 948 h, there is a very significant dispersion of these void-cracks in the subsurface of the sample, growing to some 60 μm in length (fig. 6.6c and d). Their growth seems to be driven by the absorption of continuously formed voids and guided to deflect damage by branching, normally in perpendicular directions as shown by the white arrows in (d), a mechanism that has been exploited to toughen brittle materials [162].

In order to study the mechanism of void-crack formation, two different crack-types were examined in detail. For this purpose, samples were carved out as lamellae using a FIB SEM and characterised using transmission electron microscopy. Fig. 6.7a shows a crack that has originated from a cluster of voids. As seen in fig 6.7b, there are numerous minuscule voids up to 60 nm in size at a depth of 2.5 μm below the gross damage illustrated in fig. 6.7a. Furthermore, there are fine cracks (about 7 nm thick) associated with the voids, and electron diffraction indicated that the whole region did not contain any retained austenite.

The second type of crack characterised has a branched morphology as mentioned earlier. Below the branched crack in fig. 6.8b, the layers of austenite and ferrite pointed by the arrow lose structure and blend into one dark homogenised ferritic phase around the voids. It can be seen in fig. 6.8c that a void (arrowed) is formed in what appears to be the interface between a blocky retained-austenite region transformed into martensite and a platelet of bainitic ferrite, with a fine crack confined within the softer ferrite. Electron diffraction verified the absence of blocky austenite in the regions of maximum subsurface shear-stresses, suggesting its deformation-induced transformation to untempered martensite. However, the thin layers of retained austenite were still present as seen in fig. 6.8d, which corresponds to the exact same region as fig. 6.8c after a slight tilt of the sample. The main void is still present as marked by the white arrow.

The evidence presented above suggests that the failure mechanism in nanostructured bainite under rolling contact fatigue is ductile void formation at the interfaces, for example between martensite and bainitic ferrite sheafs or between ferrite and austenite layers due to dislocation pile-up and compatibility requirements at the interface breaking down causing decohesion [195, 196]. It is well known in the context of dual phase steels [197–200], that ductile voids form at the interface between hard martensite and soft ferrite. In the present case, the larger regions of carbon-enriched retained austenite transform to hard martensite, creating the strain incompatibility. This could be the Achilles heel of the material in rolling

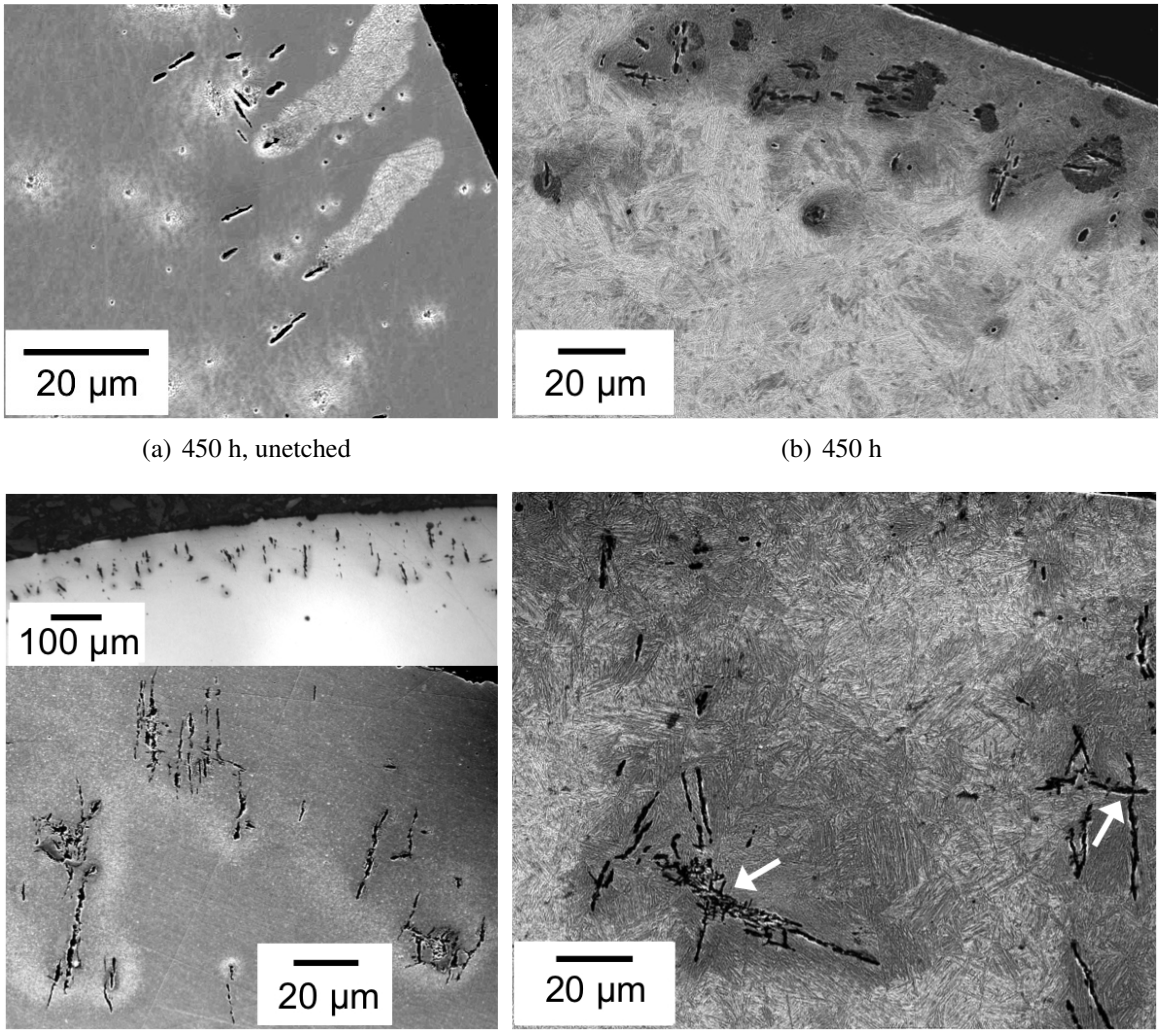

(a) 450 h, unetched (b) 450 h

(c) 948 h, unetched (d) 948 h

Fig. 6.6 SEM images of the radial cross section at the centre of wear tracks of two different RCF samples in the unetched and etched condition. Its important to note the light regions in (a) are not white-etching areas, but stains caused by water trapped at cracks . Likewise, the darker areas around cracks in (b) are not dark-etching regions, but overetched regions caused by nital trapped at cracks.

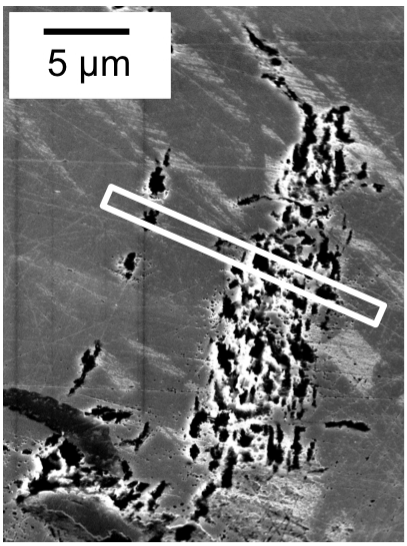

(a) Location of FIB sample

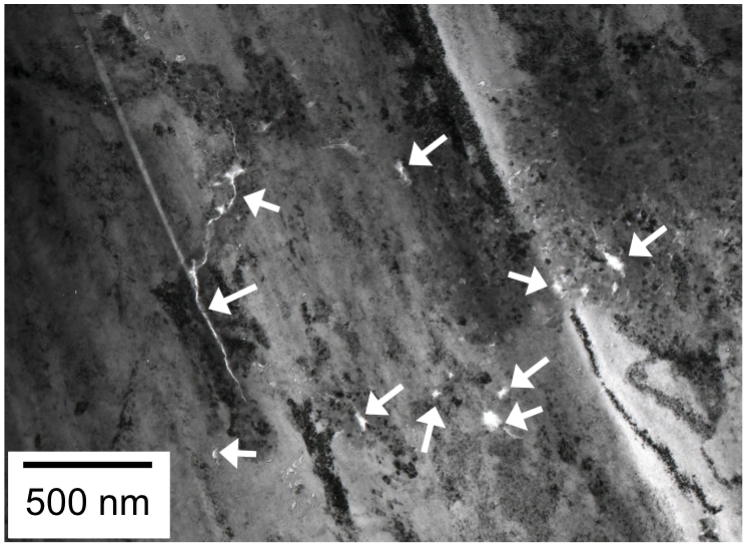

(b) Microscopic voids

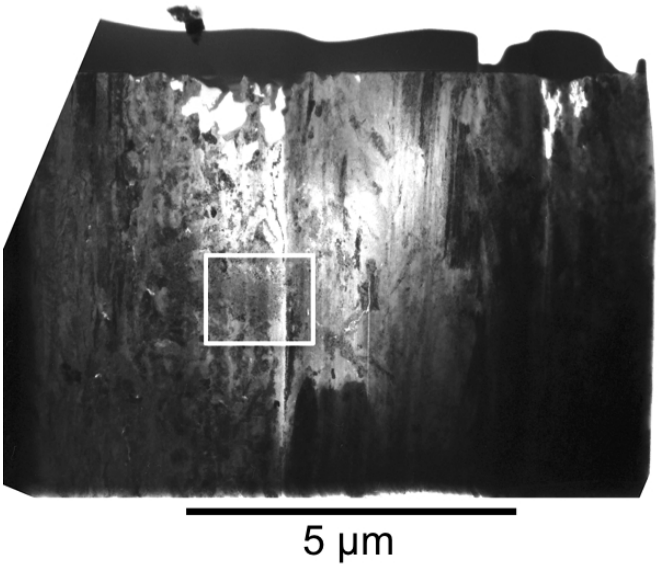

(c) Location of image shown in (b)

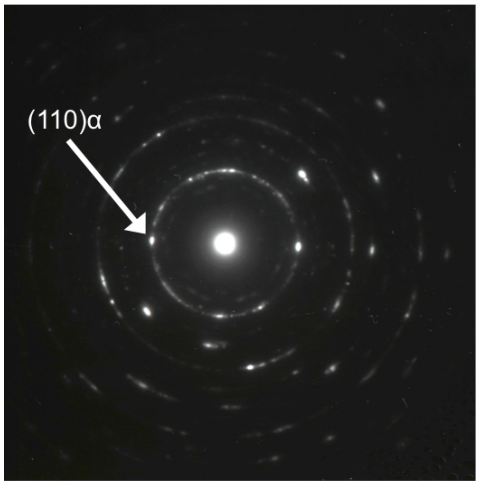

(d) Electron diffraction

Fig. 6.7 Images from a crack that has evolved from microscopic voids in the sample that clocked 948 h. (a) Shows the location of the region from which a sample was extracted for transmission electron microscopy. (b) Transmission electron micrograph illustrating microscopic voids and fine cracks associated with the voids, from a region well below the gross cracking. (c) The rectangle corresponds to the micrograph in (b). (d) Electron diffraction pattern showing the absence of any austenite.

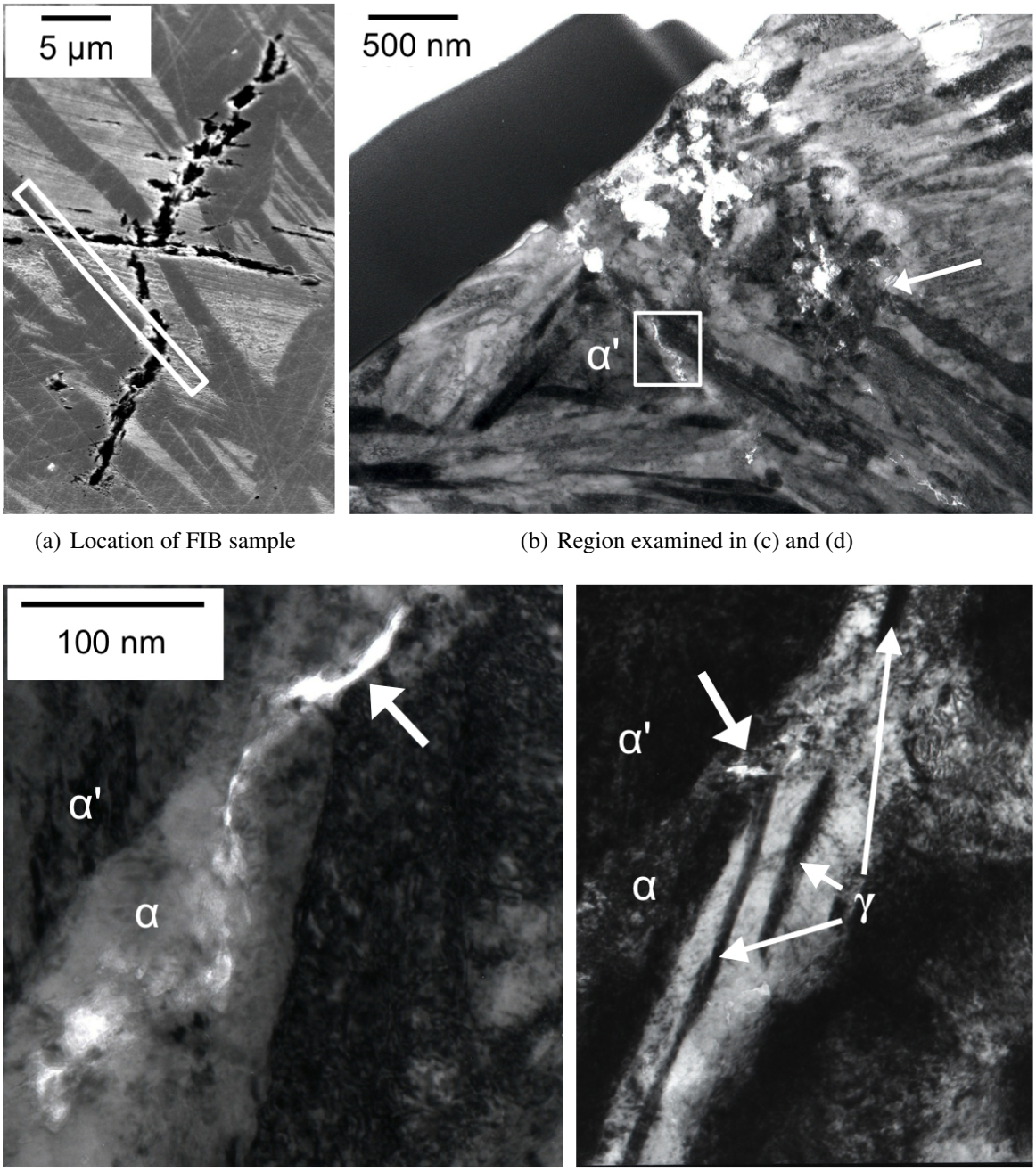

(a) Location of FIB sample

(b) Region examined in (c) and (d)

(c) Void and crack

(d) Films of austenite

Fig. 6.8 Images from a branched crack that has evolved from microscopic voids in the sample that clocked 948 h. (a) Shows the location of the region from which a sample was extracted for transmission electron microscopy. (b) The rectangle marks the region examined in (c) and (d). (c) Void at prior-γ/α interface and crack inside the bainite. (d) Same region as (c) but with the foil tilted.

contact fatigue, because unlike normal bearing steels, the fine scale structure will be mechanically heterogeneous if the austenite is not stable.

It was observed that when a crack eventually forms, it can lengthen within the bainitic ferrite when the latter is adjacent to the harder phase (fig. 6.8c); the consequence of this on the overall performance of the material is not clear. Nevertheless, the mechanisms of damage observed are radically different from those present in classical bearing steels such as the 52100 steel.

It is worth mentioning that no white-etching matter cracks were seen in any of the nanobainitic samples studied, even after 948 h, suggesting that the ductility of this alloy and its lack of carbides restrict the operation of hard white-etching matter formation mechanisms such as mechanical solution of fine carbides [4, 179].

X-ray Diffraction

The XRD results of a sample after heat treatment (0 h) and after RCF (948 h) summarised in table 6.3 confirm the stress-induced transformation of some small amount of retained austenite to martensite after RCF. As mentioned in last chapter, the X-ray beam used covers the whole area of the sample (39 mm^2), whereas the decomposition of austenite would only occur in the region of maximum subsurface shear stresses, which represents an area of maximum 3.7 mm^2 (0.25 mm thick all along the circumference of the half-disc sample of 9.53 mm in diameter) leading to an averaging [28]. Nevertheless, TEM imaging and diffraction patterns of the regions of maximum subsurface shear stress (fig. 6.7d) confirm only decomposition of blocky retained austenite, but not of the austenite films.

6.4 Conclusions

The following conclusions can be drawn about the rolling contact degradation of nanostructured bainite:

- The damage mechanism found is quite different from that observed in conventional bearing steels such as 52100. In particular, void formation is prominent, and the linking of these voids represents a key mechanism of damage evolution.
- The indications are that voids form at interfaces between regions of martensite and bainitic ferrite. The martensite here originates from the deformation-induced transformation of relatively coarse regions of austenite. It is safe to assume that the strain

Table 6.3 Volume fraction of bainitic ferrite (V_α), retained austenite (V_γ), and stress-induced martensite ($V_{\alpha'}$) for nanobainitic samples after 0 and 948 h of RCF. The error to all volume fractions is ± 0.01.

Analysis method	Phase fraction	Sample 0 h	Sample 948 h
austenite lattice parameter deduced from 002_γ, 022_γ, and 113_γ; all peaks (including those that overlap) used to determine volume fractions	V_α	0.779	0.761
	V_γ	0.213	0.209
	V'_α	0.008	0.030
austenite lattice parameter deduced from 002_γ, 022_γ, and 113_γ; only non-overlapping peaks used to determine volume fractions	V_α	0.802	0.796
	V_γ	0.198	0.183
	V'_α	0	0.021

incompatibility between the hard, untempered martensite and relatively soft bainite that induces void formation in a manner akin to dual-phase steels of the type used in automotive applications.

- The films of austenite maintain their stability under the rolling contact circumstances studied here. It is well known that such films are more stable than coarser regions due to a greater carbon concentration [90, 201–204] and their fine scale [205].

- The hardness of the affected regions of the nanostructured bainite does not change much due to rolling contact fatigue. This is unlike convention in the 52100 steel, as well as the lack of hard white-etching regions. The reason for this is that the fine mixture of bainitic ferrite and austenite does not contain any significant carbide precipitation, whereas in 52100, it is known that cementite can be induced to dissolve in the ferrite due to severe deformation, thus inducing a dramatic change in microstructure. For the same reason, when butterfly-like cracks initiate at inclusions within the bainitic steel, they were not seen to be associated with the hard white-etching “wings".

On the one hand, if void formation is promoted by the strain incompatibility arising when the retained austenite is induced to transform into hard martensite, then the structure may not be appropriate for rolling contact applications. On the other hand, the mixture of retained austenite and bainitic ferrite does not suffer from the effects of carbides, such as cementite dissolution and consequently hard white-etching matter formation. Furthermore,

when cracks do form by the linking of voids, they exhibit considerable branching, which must delay final fracture. This might explain why nanostructured bainite has been shown in independent work to outperform other microstructures [206], although it is noteworthy that in that study, the carbon concentration was exceptionally large at 1.26 wt% so that the structures observed were not uniform and contained proeutectoid cementite. Further work comparing carbide-free nanostructured bainite against conventional bearing steels is required to assess whether the failure mechanisms are better or worse than in the latter alloys.

Chapter 7

Conclusions

The following conclusions can be drawn about the work presented in this thesis:

1. Four heat treatments were developed to create different crack types and dispersions in a standard bearing steel. Two of these heat treatments proved to be especially useful: the one that created extensive martensite plate cracks in generating hard white-etching matter under rolling contact fatigue and irreversibly trapping hydrogen, and the one that introduced surface cracks in increasing the rolling contact fatigue life by 300% compared to a standard heat-treated and uncracked sample.

2. The evidence presented in chapter 4 suggests that hard white-etching matter is a consequence of microscopic fracture rather than the cause. During rolling contact fatigue, the crack faces in favourable orientations to the rolling direction and subsurface shear stresses rub and beat against each other, creating minute grains of ferrite as a result of recovery and recrystallisation. Therefore, one way to avoid the formation of hard WEM is by increasing the steel toughness, i.e. increasing the energy required for cracks to form and propagate.

3. The dissolution of carbides seems to be an essential requirement for hard WEM formation. This fact was indicated from the stronger presence of WEM around cracks surrounding tempered martensite than around cracks surrounding untempered stress-induced martensite, and from the lack of hard WEM around cracks in carbide-free nanostructured bainite. Carbides dissolve through cyclic stressing and the carbon supersaturates the nanostructured ferrite crystallites created by the beating action of cracks. Therefore, a second way to avoid the formation of hard WEM is to eliminate carbides from the microstructure.

4. By developing a local equilibrium model to reproduce hydrogen desorption from cracked samples it was possible to determine the binding energy of cracks, which corresponds to irreversible trapping, assuming hydrogen absorbed by them becomes molecular inside. RCF testing of a hydrogen charged cracked sample showed no acceleration of WEM formation or crack propagation despite many studies proving the damaging behaviour of hydrogen, confirming the success in hydrogen trapping by cracks and corroborating the assumptions made.

5. The lengthening of RCF life of the surface cracked sample compared with the uncracked one despite having similar surface roughnesses and the same testing conditions can be explained by the branching of cracks that deflect damage and toughen the otherwise brittle microstructure, such as in artificial composites.

6. The damage evolution mechanism of nanostructured bainite under rolling contact fatigue is presented for the first time and can be summarised by void formation at the interfaces between bainitic ferrite and deformation-induced martensite of relatively coarse regions of austenite and void linking into crack-like morphologies that branch out. Although void formation is not ideal for rolling contact fatigue applications, crack branching could delay final fracture and the lack of carbides could restrict hard WEM formation.

Chapter 8

Future work

Knowing the work performed in this thesis and the results obtained, the following work could be relevant for further research on the field:

1. An alternative way of introducing disconnected surfaces inside the bulk material could be by generating microscopic pores instead of cracks. In the past, these pores have been created homogeneously in the sample through power metallurgy and these generated substantial WEM around them after being tested in RCF. An alternative solution to generate pores mostly in the subsurface could be via ion bombardment. This effect occurs readily in steels used as cladding in nuclear plants, but no positive use of it has been implemented so far.

2. Another intriguing study would be to try to introduce a system of small cracks in nanostructured bainite meant for rolling contact applications as these cracks in standard bearing steel have been shown to deflect damage effectively raising the toughness of the material and delaying failure.

3. It would be interesting to assess whether the failure mechanisms of nanostructured bainite presented in this work are better or worse than the ones in conventional bearing steel.

4. Just as standard bearing steel was tested under rolling contact fatigue after being charged with hydrogen, it would be interesting to study if the damage evolution of nanostructured bainite under RCF changes with the presence of mobile hydrogen. The microstructural degradation process presented in this thesis corresponds to ductile void formation and linking, which could be affected by the embrittlement of hydrogen if the layers of retained austenite in the nanostructure are not percolating.

5. One of the most important contributions of this thesis is that dissolvable carbides appear to be a requirement for hard white-etching matter generation, such as disconnected surfaces that can rub against each other. However, more work needs to be performed by studying the butterfly cracks created at inclusions located in the maximum subsurface stress region of carbide-free nanostructured bainite to fully prove this idea.

References

[1] R. Errichello, S. Sheng, J. Keller, and A. Greco. Wind turbine tribology seminar. Technical Report DOE/GO-102012-3496 February 2012, U. S. Department of Energy, Golden, Colorado, USA, 2012.

[2] A. Grabulov, U. Ziese, and H. W. Zandbergen. TEM/SEM investigation of microstructural changes within the white etching area under rolling contact fatigue and 3-D crack reconstruction by focused ion beam. *Scripta Materialia*, 57:635–638, 2007.

[3] M.-H. Evans. White structure flaking (WSF) in wind turbine gearbox bearings: effects of 'butterflies' and white etching cracks (WECs). *Materials Science and Technology*, 28:3–22, 2012.

[4] H. K. D. H. Bhadeshia. Steels for bearings. *Progress in Materials Science*, 57:268–435, 2012.

[5] K. Hiraoka, M. Nagao, and T. Isomoto. Study of flaking process in bearings by white etching area generation. *Journal of ASTM International*, 3:234–240, 2007.

[6] R. Fougères, G. Lromand, A. Vincent, D. Nelias, G. dudragne, D. Girodin, G. Baudry, and P. Daguier. A new physically based model for predicting the fatigue life distribution of rolling bearings. In J. M. Beswick, editor, *Bearing Steel Technology*, pages 197–212, Philadelphia, USA, 2002. ASTM International.

[7] R. Irving and N. A. Scarlett. Wear problems associated with lubrication in inert atmospheres. *Wear*, 7:244–254, 1964.

[8] Y. Matsubara and H. Hamada. A novel method to evaluate the influence of hydrogen on fatigue properties of high strength steels. In J. M. Beswick, editor, *Bearing Steel Technology - Advances and State of the Art in Bearing Steel Quality Assurance*, pages 153–166, West Conshohocken, PA, USA, 2007. ASTM International.

[9] F. G. Caballero, H. K. D. H. Bhadeshia, K. J. A. Mawella, D. G. Jones, and P. Brown. Very strong, low–temperature bainite. *Materials Science and Technology*, 18:279–284, 2002.

[10] F. G. Caballero and H. K. D. H. Bhadeshia. Very strong bainite. *Current Opinion in Solid State and Materials Science*, 8:251–257, 2004.

[11] S. Fujita, S. Matsuoka, and T. Murakami. Effect of hydrogen on fatigue behaviour of bearing steel under cyclic torsion with compressive mean stress. In *Mechanics of Materials*, pages 241–243, Tokyo, Japan, 2000. Japan Society of Mechanical Engineers.

[12] K. Burkart, H. Bomas, R. Schroeder, and H.-W. Zoch. Rolling contact and compression-torsion fatigue of 52100 steel with special regard to carbide distribution. In *Advances in rolling contact fatigue strength testing and related substitute technologies*, pages 218–236, West Conshohocken, PA, USA, 2012. ASTM International.

[13] M. J. Dickson. Significance of texture parameters in phase analysis by X-ray diffraction. *Journal of Applied Crystallography*, 2:176–180, 1969.

[14] R. L. Bannerjee. X-ray determination of retained austenite. *Journal of Heat Treating*, 2:147–150, 1981.

[15] J. X. Zhang, P. M. Kelly, L. K. Bekessy, and J. D. Gates. Determination of retained austenite using an X-ray texture goniometer. *Materials Characterization*, 45:39–49, 2000.

[16] M. Radu, J. Valy, A. F. Gourgues, F. Le Strat, and A. Pineau. Continuous magnetic method for quantitative monitoring of martensitic transformation in steels containing metastable austenite. *Scripta Materialia*, 52:525–530, 2005.

[17] L. K. Perry, D. H. Ryan, and R. Gagon. Studying surfaces and thin films using mössbauer spectroscopy. *Hyperfine Interactions*, 170:131–143, 2006.

[18] J. Talonen, P. Aspergren, and H. Hänninen. Comparison of different methods for measuring strain induced martensite content in austenitic steels. *Materials Science and Technology*, 20:1506–1512, 2004.

[19] P. J. Jacques, S. Allain, O. Bouaziz, A. De, A. F. Gourgues, B. M. Hance, Y. Houbaert, J. Huang, A. Iza-Mendia, S. E. Kruger, M. Radu, L. Samek, J. Speer, L. Zhao, and S. van der Zwaag. On measurement of retained austenite in multiphase TRIP steels — results of blind round robin test involving six different techniques. *Materials Science and Technology*, 25:567–574, 2009.

[20] L. Zhao, N. H. van Dijk, A. J. Lefering, and J. Sietsma. Magnetic detection of small fractions of ferromagnetic martensite within the paramagnetic austenite matrix of TWIP steel. *Journal of Materials Science*, 48(4):1474–1479, 2013.

[21] L. Zhao, N. H. Van Dijk, E. Brück, J. Sietsma, and S. Van der Zwaag. Magnetic and X-ray diffraction measurements for the determination of retained austenite in trip steels. *Materials Science and Engineering A*, 313(1):145–152, 2001.

[22] S. S. M. Tavares, P. D. S. Pedrosa, J. R. Teodosio, M. R. Da Silva, J. M. Neto, and S. Pairis. Magnetic properties of the UNS S39205 duplex stainless steel. *Journal of alloys and compounds*, 351(1):283–288, 2003.

[23] S. S. M. Tavares, J. M. Pardal, J. A. De Souza, J. M. Neto, and M. R. Da Silva. Magnetic phase quantification of the UNS S32750 superduplex stainless steel. *Journal of Alloys and Compounds*, 416(1):179–182, 2006.

[24] S. S. M. Tavares, S. R. Mello, A. M. Gomes, J. M. Neto, M. R. Da Silva, and J. M. Pardal. X-ray diffraction and magnetic characterization of the retained austenite in a chromium alloyed high carbon steel. *Journal of Materials Science*, 41(15):4732–4736, 2006.

[25] J. M. Pardal, S. S. M. Tavares, M. C. Fonseca, M. R. da Silva, J. M. Neto, and H. F. G. Abreu. Influence of temperature and aging time on hardness and magnetic properties of the maraging steel grade 300. *Journal of Materials Science*, 42(7):2276–2281, 2007.

[26] T. S. Nisbet. *Rolling Bearings*. Number 04 in Engineering Design Guides. Oxford University Press, 1974.

[27] A. Patel, R. Palka, and B. A. Glowacki. New fully superconducting bearing concept using the difference in irreversibility field of two superconducting components. *Superconductor Science and Technology*, 24(1), 2010.

[28] A. P. Voskamp. *Microstructural Changes During Rolling Contact Fatigue*. PhD thesis, Technical University of Delft, 1996.

[29] SKF. *General Catalogue*. Germany, 5000e edition, 2003.

[30] H. K. D. H. Bhadeshia. Mechanical bearings. Technical Report http://www.msm.cam.ac.uk/phase-trans/2010/types/index.html, University of Cambridge, Cambridge, U. K., 2010.

[31] T. A. Harris and M. N. Kotzalas. *Essential Concepts of Bearing Technology*. Taylor & Francis, 2007.

[32] M. J. Neale. *Bearings: A Tribology Handbook*. SAE International. Butterworth Heinemann, London, U.K., 1973.

[33] SKF. Interactive engineering catalogue and bearing selector, December 2012.

[34] E. N. Bamberger. Effect of materials – metallurgy viewpoint. In P. M. Ku, editor, *Interdisciplinary Approach to the Lubrication of Concentrated Contacts*, number SP–237 in NASA, pages 409–437, Washington, D. C., USA, 1970. NASA.

[35] E. V. Zaretsky. Rolling bearing steels – a technical and historical perspective. *Materials Science and Technology*, 28:58–69, 2011.

[36] W. J. Anderson, E. N. Bamberger, W. E. Poole, R. L. Thom, and E. V. Zaretsky. STLE life factors for rolling bearings. In E. V. Zaretsky, editor, *Materials and Processing*, pages 71–128, Park Ridge, IL, 1992. Society of Tribologists and Lubrication Engineers.

[37] F. Sadeghi, B. Jalahmadi, T. S. Slack, N. Raje, and N. K. Arakere. A review of rolling contact fatigue. *Journal of Tribology*, 131:041403, 2009.

[38] B. M. Glasgal. Bearing steel 20/20 – a steelmaker's view point – a look back 20 years and a look forward 20 years. In J. J. C. Hoo and W. B. Green, editors, *Bearing Steels: into the 21st Century*, pages 189–201, Pennsylvania, USA, 1998. American Society for Testing of Materials.

[39] J. A. Eckel, P. C. Glawas, J. O. Wolfe, and B. J. Zorc. Clean engineered steels-progress at the end of the twentieth century. In J. K. Mahaney Jr, editor, *Advances in the Production and Use of Steel with Improved Internal Cleanliness*, pages 1–10, Pennsylvania, USA, 1999. ASTM.

[40] T. Sakai, Y. Sato, and N. Oguma. Characteristic S–N properties of high-carbon–chromium-bearing steel under axial loading in long-life fatigue. *Fatigue & Fracture of Engineering Materials & Structures*, 25:765–773, 2002.

[41] N. Tsunekage, K. Hashimoto, T. Fujimatsu, and K. Hiraoka. Initiation behaviour of crack originated from non–metallic inclusion in rolling contact fatigue. *Journal of ASTM International*, 7:JAI102612, 2010.

[42] L. Zhang and B. G. Thomas. Inclusions in continuous casting of steel. In *XXIV National Steelmaking Symposium*, pages 138–183, Morelia, Mexico, 2003.

[43] B. V. Molotilov and P. I. Yugov. Metallurgy of bearing steel. *Steel in Translation*, 38:565–568, 2008.

[44] G. Krauss. The effect of austenitising on microstruture and fracture of hardened high carbon steels. In B. N. Prakash Babu, editor, *Wear and Fracture Prevention*, pages 147–161, Metals Park, Ohio, USA, 1981. ASM.

[45] G. Krauss. The relationship of microstructure to fracture morphology and toughness of hardened hypereutectoid steels. In D. E. Diesburg, editor, *Case–Hardened Steels: Microstructural and Residual Stress Effects*, pages 33–58, Warrendale, Pennsylvania, USA, 1983. TMS–AIME.

[46] S. H. H. Ibragimov, P. I. Polukhin, A. M. llin, A. M. Galkin, and V. I. Pilyushenko. Auger spectroscopy of the fracture surface of steel ShKh15. *Russian Metallurgy* (Metally), 2:147–149, 1985.

[47] L. Karmazin. Experimental study of the austenitization process of hypereutectoid steel alloyed with small amounds of silicon, manganese and chromium, and with an initial structure of globular cementite in a ferrite matrix. *Materials Science & Engineering A*, 142:71–77, 1991.

[48] J. M. Beswick. Effect of prior cold work on the martensite transformation in SAE 52100. *Metallurgical & Materials Transactions A*, 15:299–306, 1984.

[49] C. A. Stickels. Carbide refining heat treatment for 52100 bearing steels. *Metallurgical Transactions*, 5:865–874, 1974.

[50] K. Monma, R. Maruta, T. Yamamoto, and Y. Wakikado. Effect of particle sizes of carbides and amounts of undissolved carbide on the fatigue life of bearing steel. *Journal of the Japan Institute of Metals*, 32:1198–1204, 1968.

[51] C. A. Stickels. Rolling contact fatigue tests of 52100 bearing steel using a modified NASA ball test rig. *Wear*, 199–210, 1984.

[52] S. Das Bakshi, P. H. Shipway, and H. K. D. H. Bhadeshia. Three-body abrasive wear of fine pearlite, nanostructured bainite and martensite. *Wear*, 308:46–53, 2013.

[53] E. D. Scott. The effect of steelmaking, vacuum melting and casting techniques on the life of rolling bearings. *Vacuum*, 19:167–169, 1969.

[54] R. A. Baughman. Effect of hardness, surface finish, and grain size on rolling-contact fatigue life of M50 bearing steel. *Journal of Basic Engineering*, 82:287–294, 1960.

[55] A. R. Marder and A. O. Benscoter. Microcracking in plate martensite of AISI 52100 steel. *Metallurgical & Materials Transactions B*, 1:3234–3237, 1970.

[56] C. Sommer, H.-J. Christ, and H. Mughrabi. Non-linear elastic behaviour of the roller bearing steel SAE 52100 during cyclic loading. *Acta Metallurgica and Materialia*, 39:1177–1187, 1991.

[57] D. Umbrello, A. D. Jayal, S. Caruso, O. W. Dillon, and I. S. Jawahir. Modelling of white and dark layer formation in hard machining of AISI 52100 bearing steel. *Machining Science and Technology*, 14:128–147, 2010.

[58] H. K. D. H. Bhadeshia. Thermodynamic extrapolation and the martensite-start temperature of substitutionally alloyed steels. *Metal Science*, 15:178–180, 1981.

[59] A. T. W. Barrow, J. H. Kang, and P. E. J. Rivera-Díaz del Castillo. The $\varepsilon \rightarrow \eta \rightarrow \theta$ transition in 100Cr6 and its effect on mechanical properties. *Acta Materialia*, 60(6):2805–2815, 2012.

[60] A. G. Allten and P. Payson. The effect of silicon on the tempering of martensite. *Trans. ASM*, 45:498–532, 1953.

[61] H. Nakashima. Trends in materials and heat treatments for rolling bearings. Technical Report Technical Review No. 76, NTN Corporation, Osaka, Japan, 2008.

[62] J. M. Beswick. Steel with a composition of iron, carbon, phophorus and molybdenum. Technical Report US Patent 4,961,904, U. S. Patent Office, 1990.

[63] R. G. Davies and C. L. Magee. Microcracking in ferrous martensites. *Metallurgical Transactions*, 3:307–313, 1972.

[64] A. R. Marder, A. O. Benscoter, and G. Krauss. Microcracking sensitivity in Fe–C plate martensite. *Metallurgical Transactions*, 1:1545–1549, 1970.

[65] J. Lyman. High crabon steel microcracking during hardening. *Journal of Engineering Materials and Technology*, 106:253–256, 1984.

[66] S. Chatterjee and H. K. D. H. Bhadeshia. TRIP–assisted steels: cracking of high carbon martensite. *Materials Science and Technology*, 22:645–649, 2006.

[67] M. G. Mendiratta, J. Sasser, and G. Krauss. Effect of dissolved carbon on microcracking in martensite of an Fe-1.39C alloy. *Metallurgical Transactions*, 3:351–353, 1972.

[68] Z. Lei, A. Zhao, J. Xie, C. Sun, and Y. Hong. Very high cycle fatigue for GCr15 steel with smooth and hole-defect specimens. *Theoretical and Applied Mechanics Letters*, 2:031003, 2012.

[69] L. C. D. Fielding. The bainite controversy. *Materials Science and Technology*, 29:383–399, 2013.

[70] H. K. D. H. Bhadeshia. *Bainite in Steels, 2nd edition*. Institute of Materials, London, U.K., 2001.

[71] H. K. D. H. Bhadeshia. Nanostructured bainite. *Proceedings of the Royal Society of London A*, 466:3–18, 2010.

[72] H. K. D. H. Bhadeshia. The first bulk nanostructured metal. *Science and Technology of Advanced Materials*, 14:014202, 2013.

[73] F. G. Caballero, C. Garcia-Mateo, and M. K. Miller. Design of novel bainitic steels: Moving from ultrafine to nanoscale structures. *Journal of Metals*, ?:DOI: 10.1007/s11837–014–0908–0, 2014.

[74] T. S. Wang, J. Yang, C. J. Shang, X. Y. Li, B. Lv, M. Zhang, and F. C. Zhang. Sliding frction surface microstructure and wear resistance of 9SiCr steel with low–temperature austempering treatment. *Surface & Coatings Technology*, 202:4036–4040, 2008.

[75] P. Zhang, F. C. Zhang, Z. G. Yan, T. S. Wang, and L. H. Qian. Wear property of low-temperature bainite in the surface layer of a carburized low carbon steel. *Wear*, 271:697–704, 2011.

[76] A. Leiro, A. Kankanala, E. Vuorinen, and B. Prakash. Tribological behaviour of carbide-free bainitic steel under dry rolling/sliding conditions. *Wear*, 273:2–8, 2011.

[77] J. Yang, T. S. Wang, B. Zhang, and F. C. Zhang. Sliding wear resistance and worn surface microstructure of nanostructured bainitic steel. *Wear*, 282–283:81–84, 2012.

[78] A. Leiro, E. Vuorinen, K. G. Sundin, B. Prakash, T. Sourmail, V. Smanio, F. G. Caballero, C. Gracia-Mateo, and R. Elvira. Wear of nano-structured carbide-free bainitic steels under dry rolling-sliding conditions. *Wear*, 298–299:42–47, 2013.

[79] T. Sourmail, F. G. Caballero, C. Garcia-Mateo, V. Smanio, C. Ziegler, M. Kuntz, R. Elvira, A. Leiro, E. Vuorinen, and T. Teeri. Evaluation of potential of high Si high C steel nanostructured bainite for wear and fatigue applications. *Materials Science and Technology*, 29:1166–1173, 2013.

[80] S. Das Bakshi, A. Leiro, B. Prakash, and H. K. D. H. Bhadeshia. Dry rolling/sliding wear of nanostructured bainite. *Wear*, 316:70–78, 2014.

[81] X. Y. Feng, F. C. Zhang, J. Kang, Z. N. Yang, and X. Y. Long. Sliding wear and low cycle fatigue properties of new carbide free bainitic rail steel. *Materials Science and Technology*, 30(12):1410–1418, 2014.

[82] M. J. Peet, P. Hill, M. Rawson, S. Wood, and H. K. D. H. Bhadeshia. Fatigue of extremely fine bainite. *Materials Science and Technology*, 27:119–123, 2011.

[83] L. C. D. Fielding, E. J. Song, D. K. Han, H. K. D. H. Bhadeshia, and D. W. Suh. Hydrogen diffusion and the percolation of austenite in nanostructured bainitic steel. *Proceedings of the Royal Society of London A*, 470:20140108, 2014.

[84] H. K. D. H. Bhadeshia. Properties of fine–grained steels generated by displacive transformation. *Materials Science and Engineering A*, 481–482:36–39, 2008.

[85] M. Sherif, C. Garcia-Mateo, T. Sourmail, and H. K. D. H. Bhadeshia. Stability of retained austenite in TRIP–assisted steels. *Materials Science and Technology*, 20(3):319–322, 2004.

[86] M. J. Peet. *Transformation and Tempering of Low Temperature Bainite*. PhD thesis, University of Cambridge, 2010.

[87] W. Solano-Alvarez and H. K. D. H. Bhadeshia. White-etching matter in bearing steel. part I: Controlled-cracking of bearing steel. *Metallurgical & Materials Transactions A*, 45(11):4907–4915, 2014.

[88] C. Garcia-Mateo, F. G. Caballero, and H. K. D. H. Bhadeshia. Acceleration of low–temperature bainite. *ISIJ International*, 43:1821–1825, 2003.

[89] C. Garcia-Mateo, M. Peet, F. G. Caballero, and H. K. D. H. Bhadeshia. Tempering of a hard mixture of bainitic ferrite and austenite. *Materials Science and Technology*, 20:814–818, 2004.

[90] H. J. Stone, M. J. Peet, H. K. D. H. Bhadeshia, P. J. Withers, S. S. Babu, and E. D. Specht. Synchrotron X-ray studies of austenite and bainitic ferrite. *Proceedings of the Royal Society A*, 464:1009–1027, 2008.

[91] H. S. Hasan, M. J. Peet, M-N. Avettand-Fènoël, and H. K. D. H. Bhadeshia. Effect of tempering upon the tensile properties of a nanostructured bainitic steel. *Materials Science and Engineering A*, 615:340–347, 2014.

[92] H. Hertz. Über die berübrung fester elastiscber Körper (on the contact of elastic solids). *J. reine und angewandte Mathematik*, 92:156–171, 1882.

[93] L. Coelho, A. Dias, H. P. Lieurade, and H. Maitournam. Experimental and numerical rolling contact fatigue study on the 32CrMoV13 steel. *Fatigue and Fracture of Engineering Materials and Structures*, 27:811–823, 2004.

[94] A. B. Jones. New departure engineering data: Analysis of stresses and deflections. New departure division, General Motors Corp., Bristol, CT, 1946.

[95] H. Thomas and V. Hoersch. Stresses due to the pressure of one elastic solid upon another. University of Illinois Bulletin, 1930.

[96] K. Johnson. *The effects of oscillating trangential force at the interface between elastic bodies in contact*. Phd thesis, University of Manchester, 1954.

[97] G. Lundberg and A. Palmgren. Dynamic capacity of rolling bearings. *Acta Polytechnica - Mechanical Engineering Series*, 1:4–51, 1947.

[98] T. A. Stolarski and S. Tobe. *Rolling Contacts*. Professional Engineering Publishing, UK, 2000.

[99] D. A. Hills and D. W. Ashelby. The influence of residual stresses on contact-load-bearing capacity. *Wear*, 75:221–239, 1982.

[100] B. Wilke. Hysteresis loop of an elastic–plastic $\lambda/2$ oscillator. *Physica Status Solidi*, 23:237–244, 1974.

[101] D. McLean. *Mechanical Properties of Metals*. John Wiley & Sons, New York, USA, 1962.

[102] S. Kocanda and A. Likowski. Fatigue crack growth rate in high-strength steel under bending. *Mémoires Scientifiques Revue Métallurgie*, 76:345–350, 1970.

[103] S. Shimizu, K. Tsuchiya, and K. Tosha. Probabilistic stress-life (P-S-N) study on bearing steel using alternating torsion life test. *Tribology Transactions*, 52:806–816, 2009.

[104] E. Zaretsky. In search of a fatigue limit: a critique of ISO standard 281:2007. *Tribology and Lubrication Technology*, 66:30–40, 2010.

[105] K. Shiozawa and L. Lu. Very high-cycle fatigue behaviour of shot-peened high-carbon–chromium bearing steel. *Fatigue & Fracture of Engineering Materials & Structures*, 25:813–822, 2002.

[106] E. Ioannides, G.Bergling, and A. Gabelli. An analytical formulation for the life of rolling bearings. *Acta Ploytechnica Scandinavica*, 137:1–80, 1999.

[107] T. A. Harris and M. N. Kotzalas. *Advanced Concepts of Bearing Technology*. Taylor & Francis, 2007.

[108] W. Nierlich, J. Gegner, and M. Bruckner. X-ray diffraction in failure analysis of rolling bearings. *Materials Science Forum*, 524–525:147–152, 2006.

[109] J. Lankford and F. N. Kusenberger. Initiation of fatigue cracks in 4340 steel. *Metallurgical Transactions*, 4:553–559, 1973.

[110] N. P. Suh. An overview of the delamination theory of wear. *Wear*, 44:1–16, 1977.

[111] G. R. Chanani, S. D. Antolovich, and W. W. Gerberich. Fatigue crack propagation in TRIP steels. *Metallurgical Transactions*, 3:2661–2672, 1972.

[112] H. Swahn, P. C. Becker, and O. Vingsbo. Martensite decay during rolling contact fatigue in ball bearings. *Metallurgical & Materials Transactions A*, 7:35–39, 1976.

[113] K. Sugino, K. Miyamoto, M. Nagumo, and K. Aoki. Structural alterations of bearing steels under rolling contact fatigue. *Trans. Iron Steel Institute of Japan*, 10:98–111, 1970.

[114] R. Österlund and O. Vingsbo. Phase changes in fatigued ball bearings. *Metallurgical & Materials Transactions A*, 11:701–707, 1980.

[115] R. O. Ritchie. Influence of microstructure on near-threshold fatigue crack propagation in ultra high strength steel. *Metal Science*, 11:368–381, 1977.

[116] J. A. Martin, S. F. Borgese, and A. D. Eberhardt. Microstructural alterations of rolling–bearing steel undergoing cyclic contact. *ASME Journal of Basic Engineering*, 88:555–567, 1966.

[117] J. Takahashi, K. Kawakami, and M. Ueda. Atom probe tomography analysis of the white etching layer in a rail track surface. *Acta Materialia*, 58:3602–3612, 2010.

[118] B. Loy and R. McCallum. Mode of formation of spherical particles in rolling contact fatigue. *Wear*, 24:219–228, 1973.

[119] J. M. Beswick. Measurement of carbon levels in structurally transformed SAE 52100 ball bearing steel by microprobe analysis. *Practical Metallography*, 12:200–206, 1975.

[120] N. Mitamura, H. Hidaka, and S. Takaki. Microstructural development in bearing steel during rolling contact fatigue. *Materials Science Forum*, 539–543:4255–4260, 2007.

[121] H. Harada, T. Mikami, M. Shibata, D. Sokai, A. Yamamoto, and H. Tsubakino. Microstructural changes and crack initiation with white etching area formation under rolling/sliding contact in bearing steel. *ISIJ International*, 45:1897–1902, 2005.

[122] J. Buchwald and R. W. Heckel. An analysis of microstructural changes in 52100 steel bearings during cylic stressing. *Trans. ASM*, 61:750–756, 1968.

[123] P. C. Becker, H. Swahn, and O. Vingsbo. Structural changes in ball bearing steels caused by rolling contact fatigue. *Mecanique Matériaux électricité*, 320–321:8–14, 1976.

[124] V. Bhargava, G. T. Hahn, and C. A. Rubin. Rolling contact deformation, etching effects, and failure of high-strength bearing steel. *Metallurgical & Materials Transactions A*, 21:1921–1931, 1990.

[125] R. Österlund, O. Vingsbo, L. Vincent, and P. Guiraldenq. Butterflies in fatigued ball bearings - formation mechanisms and structure. *Scandinavian Journal of Metallurgy*, 11:23–32, 1982.

[126] A. Grabulov, R. Petrov, and H. W. Zandbergen. EBSD investigation of the crack initiation and TEM/FIB analyses of the microstructural changes around the cracks formed under rolling contact fatigue. *International Journal of Fatigue*, 32:576–583, 2010.

[127] W. Lojkowski, M. Djahanbakhsh, G. Bürkle, S. Gierlotka, W. Zielinski, and H. J. Fecht. Nanostructure formation on the surface of railway tracks. *Materials Science & Engineering A*, 303:197–208, 2001.

[128] G. Baumann. Formation of white-etching layers on rail treads. *Wear*, 191:133–140, 1996.

[129] X. Sauvage, J. M. Le Breton, A. Guillet, A. Meyer, and J. Teillet. Phase transformations in surface layers of machined steels investigated by X-ray diffraction and mossbauer spectroscopy. *Materials Science & Engineering A*, 362:181–186, 2003.

[130] C. Mao, X.-M. Huang, Y.-L. Li, and Z.-X. Zhou. Characterisitics of affected layer in surface grinding of hardened bearing steel. *Nanotechnology and Precision Engineering*, 8:356–361, 2010.

[131] K. Hashimoto, K. Hiraoka, K. Kida, and E. Costa Santos. Effect of sulphide inclusions on rolling contact fatigue life of bearing steels. *Materials Science and Technology*, 28:39–43, 2012.

[132] A. Marze, L. Vincent, B. Coquillet, J. Munier, and P. Guiraldenq. Evolution et dégradation par fatigue de la structure martensitique d'un acier semi-rapide. *Mémoires et études scientifiques de la revue de métallurgie*, 76:165–173, 1979.

[133] M.-H. Evans, A. D. Richardson, I. Wang, and R. J. K. Wood. Tomographic serial sectioning investigation of butterfly and white etching crack (wec) formation in wind turbine gearbox bearings. *Wear*, 302:1573–1582, 2013.

[134] M.-H. Evans, L. Wang, H. Jones, and R. J. K. Wood. White Etching Crack (WEC) Investigation by Serial Sectioning, Focused Ion Beam and 3-D Crack Modelling*. *Tribology International*, 65:146–160, 2013.

[135] B. Zhang, W. Shen, Y. Liu, X. Tang, and Y. Wang. Microstructures of surface white layer and internal white adiabatic shear band. *Wear*, 211(164–168), 1997.

[136] D. M. Turley. The nature of the white-etching surface layers produced during reaming ultra-high strength steel. *Materials Science and Engineering*, 19:79–86, 1975.

[137] K. Ryttberg, M. K. Wedel, P. Dahlman, and L. Nyborg. Microstructure of surface zones subjected to high-velocity parting-off. *Journal de Physique IV (Proceedings)*, 134:1313–1318, 2006.

[138] S. B. Newcomb and W. M. Stobbs. A transmission electron microscope study of the white etching layer on a rail head. *Materials Science & Engineering A*, 66:195–204, 1984.

[139] H. Schlicht. About adiabatic shear bands and the generation of "high-angle white bands" in roller bearings. *Materialwissenschaft und Werkstofftechnik*, 39:217–226, 2008.

[140] Gegner J. Tribological aspects of rolling bearing failures in tribology- lubricants and lubrication. Chapter 2, SKF GmbH, Department of Material Physics/ Institute of Materials Science, University of Siegen, Germany., 2011.

[141] P. Schatzberg and I. M. Felsen. Effect of water and oxygen during rolling contact lubrication. *Wear*, 12:331–342, 1968.

[142] K. Tamada and H. Tanaka. Occurrence of brittle flaking on bearings used for automotive electrical instruments and auxiliary devices. *Wear*, 199:245–252, 1996.

[143] L. Grunberg, D. T. Jamieson, and D. Scott. Hydrogen penetration in water-accelerated fatigue of rolling surfaces. *Philosophical Magazine*, 8:1553–1568, 1963.

[144] T. Imran, B. Jacobson, and A. Shariff. Quantifying diffused hydrogen in AISI-52100 bearing steel and in silver steel under tribo-mechanical action: Pure rotating bending, sliding–rotating bending, rolling–rotating bending and uni-axial tensile loading. *Wear*, 261:86–95, 2006.

[145] M. Aoki, H. Saito, M. Mori, Y. Ishida, and M. Nagumo. Deformation microstructures of a low carbon steel characterized by tritium autoradiography and thermal desorption spectroscopy. *Journal of the Japan Institute of Metals*, 58:1141–1148, 1994.

[146] M. Śmiałowski. *Hydrogen in steel; effect of hydrogen on iron and steel during production, fabrication and use*. Pergamon Press, Oxford, U. K., 1962.

[147] G. M. Pressouyre. A classification of hydrogen traps in steel. *Metallurgical and Materials Transactions A*, 10:1571–1573, 1979.

[148] J. P. Hirth. Effects of hydrogen on the properties of iron and steel. *Metallurgical & Materials Transactions A*, 11(861–890), 1980.

[149] R. A. Oriani. Hydrogen—the versatile embrittler. *Corrosion*, 43:390–397, 1987.

[150] H. K. Brinbaum and P. Sofronis. Hydrogen-enhanced localized plasticity—a mechanism for hydrogen-related fracture. *Materials Science & Engineering A*, 176:191–202, 1994.

[151] A. R. Troiano. Role of H and other interstitials in the mechanical behaviour of metals. *Trans. ASM*, 52:54–80, 1960.

[152] B. Chalmers, R. King, and R. Shuttleworth. The thermal etching of silver. *Proceedings of the Royal Society A*, 193:465–483, 1948.

[153] K. Ryttberg, M. Knutson Wedel, V. Recina, P. Dahlman, and L. Nyborg. The effect of cold ring rolling on the evolution of microstructure and texture in 100Cr6 steel. *Materials Science & Engineering A*, 527:2431–2436, 2010.

[154] H. Brandis. Vergleichende untersuchungen an DEW–100 Cr 6 und zwei niedriglegierten wälzlagerstählen amerikanischer entwicklung. Technical Report 227/72, Deutsche Edelstalwerke Aktiengesellschaft Krefeld Forschungsinstitut, Germany, 1972.

[155] I. L. Goldblatt. Surface fatigue initiated by fatty acids. *Tribology Transactions*, 16:150–159, 1973.

[156] N. A. Branch, N. K. Arakere, V. Svensdsen, and N. H. Forster. Stress field evolution in ball bearing raceway fatigue spall. *Journal of ASTM International*, 7:ID JAI102529 1–18, 2010.

[157] A. Yonezu, T. Hara, T. Kondo, H. Hirakata, and K. Minoshima. Evaluation of threshold stress intensity factor of hydrogen embrittlement cracking by indentation testing. *Materials Science and Engineering A*, 531:147–154, 2012.

[158] B. Hildenwall. *Prediction of the residual stresses created during quenching*. PhD thesis, Linkoping University, Sweden, 1979.

[159] Delta Research Corp. *Ball/Rod RCF Tester Model BR-4 Users Manual*. Livonia, Michigan, USA, 2010.

[160] D. Glover. A ball–rod rolling contact fatigue tester. In J. J. C. Hoo, editor, *Rolling Contact Fatigue Testing of Bearing Steels ASTM STP 771*, pages 107–124, Philadelphia, USA, 1982. ASTM International.

[161] K. L. Johnson. *Contact Mechanics*. Cambridge University Press, Cambridge, U. K., 1985.

[162] J. Cook, J. E. Gordon, C. C. Evans, and D. M. Marsh. A mechanism for the control of crack propagation in all-brittle systems. *Proceedings of the Royal Society of London A*, 282:508–520, 1964.

[163] W.J. Clegg, K. Kendall, N. Alford, J.D. Birchall, and T.W. Button. A simple way to make tough ceramics. *Nature*, 347:455–457, 1990.

[164] M.-H. Evans, J. C. Walker, C. Ma, L. Wang, and R. J. K. Wood. A FIB/TEM study of butterfly crack formation and white etching area (WEA) microstructural changes under rolling contact fatigue in 100Cr6 bearing steel. *Materials Science and Engineering: A*, 570:127–134, 2013.

[165] N. K. Mukhopadhyay and P. Paufler. Micro-and nanoindentation techniques for mechanical characterisation of materials. *International materials reviews*, 51(4):209–245., 2006.

[166] M. T. Oyen and R. F. Cook. A practical guide for analysis of nanoindentation data. *Journal of the Mechanical Behavior of Biomedical Materials*, 2(4):396–407, 2009.

[167] V. García Navas, I. Ferreres, J. A. Marañón, C. Garcia-Rosales, and J. Gil Sevillano. Electro-discharge machining (EDM) versus hard turning and grinding—Comparison of residual stresses and surface integrity generated in AISI O1 tool steeltool steel. *Journal of Materials Processing Technology*, 195:186–194, 2008.

[168] G. B. Johnston, T. Andersson, E. V. Amerongen, and A. Voskamp. Experience of element and full–bearing testing of materials over several years. In J. J. C. Hoo, editor, *Rolling Contact Fatigue Testing of Bearing Steels*, pages 190–205, Philadelphia, USA, 1982. ASTM.

[169] K. Furumura, Y. Murakami, and T. Abe. Development of long life bearing steel for full film lubrication and for poor and contaminated lubrication. *Motion and Control*, 1:30–36, 1996.

[170] W. Guo, J. Yao, E. A. Jägle, P-P Choi, M. Herbig, J. M. Schneider, and D. Raabe. Deformation induced alloying in crystalline–metallic glass nano-composites. *Materials Science & Engineering A*, 628:269–280, March 2015.

[171] Eun Ju Song. *Hydrogen desorption in steels*. PhD thesis, Graduate Institute of Ferrous Technology in the Pohang University of Science and Technology, 2015.

[172] B. A. Szost. *Hydrogen trapping in bearing steels: mechanisms and alloy design*. PhD thesis, University of Cambridge, 2012.

[173] B. D. Craig. On the elastic interaction of hydrogen with precipitates in lath martensite. *Acta Metallurgica*, 25:1027–1030, 1977.

[174] K. Kawakami and T. Matsumiya. Ab-initio investigation of hydrogen trap state by cementite in BCC-Fe. *ISIJ international*, 53(4):709–713, 2013.

[175] L. C. D. Fielding. *Understanding toughness and ductility in novel steels with mixed microstructures*. PhD thesis, University of Cambridge, 2014.

[176] M. A. V. Devanathan and Z. Stachurski. The adsorption and diffusion of electrolytic hydrogen in palladium. *Proceedings of the Royal Society of London. Series A. Mathematical and Physical Sciences*, 270(1340):90–102, 1962.

[177] ISO 17081. *Method of measurement of hydrogen permeation and determination of hydrogen uptake and transport in metals by an electrochemical technique*, 2004.

[178] D. K. Han, K. Y. Kim, S. J. Kim, and H. G. Jung. Effect of heat treatment on hydrogen diffusion and hydrogen induced cracking behavior of process pipe steel in sour environment. In *The Twenty-third International Offshore and Polar Engineering Conference*. International Society of Offshore and Polar Engineers, 2013.

[179] W. Solano-Alvarez and H. K. D. H. Bhadeshia. White-etching matter in bearing steel. part II: Distinguishing cause and effect in bearing steel failure. *Metallurgical & Materials Transactions A*, 45(11):4916–4931, 2014.

[180] D. K. Han, Y. Kim, H. N. Han, H. K. D. H. Bhadeshia, and D. W. Suh. Hydrogen and aluminium in high-manganese twinning-induced plasticity steel. *Scripta Materialia*, ?:http://dx.doi.org/10.1016/j.scriptamat.2014.01.039, 2014.

[181] J. H. Ryu, Y. S. Chun, C. S. Lee, H. K. D. H. Bhadeshia, and D. W. Suh. Effect of deformation on hydrogen trapping and effusion in TRIP-assisted steel. *Acta Materialia*, 60:4085–4092, 2012.

[182] T. Tarui and M. Kubota. Approaches for fundamental principles 1: Evaluation method of hydrogen embrittlement and improvement techniques of delayed fracture. Technical Report 101, Nippon Steel, 2012.

[183] L. C. D. Fielding and H. K. D. H. Bhadeshia. Shear band structure in ballistically tested bainitic steels. *Materials Science and Technology*, 30(7):812–817, 2014.

[184] E. J. Song, D. W. Suh, and H. K. D. H. Bhadeshia. Theory for hydrogen desorption in ferritic steel. *Computational Materials Science*, 79:36–44, 2013.

[185] H. Swahn, P. C. Becker, and O. Vingsbo. Electron-microscope studies of carbide decay during contact fatigue in ball bearings. *Metal Science*, 10:35–39, 1976.

[186] O. D. Gonzalez. The measurement of hydrogen permeation in alpha iron and analysis of the experiments. *Transactions of the Metalurgical Society, American Instiute of Mining, Metalurgical and Petroleum Enginers*, 245(607-612), 1969.

[187] J. W. Christian. Thermodynamics and kinetics of martensite. In G. B. Olson and M. Cohen, editors, *International Conference on Martensitic Transformations ICOMAT '79*, pages 220–234, Massachusetts, USA, 1979. Alpine Press.

[188] K. P. Huber and G. Herzberg. Constants of diatomic molecules, molecular spectra and molecular structure vol. iv, 1979.

[189] R. Gibala, J. Ratka, J. Talia, and S. Wu. Environmental reactions and their effects on mechanical behavior of metallic materials. Technical progress report, Case Western Reserve University, 1980.

[190] D. J. Dyson and B. Holmes. Effect of alloying additions on the lattice parameter austenite. *Journal of the Iron and Steel Institute*, 208:469–474, 1970.

[191] E. Honda and Z. Nishiyama. On the nature of the tetragonal and cubic martensites. *Science Reports of Tohoku Imperial University*, 21:299–331, 1932.

[192] M. Mata, O. Casals, and J. Alcala. The plastic zone size in indentation experiments: The analogy with the expansion of a spherical cavity. *International Journal of Solids and Structures*, 43:5994–6013, 2006.

[193] H. Styri. Fatigue strength of ball bearing races and heat-treated. 52ioo steel specimens. *Proceedings of ASTM*, 51:682–700, 1951.

[194] C. Qing, S. Eryu, Z. Dongmai, G. Juwen, and F. Zonghe. Measurement of the critical size of inclusions initiating contact fatigue cracks and its application in bearing steel. *Wear*, 147:285–294, 1991.

[195] M. A. Greenfield and H. Margolin. The mechanism of void formation, void growth, and tensile fracture in an alloy consisting of two ductile phases. *Metallurgical Transactions*, 3:2649–2659, 1972.

[196] D. L. Steinbrunner, D. K. Matlock, and G. Krauss. Void formation during tensile testing of dual phase steels. *Metallurgical Transactions A*, 19:579–589, 1988.

[197] N. J. Kim and G. Thomas. Effects of morphology on the mechanical behavior of a dual phase Fe/2Si/0.1 C steel. *Metallurgical Transactions A*, 12:483–489, 1981.

[198] A. H. Nakagawa and G. Thomas. Microstructure-mechanical property relationships of dual-phase steel wire. *Metallurgical Transactions A*, 16:831–840, 1985.

[199] M. Erdogan. The effect of new ferrite content on the tensile fracture behaviour of dual phase steels. *Journal of Materials Science*, 37:3623–3630, 2002.

[200] G. Avramovic-Cingara, Y. Ososkov, M. K. Jain, and D. S. Wilkinson. Effect of martensite distribution on damage behaviour in DP600 dual phase steels. *Materials Science & Engineering A*, 516:7–16, 2009.

[201] S. J. Matas and R. F. Hehemann. The structure of bainite in hypoeutectoid steels. *TMS–AIME*, 221:179–185, 1961.

[202] Yu. N. Taran, K. I. Uzlov, and A. Yu Kutsov. Bainite reaction kinetics in austempered ductile iron. *Journal de Physique IV (Colloque)*, 7:C5–429–434, 1997.

[203] A. Kutsov, Y. Taran, K. Uzlov, A. Krimmel, and M. Evsyukov. Formation of bainite in ductile iron. *Materials Science & Engineering A*, 273–275:480–484, 1999.

[204] F. G. Caballero, M. K. Miller, and C. Garcia Mateo. Opening previously impossible avenues for phase transformation in innovative steels by atom probe tomography. *Materials Science and Technology*, 30:1034–1039, 2014.

[205] H. S. Yang and H. K. D. H. Bhadeshia. Austenite grain size and the martensite-start temperature. *Scripta Materialia*, 60:493–495, 2009.

[206] H. Liu, J. Sun, T. Jiang, S. Guo, and Y. Liu. Improved rolling contact fatigue life for an ultrahigh carbon steel with nanobainitic microstructure. *Scripta Materialia*, 90:17–20, 2014.

[207] D. O. Smith. Development of a vibrating-coil magnetometer. *The Review of Scientific Instruments*, 27(5):261–268, May 1956.

[208] B. D. Cullity and C. D. Graham. *Introduction to Magnetic Materials*. Addison–Wesley Publication Company, Reading, Mass., 1972.

[209] W. Solano-Alvarez, Eun Ju Song, Do Kyeong Han, Dong-Woo Suh, and H.K.D.H. Bhadeshia. The role of martensite plate cracks as hydrogen trapping sites in 52100 bearing steel. *Metallurgical & Materials Transactions A*, pages DOI: 10.1007/s11661–014–2680–8, 2014.

[210] C. M. Sorensen. *Magnetism in Nanoscale Materials in Chemistry*. John Wiley and Sons, Inc., New York, USA, 2002.

[211] P. L. Mangonon and G. Thomas. Structure and properties of thermal-mechanically treated 304 stainless steel. *Metallurgical transactions*, 1(6):1587–1594, 1970.

[212] S. S. M. Tavares, M. R. Da Silva, J. M. Pardal, H. F. G. Abreu, and A. M. Gomes. Microstructural changes produced by plastic deformation in the UNS S31803 duplex stainless steel. *Journal of Materials Processing Technology*, 180(1):318–322, 2006.

Appendix A

Calculation of geometrical factor K

Symbol	Description	Equation	Value
Φ_1	Ball diameter	-	12.7 mm
Φ_2	Rod diameter	-	9.53 mm
A	Cup angle	-	25.083 °
Φ_a	Ball contact diameter with balls	$\Phi_a = \Phi_1 \cos A$	11.51 mm
Φ_b	Pitch diameter of balls and retainer	$\Phi_b = \Phi_1 + \Phi_2$	22.23 mm
Φ_c	Cup contact diameter with balls	$\Phi_c = \Phi_a + \Phi_b$	33.74 mm
E	Ball revolutions for one revolution of retainer	$E = \frac{\Phi_c}{\Phi_a}$	2.932
F	Shaft revolutions for one revolution of retainer	$F = 1 + \frac{E\Phi_1}{\Phi_2}$	4.909
H	Number of stress cycles between ball and specimen for one revolution of retainer	$H = F - 1$	3.909
K	Number of stress cycles between balls and specimen for one revolution of specimen	$K = \frac{3H}{F}$	2.389

Appendix B

Phase quantification in nanobainite via magnetic measurements and X-ray diffraction

B.1 Introduction

Accurate phase quantification of nanostructured bainitic steel is of importance because of the nature of its percolating structure that controls many of its mechanical properties. X-ray diffraction is the technique of choice for such analysis, but magnetic methods can be more rapid and less sensitive to defect structures compared with the surface limitations of XRD such as stress transformation of the surface retained austenite to untempered martensite, texture, scanning step size, beam size, peak broadening due to the nanostructure, austenite/ferrite peak overlap, and errors from inadequate fitting of the Rietveld equations to determine volume fractions [21, 24]. In this study, the phase volume fractions measured using both of these techniques for the specific mixtures associated with nanostructured bainite have been compared and contrasted. An expression which relates the volume fraction and the saturation magnetisation is obtained and its form is found to be consistent with previous work done on duplex stainless steels and TRIP steels. The fitting constants used in many of such analyses vary significantly so an attempt is made to rationalise the differences by considering the factors that determine the intrinsic saturation magnetisation of ferrite.

B.2 Experimental Methods

B.2.1 Material

All alloys used were cast as 25-50 kg ingots, which were then reduced 50% in thickness via hot forging. The chemical compositions are presented in table B.1.

Table B.1 Chemical composition, wt%, of the alloys used.

Alloy	C	Si	Mn	Cr	Mo	Ni	V	Co	P	S	Al
A	0.79	1.59	1.94	1.33	0.30	0.02	0.11	-	<0.005	-	-
B	0.80	1.59	2.01	1.00	0.24	-	-	1.51	0.002	0.002	-
C	0.79	1.56	1.98	1.01	0.24	-	-	1.51	0.002	0.002	1.01
D	0.78	1.60	2.02	1.01	0.24	-	-	3.87	0.002	0.002	1.37

B.2.2 Heat treatments

The heat treatment of small samples cut via electrical-discharge machining included homogenisation at 1473 K (1200 °C) for 2 days and furnace cooling, austenitisation in the γ region 1173-1273 K (900-1000 °C) for 15 min and air cooling, bainitic transformation at different temperatures and times (table B.2) before being quenched in water at room temperature, and in some cases tempering also for different times and temperatures. For the two heat treatments prior to the bainitic transformation, samples were sealed in quartz tubes back-filled with argon or in a vacuum furnace. Cooling slowly through the 973-823 K (700-550 °C) range, following homogenisation, was used to ensure pearlite formation and avoid martensite, which could induce quench cracks [87]. Extensive characterisation by X-ray diffraction and microscopy in these and similar conditions has been reported previously [86, 88–91].

The main three parameters that determine the quantity of the ferromagnetic ferrite present are the mass, chemical composition, and the heat treatment of the samples. Therefore, the magnetisation was studied by altering only one of these three parameters at a time in order to separate out their individual contributions. For example, samples 6 and 7 have different compositions but constant heat treatment and approximately constant mass; samples 8, 9 and 10 have different mass but constant composition and heat treatment; samples 3 and 4 have different heat treatment but constant composition and approximately constant mass;

and finally samples 1 and 2 have no variation, meaning constant heat treatment, composition, and very similar mass.

Table B.2 Heat treatments performed on different samples. The weight column corresponds to the final sample geometry of thin discs used for TEM and magnetic measurements.

Sample	Alloy	Weight / g	Isothermal transformation		Tempering	
			Temperature / K (°C)	Time	Temperature / K (°C)	Time
1	A	0.01135	473 (200)	10 days	-	-
2	A	0.01065	473 (200)	10 days	-	-
3	A	0.00965	473 (200)	10 days	673 (400)	1 h
4	A	0.0089	473 (200)	10 days	773 (500)	1 h
5	B	0.00405	423 (150)	1 year	-	-
6	B	0.00395	473 (200)	4 days	-	-
7	C	0.0036	473 (200)	4 days	-	-
8	D	0.0099	473 (200)	4 days	-	-
9	D	0.0064	473 (200)	4 days	-	-
10	D	0.01235	473 (200)	4 days	-	-

B.2.3 X-ray diffraction

Samples were polished to a 1 µm finish, etched with 2% Nital and analysed with X-ray diffraction using the same parameters and equipment as described in chapter 6. Etching prior to XRD was performed in an attempt to remove the stress-transformed austenite region.

B.2.4 Transmission electron microscopy

Samples were cut into thin slices 250 µm thick using a silicon carbide cutting wheel and ground down to 40-100 µm using 1200 silicon carbide grinding paper. These thin discs of 3 mm in diameter were then electropolished using a twin jet polishing machine and a solution of 80% ethanol, 15% glycerol, and 5% perchloric acid with voltages between 20-40 V. Samples were observed in a JEOL 200 CX with an accelerating voltage of 200 kV.

B.2.5 Vibrating sample magnetometer

A vibrating sample magnetometer (VSM) allows measuring the magnetic moment of a material by applying a uniform magnetic field to a sinusoidally vibrated sample, which according to Faraday's law, changes the magnetic flux and induces a voltage in the pickup coils

that is proportional to the magnetic moment of the sample. The magnetisation can then be calculated as the resulting magnetic moment per unit volume of sample. The change of magnetic flux will be proportional to the amplitude and frequency of vibration, the magnetic moment of the sample and the distance to the pickup coils [207].

The magnetisation and coercive field of the different samples were measured at room temperature using the TEM discs prior to electropolishing and an EGG-PAR model 4500 with a maximum applied field of 600 kA m^{-1} and total measuring time of 25 min. These conditions were chosen in order to be able to compare the results to XRD volume fractions and to other magnetic measurements in the literature, which were mostly performed at room temperature. This study concentrates only on dual phase systems, but it should be noted that for the tempered samples additional measurements could be performed above the Curie temperature of cementite, 480 K (207 °C), without affecting the structure in order to obtain information about the carbide phase fractions.

B.3 Results and discussion

Given the similarity in heat treatments and expected nanostructure, only some representative samples were studied using TEM. The images obtained are presented in fig. B.1. For the sake of brevity, samples from here onwards are referred to as X-$T^{isotrans}$-$t^{isotrans}$-T^{temper}-t^{temper}-Y, where X is the alloy type, T stands for the temperature in [°C], t is the time in hours [h], days [d], or years [y], and Y is the sample number in case of there being more than one with the same composition and heat treatment.

The stereologically corrected bainitic plate size of some untempered samples was determined using the mean width in the direction normal to the plate length. For sample 1 (A-200C-10d-1) and 2 (A-200C-10d-2) the mean thickness is 39±1 nm and for sample 5 (B-150C-1y) it is 51±4 nm [86].

The volume fraction of retained austenite obtained via Rietveld analysis of the complete XRD spectra (including overlapping peaks) is presented in table B.3 along with the values of saturation magnetisation per unit mass obtained at the maximum applied field and the effective field corrected by the demagnetisation factor corresponding to shape (thickness) of each sample [208]. The magnetisation curves are presented in fig. B.2.

It can be seen from table B.3 that tempering at 773 K (500 °C) for 1 h decomposed all

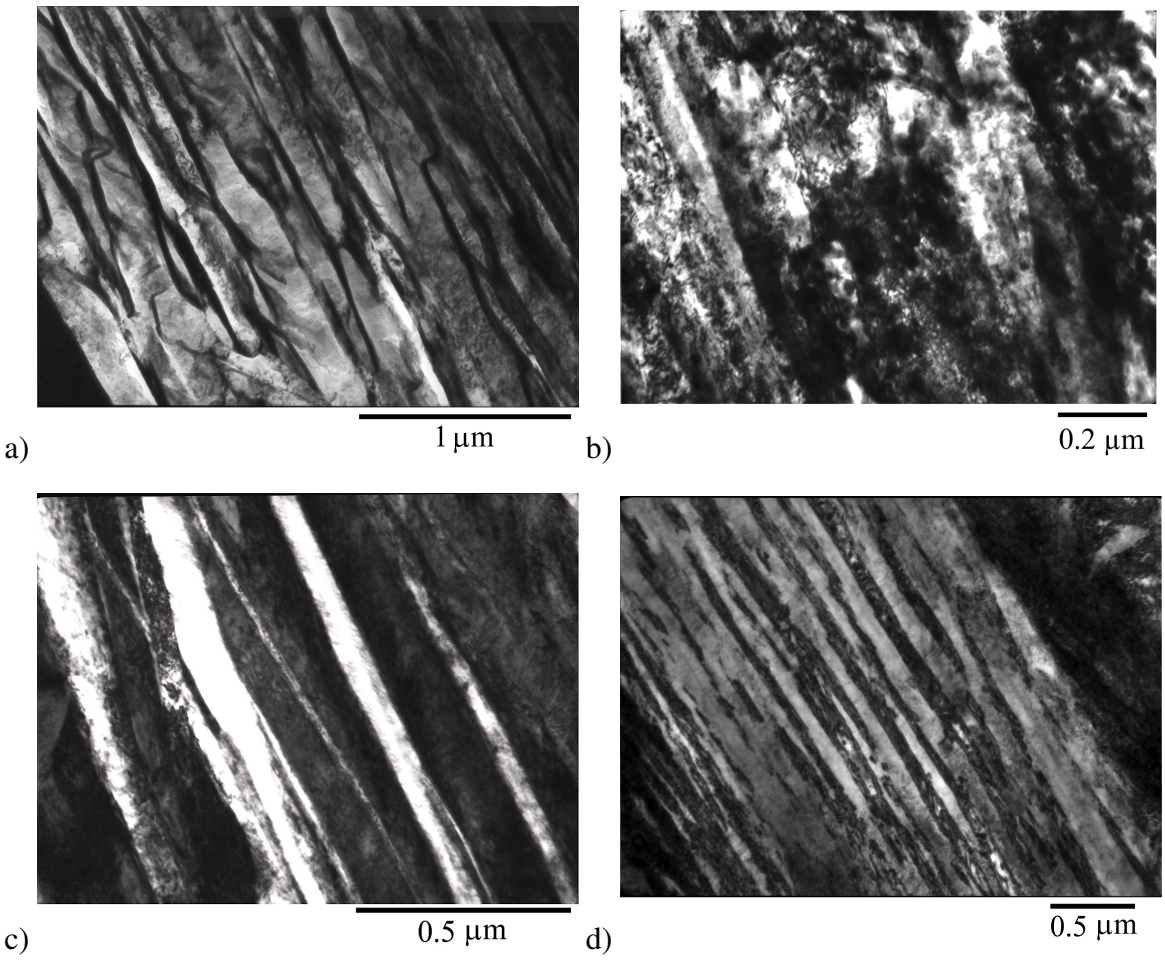

Fig. B.1 TEM micrographs of samples: a) 3 (A-200C-10d-400C-1h), b) 4 (A-200C-10d-500C-1h), c) 5 (B-150C-1y), and d) 8 (D-200C-4d-1).

Table B.3 Volume fraction of retained austenite V_γ, saturation magnetisation m_s, and effective field H_{eff} for each sample. The error to all volume fractions is ± 0.01 and for all magnetisation measurements, ± 1 . For the analysis, only bainitic ferrite and austenite were considered, although the structure will contain carbides after tempering.

Sample	V_γ	m_s / A m^2 kg^{-1}	H_{eff} / kA m^{-1}
1 A-200C-10d-1	0.215	149.4	167.6
2 A-200C-10d-2	0.215	149.2	168
3 A-200C-10d-400C-1h	0.161	152.7	168.5
4 A-200C-10d-500C-1h	0	184.9	167.6
5 B-150C-1y	0.204	154.3	172.1
6 B-200C-4d	0.192	145.5	172.3
7 C-200C-4d	0.171	163.1	172.3
8 D-200C-4d-1	0.233	147.7	168.5
9 D-200C-4d-2	0.233	150.1	170.7
10 D-200C-4d-3	0.233	143.0	167.3

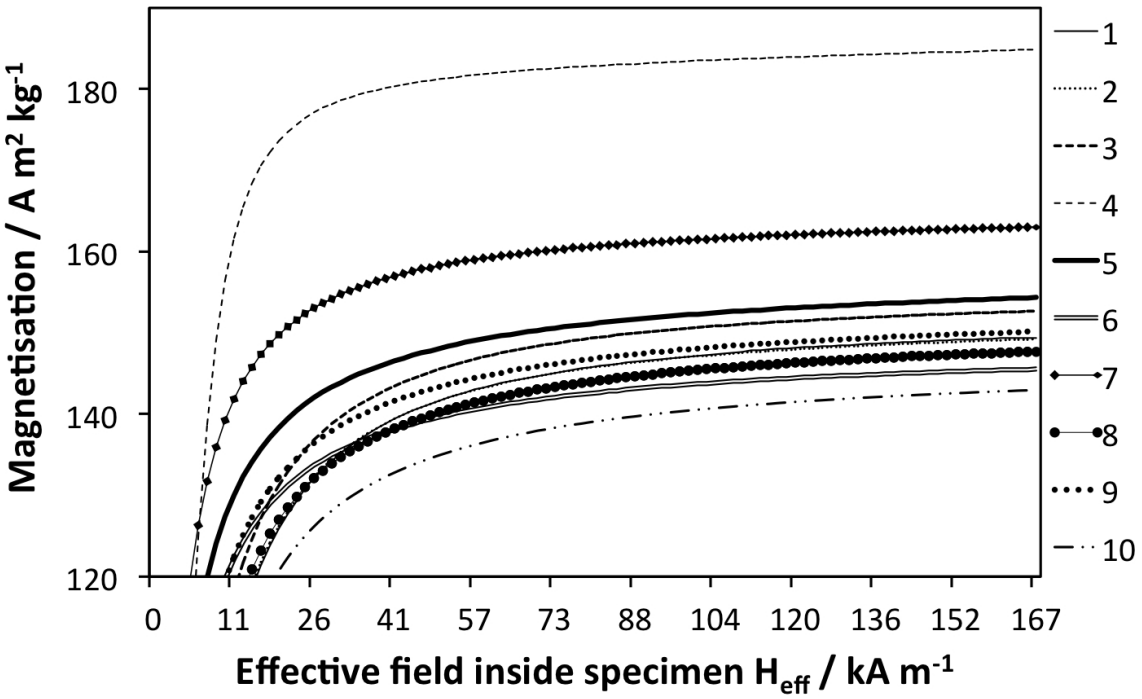

Fig. B.2 Magnetisation curves for each sample.

the retained austenite and left behind a completely ferritic structure, as confirmed by the TEM image of fig. B.1b. It is therefore not surprising that this sample displayed the highest specific saturation magnetisation. By plotting the measured volume fraction of bainitic ferrite V_{α_b} against the specific saturation magnetisation m_s (fig. B.3), it was possible to perform a linear fit which yields the following equation

$$V_{\alpha_b} = 0.0054\, m_s - 0.015 \tag{B.1}$$

The small value of the y-intercept confirms the fact that the magnetisation of a completely austenitic sample should be approximately zero [23], so the equation can be rewritten as

$$V_{\alpha_b} = \frac{m_s}{185.2} \tag{B.2}$$

The value 185.2 A m^2 kg^{-1} represents the intrinsic saturation magnetisation of ferrite (M_s) with a average of the compositions in table B.1, which is in close agreement with the measured magnetisation of 184.9 A m^2 kg^{-1} for sample 4 (A-200C-10d-500C-1h).

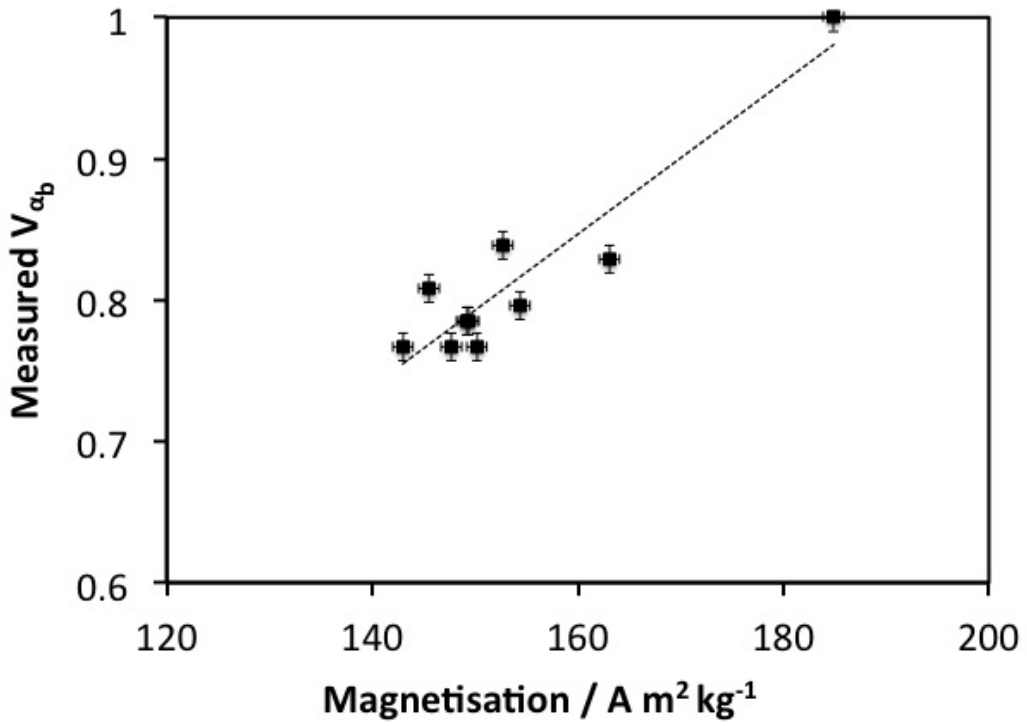

Fig. B.3 Measured volume fraction of bainitic ferrite and saturation magnetisation.

By using equation B.2, it is possible to plot the expected volume fraction of bainitic ferrite for all samples against the measured value. As seen in fig. B.4, 70% of the measured values lie within the error bars of the calculated value despite slight compositional variations. The error bars of the measured values all correspond to 0.01 given by the generally achieved accuracy of the Rietveld refinement method using HighScore Plus, whilst the error bars of the calculated values were determined by

$$\delta V_{\alpha_b} = 0.005423\,\delta m_s + 0.000137\,m_s \tag{B.3}$$

where 0.005423 is the average of the V_{α_b}/m_s ratio of all samples and 0.000137 is its standard error, as described in [23].

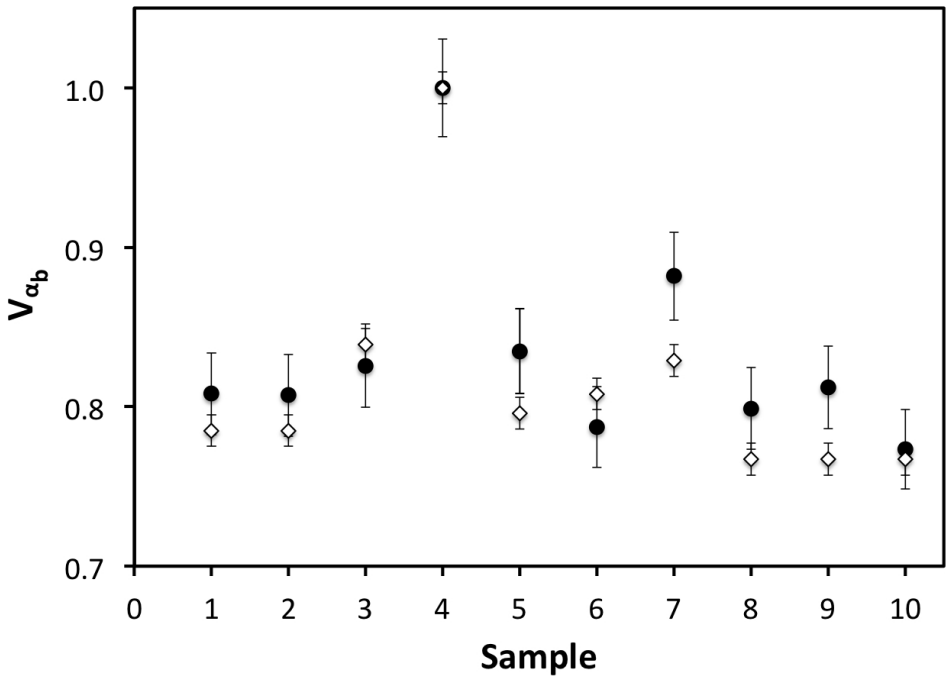

Fig. B.4 Measured volume fraction of ferrite via diffraction (black dots) compared with the calculated value (white diamond) using the proposed equation.

The fact that the ferrite volume fraction of sample 5 (B-150C-1y), 7 (C-200C-4d) and 9 (D-200C-4d-2) cannot be accurately predicted is not clear as it could not be attributed to either the mass of the sample, the chemical composition, or the heat treatment. It is possible nevertheless that since magnetic measurements were performed on TEM samples, the nanostructure was not homogenous for such sample size or there was stress induced transformation of the retained austenite to martensite. As shown in chapter 6, the austen-

ite films of nanostructured bainite in the regions of maximum subsurface shear stress do not stress transform to martensite even after significant cyclic stressing [209]. Nevertheless, less stable blocky austenite regions could in principle transform to martensite during thin disc sample preparation distorting volume fraction measurements. Ion milling of the samples would reduce this effect, but given the cost and time associated with it, standard TEM sample preparation was chosen knowing that the affected region caused by the final grinding step with 1200 grit is $\sim$26 µm for both sides, which corresponds to $\sim$10-40% of the sample volume depending on the different specimen thickness. Analysis of samples 8, 9, and 10 that have the same composition and heat treatment but different thickness (178, 155, and 222 µm respectively) confirms that the thinnest sample has the highest magnetisation and thus the highest ferrite content (150.1 A m^2 kg^{-1}) and the thickest one, the lowest (143.0 A m^2 kg^{-1}) that could in part be because the region of possible stress transformation of austenite to martensite is a larger percentage of the whole sample. Although sample preparation is a variable that could lead to further improvement of the accuracy of magnetic phase quantification, the different magnetisation values for samples 8-10 still lie within the error estimated.

A variety of values have been found for the intrinsic saturation magnetisation of ferrite in different steels (saturation magnetisation of samples containing virtually no austenite), but no quantitative explanations of such difference have been presented in the literature to date. Here, a simple calculation was performed to estimate this quantity based solely on the chemical composition of the alloy

$$M_s^{\text{calc}} = k\frac{\sum m_s^i x_i}{\sum x_i} \tag{B.4}$$

Since the only ferromagnetic elements at room temperature are iron (m_s^{Fe}=218 A m^2 kg^{-1}), cobalt (m_s^{Co}=159 A m^2 kg^{-1}), and nickel (m_s^{Ni}=54.4 A m^2 kg^{-1}), m_s for all other elements was taken as 0 A m^2 kg^{-1} [210]. x is the weight percent of each element and k is a correction factor that will be discussed later. The results of this calculation for different alloys in contrast with the measured values are presented in table B.4.

In fig. B.5, the calculated values of intrinsic saturation magnetisation for each of the alloys in table B.4 are plotted against the measured experimental values. A linear regression was applied which yielded the following equation if solved for M_s^{exp}:

$$M_s^{\text{exp}} = 1.13M_s^{\text{calc}} - 33.35 \tag{B.5}$$

Table B.4 Measured (M_s^{exp}) and calculated (M_s^{calc}) intrinsic saturation magnetisation of ferrite for different alloys, except for the ones marked with † which are martensitic. Magnetic measurements were performed at room temperature (temperature not stated in those marked with *). The chemical composition of each alloy is shown in wt%.

Name	M_s^{exp} / A m^2 kg^{-1}	M_s^{calc} / A m^2 kg^{-1}	Fe	C	Si	Mn	Cr	Mo	Ni	V	Co	P	S	N	Nb	Ti	Al
Superduplex stainless UNS S32750 [23]	128	142.1	63.523	0.02	0.34	0.83	24.57	3.75	6.68	-	-	0.026	0.001	0.26	-	-	-
Duplex stainless UNS S39205 [22]	133*	154.5	69.575	0.032	-	-	22.38	2.55	5.32	-	-	0.028	0.003	0.1123	-	-	-
304 stainless [211]	160.4* †	160.2	71.299	0.07	0.72	1.32	18.03	-	8.46	-	0.08	0.015	0.006	-	-	-	-
Superbainite (Alloy A)	184.9	204.7	93.915	0.79	1.59	1.94	1.33	0.30	0.02	0.11	-	0.005	-	-	-	-	-
300 maraging steel [25]	188	170.4	66.93	0.01	-	-	-	4.96	17.86	-	9.31	-	-	-	-	0.79	0.14
TRIP (Al1.4P) [21]	189.5	211.2	96.87	0.18	0.02	1.52	-	-	-	-	-	0.005	-	0.004	-	-	1.4
TRIP (Al1.8) [21]	197.5	210.1	96.36	0.2	0.02	1.53	-	-	-	-	-	0.081	-	0.0055	-	-	1.8
Cr- High carbon [24]	206.4 †	212.1	97.3	0.93	0.21	0.69	0.68	0.14	-	-	-	0.013	0.004	-	0.032	-	-

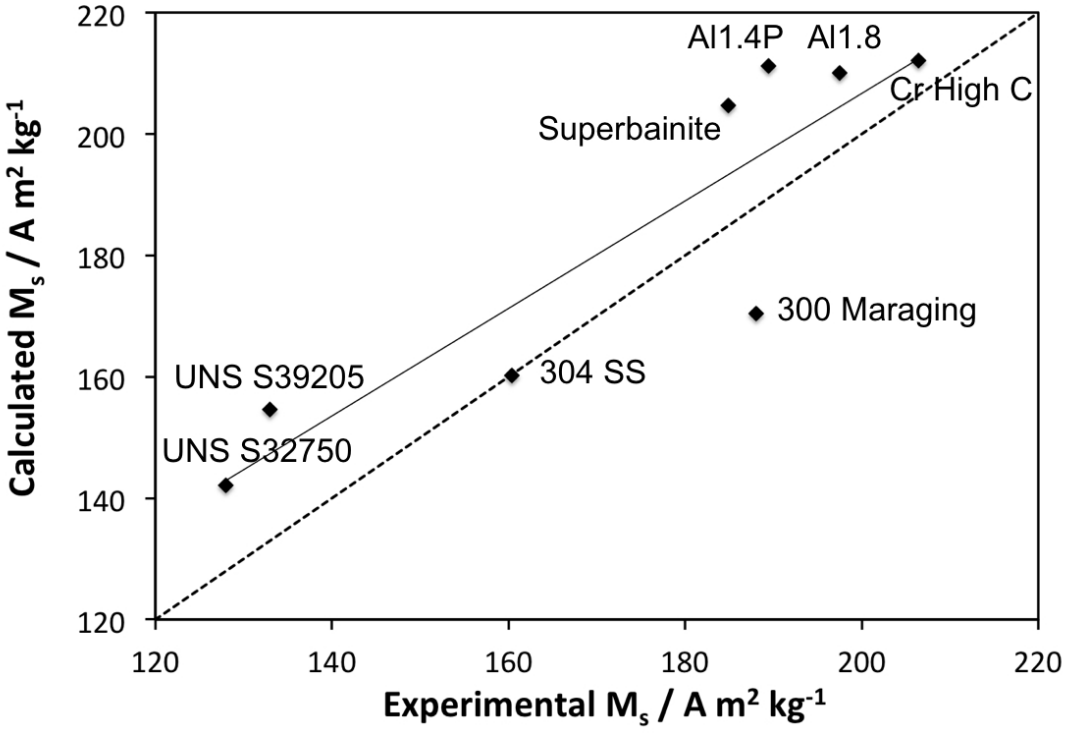

Fig. B.5 Calculated intrinsic saturation magnetisation against experimental values for different alloys. The continuous line is the applied linear regression and the dashed line represents perfect correspondence to the experimental data.

In previous work it is assumed that the chemical composition dominates the intrinsic saturation magnetisation of the ferrite, while it is acknowledged that microstructure also plays a role [21, 24, 212]. From our analysis it is possible to quantify how dominant the chemical composition actually is. Given the significant grain size difference between samples such as nanostructured bainite with a mean ferritic plate size of ∼40-60 nm and the superduplex stainless steel with grains up to ∼350 μm, it can be speculated that there must be a contribution of the ferritic grain size (domain size), shape/size of the sample[1], and crystal structure of the ferritic phase (cubic or tetragonal) that can be incorporated to equation B.4 by a constant k, which has a value of 1.052 for this study if the linear regression is performed with an intercept of zero. By providing data such as the grain and sample size in future studies, a more complete equation to predict the intrinsic saturation magnetisation of ferrite, M_s, and hence the volume fraction of ferrite/austenite could, in principle, be determined using magnetic measurements alone.

B.4 Conclusion

By performing a short magnetisation measurement at room temperature it is possible to confidently determine the amount of austenite/ferrite volume fraction of a nanostructured bainitic alloy irrespective of small compositional variations by using $V_{\alpha_b} = m_s/185.2$. Similar expressions have been derived for stainless steels with substantial compositional, grain size, and phase volume fraction differences confirming the applicability of magnetisation measurements as a reliable tool for phase quantification in steels.

A simple calculation has been performed to determine the intrinsic saturation magnetisation of ferrite based solely on the chemical composition of the ferromagnetic elements present in the alloy. The results indicate that chemical composition does not predict this property entirely and that additional parameters such as the grain size (domain size), sample size/shape, or crystal structure of the ferrite may need to be considered in the development of a generally applicable model.

[1] Zhao et al. measured a 3% difference in the saturation magnetisation between small and large samples [21].